

University of Alberta

**VELOCITY STATISTICS IN THE
ATMOSPHERIC SURFACE LAYER OVER A
DESERT**

By

DOOJDAO CHARUCHITTIPAN



A Thesis
Submitted to the Faculty of Graduate Studies and Research
in Partial Fulfillment of the Requirements
for the Degree
Master of Science

Department of Earth and Atmospheric Science

Edmonton, Alberta
Spring 2009



Library and Archives
Canada

Published Heritage
Branch

395 Wellington Street
Ottawa ON K1A 0N4
Canada

Bibliothèque et
Archives Canada

Direction du
Patrimoine de l'édition

395, rue Wellington
Ottawa ON K1A 0N4
Canada

Your file *Votre référence*
ISBN: 978-0-494-54661-1
Our file *Notre référence*
ISBN: 978-0-494-54661-1

NOTICE:

The author has granted a non-exclusive license allowing Library and Archives Canada to reproduce, publish, archive, preserve, conserve, communicate to the public by telecommunication or on the Internet, loan, distribute and sell theses worldwide, for commercial or non-commercial purposes, in microform, paper, electronic and/or any other formats.

The author retains copyright ownership and moral rights in this thesis. Neither the thesis nor substantial extracts from it may be printed or otherwise reproduced without the author's permission.

AVIS:

L'auteur a accordé une licence non exclusive permettant à la Bibliothèque et Archives Canada de reproduire, publier, archiver, sauvegarder, conserver, transmettre au public par télécommunication ou par l'Internet, prêter, distribuer et vendre des thèses partout dans le monde, à des fins commerciales ou autres, sur support microforme, papier, électronique et/ou autres formats.

L'auteur conserve la propriété du droit d'auteur et des droits moraux qui protègent cette thèse. Ni la thèse ni des extraits substantiels de celle-ci ne doivent être imprimés ou autrement reproduits sans son autorisation.

In compliance with the Canadian Privacy Act some supporting forms may have been removed from this thesis.

While these forms may be included in the document page count, their removal does not represent any loss of content from the thesis.

Conformément à la loi canadienne sur la protection de la vie privée, quelques formulaires secondaires ont été enlevés de cette thèse.

Bien que ces formulaires aient inclus dans la pagination, il n'y aura aucun contenu manquant.


Canada

Abstract

During “Dugway 2005,” an atmospheric surface layer experiment performed over a Utah desert, sonic anemometers at heights up to 26 m above ground collected 20 Hz time series of the components (u, v, w) of wind velocity, and temperature (T) . In this thesis Dugway statistics (1-hr intervals) are analyzed according to the tenets of Monin-Obukhov (MO) Similarity Theory, i.e. statistics have been normalized using as “natural scales” the friction velocity u_* , the Obukhov length L , and a related temperature scale T_* . Streamwise velocity spectra are computed, and the turbulent kinetic energy (TKE) dissipation rate (ϵ) and boundary layer depth (δ) deduced from them; ϵ is well approximated by the rate of production of TKE. Runs with extremely unstable stratification permit a cursory evaluation of McNaughton’s alternative scaling theory, whose application requires as input the dissipation rate (ϵ_0) of the “outer layer.” For those cases Dugway statistics do order with z/z_s , though not as tidily as they do under MO scaling.

Acknowledgements

I would like to express my gratitude to:

My supervisor, Dr. John D Wilson, for his advice and support throughout my study.

Everyone who participated and made the Dugway 2005 experiment possible.

The Mary Louise Imrie Graduate Student Award, which partially funded me during the 28th Conference on Agricultural and Forest Meteorology in Florida.

My family and friends for their support and encouragement.

Table of Contents

1	Introduction	1
2	Theory of the atmospheric surface layer (ASL)	4
2.1	The atmospheric boundary layer (ABL)	4
2.2	Governing equations	6
2.3	Monin-Obukhov similarity theory (MOST)	11
2.4	Turbulent kinetic energy (TKE) budget	15
2.5	Velocity spectra in the ASL	17
2.6	McNaughton's ASL scaling theory	20
3	Spectral analysis	22
3.1	Power spectral density (PSD)	23
3.2	PSD estimation by periodogram	24
3.3	Periodogram by MATLAB	25
3.4	Gaussian-Markov process as a test case	26
3.5	PSD comparison: MATLAB vs standard code	27
3.6	Aliasing	30
3.7	Improving the PSD	32
3.8	Empirical spectral formulae for atmospheric velocity spectra	34
4	Experimental background and data preparation	43
4.1	Instrumentation	43
4.2	Flow disturbance	45
4.3	Other remarks	47
4.4	Data preparation and period of calculation	47
4.5	Coordinate rotation	48
5	Analysis of intervals of unstable stratification	50
5.1	Basic MOST parameters	50
5.2	Data selection	51
5.3	Normalized standard deviation in vertical velocity ($\phi_w = \sigma_w/u_*$)	54

5.4	Normalized standard deviation in temperature ($\phi_T = \sigma_T/ T_* $)	55
6	Streamwise velocity spectra and boundary layer depth	61
6.1	Streamwise velocity spectra at Dugway	61
6.2	The boundary layer depth (δ)	64
6.3	Discussion	66
7	TKE dissipation rate during unstable stratification	73
7.1	Methods for indirect estimation of TKE dissipation rate	73
7.2	Experimental TKE dissipation rate	74
7.3	Theoretical TKE dissipation rate	75
7.4	Discussion	77
8	Dugway under stable stratification	82
8.1	Data selection	82
8.2	MOST statistics and universal functions for stable conditions	84
9	McNaughton's scaling theory for unstable stratification	90
9.1	Comparison between MOST and McNaughton's scaling theory	91
10	Conclusions	94
A	Streamwise velocity spectra for all selected unstable runs	102

List of Tables

3.1	Aliasing effects demonstrated by the Gaussian-Markov process	32
5.1	Sunrise and sunset time in Utah	52
5.2	MOST parameters for the selected unstable runs	53
6.1	Estimation of the boundary layer depth under unstable stratification	67
8.1	MOST parameters for the selected stable runs	83
9.1	MOST and McNaughton's scaling theory	91
9.2	Selected extremely unstable runs	91

List of Figures

2.1	The atmospheric boundary layer (ABL)	4
2.2	Spectral region	18
3.1	Gaussian-Markov process time series	28
3.2	One-sided PSDs estimation by MATLAB and a standard code	29
3.3	PSD estimation by MATLAB	29
3.4	Comparison between analytical and numerical PSDs	30
3.5	Hamming window	34
3.6	Improving the PSD	38
3.7	Theoretical u' spectrum of the unstable ASL	39
3.8	Variation of Kaimal's spectra with height	40
3.9	Comparison between the Kaimal's and Højstrup's spectral formulae	41
3.10	Variation of Højstrup's spectra with height	42
4.1	Location of Dugway's site	44
4.2	Dugway's instrumental set up	45
4.3	Transect wind velocities	46
5.1	Normalized standard deviation in vertical velocity	57
5.2	Time series and histograms of velocities and temperature fluctuations	58
5.3	Distributions of temperature fluctuations before and after high-pass filtering	59
5.4	Normalized standard deviation in temperature	60
6.1	An example of computed Dugway spectra	69
6.2	Variation of Dugway spectra with height, and their normalization	70
6.3	Estimation of the boundary layer depth under unstable stratification	71
6.4	Examples of Dugway spectra	72
7.1	Turbulent transport term (ϕ_t)	79
7.2	Dugway's TKE dissipation rate	80
7.3	Normalized TKE dissipation rate with different choices for ϕ_m	81

8.1	Dugway's normalized functions under stable stratification	86
8.2	Example 1 of u' spectra under stable condition.	87
8.3	Example 2 of u' spectra under stable condition.	88
8.4	Normalized TKE dissipation rate under stable condition	89
9.1	Normalized σ_w and σ_T with MOST and McNaughton scaling Theories.	93
A.1	Description for the spectral plots I	103
A.2	Description for the spectral plots II	104

List of Abbreviations and Symbols

ABL	Atmospheric boundary layer
ASL	Atmospheric surface layer
FFT	Fast fourier transform
GMT	Greenwich mean time
MOST	Monin-Obukhov similarity theory
MDT	Mountain daylight time (MDT=GMT-6 hours)
MST	Mountain standard time (MST=GMT-7 hours)
PSD	Power spectral density
TKE	Turbulent kinetic energy
Al	Aliasing
$D_2(r)$	Second-order structure functions [$\text{m}^2 \text{s}^{-2}$]
$D_3(r)$	Third-order structure functions [$\text{m}^3 \text{s}^{-3}$]
$F_u(\kappa)$	u' spectral density in wavenumber space [$\text{m}^3 \text{s}^{-2}$]
I	Imbalance
L	Obukhov length [m]
\mathbb{P}	Time period [s]
$R_{ij} \equiv \overline{u'_i u'_j}$	Reynolds stress tensor

$R_x(\tau)$	Autocovariance function of time series x
$S_u(f)$	u' spectral density in frequency space [$\text{m}^2 \text{s}^{-1}$]
$S_u(n)$	u' spectral density in normalized frequency space [$\text{m}^2 \text{s}^{-1}$]
T	Temperature [K]
T_*	Turbulent temperature scale [K]
T_ϵ	McNaughton's temperature scale [K]
c_p	Specific heat of air at constant pressure [$\approx 10^3 \text{ J kg}^{-1} \text{ K}^{-1}$]
$\bar{\epsilon} = \overline{u_i' u_i'}$	Turbulent kinetic energy [$\text{m}^2 \text{s}^{-2}$]
f	Frequency [Hz]
f_N	Nyquist frequency [Hz]
f_s	Sampling frequency [Hz]
g	Gravitational acceleration (9.81 m s^{-2})
k_v	von Karman constant (≈ 0.4)
n	Normalized frequency ($= fz/\bar{u}$)
n_δ	Normalized frequency ($= f\delta/\bar{u}$)
p	Air pressure [N m^{-2}]
t	Time [s]
(u, v, w)	Velocity components [m s^{-1}]
u_*	Friction velocity [m s^{-1}]
u_ϵ	McNaughton's velocity scale [m s^{-1}]
z	Height above ground [m]
z_0	Surface roughness length [m]
z_s	McNaughton's length scale [m]
Ω_j	Earth's angular velocity components [s^{-1}]
α_k	Kolmogorov universal dimensionless constant ($=0.5$)

δ	Boundary layer depth [m]
δ_{ij}	Kronecker Delta
ϵ	Turbulent kinetic energy (TKE) dissipation rate [$\text{m}^2 \text{s}^{-3}$]
ϵ_0	TKE dissipation rate in the outer layer [$\text{m}^2 \text{s}^{-3}$]
ϵ_{ijk}	Alternating unit tensor
θ	First rotation angle (mean wind direction) [$^\circ$]
κ	Wavenumber ($= 2 \pi f / \bar{u}$) [m^{-1}]
λ	Wavelength (\bar{u} / f) [m]
ν	kinematic viscosity [$\text{m}^2 \text{s}^{-1}$]
ν_T	Molecular thermal diffusivity
ρ	Air density [kg m^{-3}]
σ_w	Standard deviation in vertical velocity w [m s^{-1}]
σ_T	Standard deviation in temperature T [K]
σ_u^2	Variance of u [$\text{m}^2 \text{s}^{-2}$]
ϕ	Second rotation angle (mean elevation angle) [$^\circ$]
ϕ_T	Normalized standard deviation in temperature T
ϕ_h	Normalized vertical gradient of mean temperature
ϕ_m	Normalized wind shear
ϕ_t	Normalized turbulent transport
ϕ_w	Normalized standard deviation in vertical velocity w
ϕ_ϵ	Normalized turbulent kinetic energy dissipation rate
ψ	Earth's Latitude [$^\circ$]
ω	Magnitude of earth's angular velocity ($7.27 \times 10^{-5} \text{ s}^{-1}$)

Chapter 1

Introduction

The atmospheric surface layer (ASL) is broadly the lowest part of the atmosphere that is most immediately affected by contact with the earth's surface. It is of obvious importance as the environment for terrestrial life. Across the ASL vital exchanges occur between the surface and the atmosphere, e.g. momentum, sensible heat, water vapor and carbon dioxide. Dust, smoke, pollen and all manner of pollutants make their way into or out of the larger atmosphere across this layer. Since the ASL exerts a crucial control over these exchange processes, many experiments have been performed over the decades since about the 1920's, in order to deepen our understanding of the ASL. Hand in hand with the observations, a theory of the ASL has been developed that focuses on *statistics* of the observable variables (velocity, temperature, humidity, etc.). As will be seen, ASL theory is (unavoidably) a combination of rigorous information from fluid mechanics, and empiricism.

The first task facing micro-meteorologists was to comprehend the ASL in its simplest condition, i.e. over uniform, level terrain. After the provision and verification of the Monin-Obukhov similarity theory (MOST) (Obukhov 1971, Businger and Yaglom 1971, Foken 2006) it came to be considered that this stage or aspect of ASL research (i.e. the uniform case) was practically complete. MOST is the standard treatment

of the ASL in a vast array of scientific models of the environment — most obviously weather and climate models, but more broadly, almost every ecosystem model needing a causal representation of microclimate. Nevertheless continuing experiments have been interpreted by some scientists as suggesting that there is the potential to refine or replace MOST and achieve a tighter scaling of ASL statistics: and from that impetus stems this thesis, which concerns micro-meteorological statistics observed at an ideal site over a desert flat in western Utah.

The “Dugway experiment” of May 2005 probed the ASL with an array of sonic anemometers up to 26 m above ground. In this thesis, the Dugway data, consisting of 20Hz time series of wind velocities (u, v, w) and temperature (T), have been analyzed and tested in the context of Monin-Obukhov Similarity Theory. Streamwise velocity spectra, covering both unstable (i.e. daytime) and stable stratification, have been calculated following the methodology of a classical ASL experiment, viz. the Kansas experiment (Kaimal et al. 1972, Kaimal and Wyngaard 1990). From the spectra I have deduced the corresponding rate of dissipation (ϵ) of turbulent kinetic energy (TKE), and the boundary layer depth (δ). The atmospheric boundary layer (ABL) depth, which varies with time of day (as well as seasonally and geographically), defines the volume of atmosphere that (over the short term) is in contact with the ground, and so exerts a key control on atmospheric dispersion. Soon after MOST had been tested, it came to be recognized that δ should be included amongst the key scaling variable for the ASL. The TKE dissipation rate ϵ , in addition to being one of the primary variables of interest in most theories of turbulent fluid mechanics, is one of the required inputs of a new ASL scaling theory proposed by McNaughton (McNaughton 2006, McNaughton et al. 2007). The initial aim of the thesis work was to compare the performance of MOST and of the new McNaughton theory and infer which is able

most effectively to organize wind statistics of the ASL.

Chapter 2

Theory of the atmospheric surface layer (ASL)

2.1 The atmospheric boundary layer (ABL)

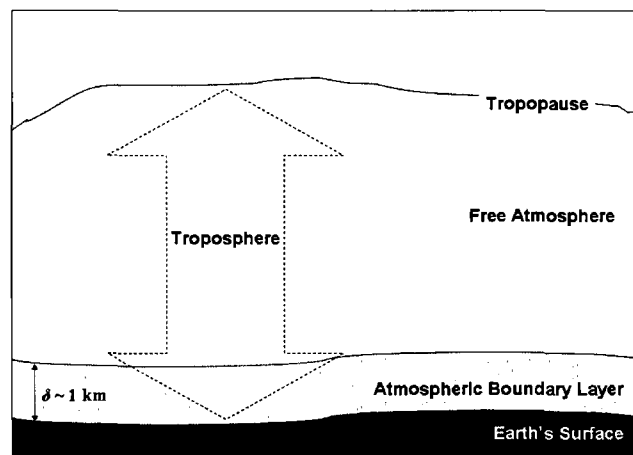


Figure 2.1: Structure of the troposphere. The lower layer is the “atmospheric boundary layer” (ABL), its height δ the boundary layer depth. The free atmosphere above extends to the rest of the troposphere (Stull 1988).

The atmospheric boundary layer (ABL) or planetary boundary layer (PBL) is the lowest part of troposphere. It is formed between the earth’s surface and the free atmosphere above (Fig. 2.1). The influence of surface forcing, e.g. surface friction, heat exchange, etc., is conveyed to the ABL by turbulent transfer on a time scale of around one hour or less (Stull 1988, Arya 1988). The depth of the ABL (δ) varies

throughout the day, in response to the diurnal cycle of heating and cooling of the earth's surface. The boundary between the ABL and the "free atmosphere" above is often quite well defined by a thin layer called the "capping inversion," where the mean temperature first starts to increase with height. The branch of meteorology that studies the ABL is normally known as micrometeorology. And micrometeorologists focus on short term statistics of the ABL, using averaging intervals that are typically from about 15 to 60 minutes.

The ABL can be separated into two nominal layers: the Atmospheric Surface Layer (ASL), and above it an outer layer that during daytime conditions may often be considered as effectively "well mixed." Then broadly speaking, the ASL is that layer within which efficiency of vertical 'mixing' is low due to the eddy size being restricted by proximity to ground, and it (the ASL) serves as a valve or conduit to the outer, well-mixed region of the ABL. According to this simplistic view the latter (i.e. outer region of the ABL) may be considered a reservoir of heat, water vapour, etc. — but a leaky reservoir, for there is some exchange with the free atmosphere across the capping inversion (entrainment fluxes). Typically, for example, the entrainment heat flux during summer daytime is regarded as having (on average) a magnitude of roughly 20% of the surface heat flux. However even though the heat budget is an important aspect of micrometeorology, in this thesis I do not focus on energetics of the ASL or ABL, but rather on statistics of *motion*. The surface heat flux will feature in my analysis because ASL velocity statistics are intricately affected by stratification, which reflects the surface heat flux.

Our concern in this thesis is the ASL, roughly the lowest 10% of the ABL with a nominal depth of order 100 m. In this layer, and assuming the underlying surface and the atmosphere above to be in a state of horizontal uniformity, the turbulent

vertical fluxes of momentum, heat, water vapour etc. and stress are approximately height-independent — indeed one may give a quantitative measure to ASL depth as that layer across which (say) the turbulent shear stress does not vary by more than (say) 10%. However such specifics are seldom of interest. What is worthwhile to state here is that the magnitudes of these surface-atmosphere exchange fluxes, regarded as roughly constant (with height, over each averaging interval) within the ASL, turn out to be the key scaling variables for the Monin-Obukhov theory of the ASL.

Flow in the ASL is strongly influenced by surface friction and stratification, but not greatly by earth's rotation, hence the Coriolis effect can be ignored (Kaimal and Finnigan 1994, Stull 1988) and wind direction considered height invariant. However above the ASL turning of the wind due to the Coriolis force (or effect) must be taken into account.

2.2 Governing equations

The theory of wind is based on a set of fundamental conservation equations, namely the continuity equation, which expresses conservation of mass, and the Navier-Stokes equations, which express Newton's second law for the case of specifically a Newtonian fluid. The coordinate system normally used in micrometeorology is the Cartesian coordinate system, with x -, y - and z -axes respectively pointing toward the east, north and vertically upward — although in the limited context of the ASL, it is more convenient to align the x -axis with the mean wind. The velocity components (u, v, w) run along the (x, y, z) axes, respectively.

The continuity and Navier-Stokes equations for a Newtonian fluid in this coordinate system can be written in the tensor notation as

Continuity equation:

$$\frac{\partial \rho}{\partial t} + \frac{\partial \rho u_j}{\partial x_j} = 0 \quad (2.1)$$

Navier-Stokes equation for Newtonian fluid:

$$\begin{array}{ccccccccc} \frac{\partial u_i}{\partial t} & + & u_j \frac{\partial u_i}{\partial x_j} & = & - & g \delta_{i3} & - & 2 \epsilon_{ijk} \Omega_j u_k & - & \frac{1}{\rho} \frac{\partial p}{\partial x_i} & + & \nu \nabla^2 u_i \\ \text{I} & & \text{II} & & & \text{III} & & \text{IV} & & \text{V} & & \text{VI} \end{array} \quad (2.2)$$

In Eq.(2.2) the Kronecker Delta is defined

$$\delta_{ij} = \begin{cases} 1 & \text{for } i = j \\ 0 & \text{for } i \neq j \end{cases} \quad (2.3)$$

and the alternating unit tensor by

$$\epsilon_{ijk} = \begin{cases} 1 & \text{for } ijk = 123, 231, 312 \\ -1 & \text{for } ijk = 321, 213, 132 \\ 0 & \text{for all other combinations.} \end{cases} \quad (2.4)$$

The components of the earth's angular velocity are

$$\Omega_j = (0, \omega \cos \psi, \omega \sin \psi) \quad (2.5)$$

and other symbols are $u_j = (u, v, w)$, the velocity components (m s^{-1}); g , the gravitational acceleration (9.81 m s^{-2}); ρ , the air density (kg m^{-3}); p , air pressure (N m^{-2}); ν , the kinematic viscosity ($\text{m}^2 \text{ s}^{-1}$); ω , earth's angular velocity ($7.27 \times 10^{-5} \text{ s}^{-1}$); and ψ , the latitude. Briefly, term I in Eq. 2.2 is a storage term, which expresses the rate of change of velocity; term II is an advection term; term III is the gravitational force; term IV is the Coriolis term, due to earth's rotation; term V is a pressure gradient force; and term VI expresses the molecular transport of momentum.

In the statistical approach to turbulence, it is normal to use the Reynolds decomposition to split each variable (say q , which could be a velocity component, a temperature, a pressure, etc.) into a mean component (\bar{q}) and the instantaneous deviation or fluctuation (q') from the mean, viz.

$$q = \bar{q} + q' \quad (2.6)$$

e.g. u' is the fluctuation of u from \bar{u} . The mean momentum equation is obtained from Eq. 2.2 by applying the Reynolds decomposition, then averaging. I shall not elaborate these steps (which are standard, and covered by many textbooks). In short, under the Boussinesq approximation (with layer mean density and temperature ρ_0, T_0) one obtains

$$\frac{\partial \bar{u}_i}{\partial t} + \bar{u}_j \frac{\partial \bar{u}_i}{\partial x_j} = -g \frac{\bar{T}}{T_0} \delta_{i3} - 2\epsilon_{ijk} \Omega_j \bar{u}_k - \frac{1}{\rho_0} \frac{\partial \bar{p}}{\partial x_i} + \nu \nabla^2 \bar{u}_i - \frac{\partial \overline{u'_i u'_j}}{\partial x_j} \quad (2.7)$$

where \bar{T} , \bar{p} are to be interpreted as the mean departure from a hydrostatic and adiabatic reference state. The first six terms in Eq. 2.7 have a form and interpretation analogous to corresponding terms in Eq. 2.2. The interesting term is the final one, which may be rewritten

$$- \frac{\partial \overline{u'_i u'_j}}{\partial x_j} = \frac{1}{\rho_0} \frac{\partial (-\rho_0 \overline{u'_i u'_j})}{\partial x_j} \quad (2.8)$$

This term is the divergence of a turbulent flux of momentum $\rho_0 \overline{u'_i u'_j}$, and indicates that the turbulent fluctuations, while not in all their detail knowable, have a direct effect on the mean motion, an effect that can not be neglected. The “kinematic” momentum flux density $R_{ij} \equiv \overline{u'_i u'_j}$ is also known as the Reynolds stress tensor, and its diagonal components are the turbulent velocity variances whose sum (the “trace” of R_{ij}) is twice the turbulent kinetic energy (TKE).

Application of Reynolds averaging to the thermodynamic energy equation yields

$$\frac{\partial \bar{T}}{\partial t} + \frac{\partial \bar{u}_j \bar{T}}{\partial x_j} = \nu_T \frac{\partial^2 \bar{T}}{\partial x_j^2} - \frac{\partial \overline{u'_j T'}}{\partial x_j} + R \quad (2.9)$$

Note that the advection term has been written as the divergence of an advective flux of heat carried by the mean wind — this is possible because (under the Boussinesq approximation) the velocity field is non-divergent. The first term in Eq. 2.9 expresses the local tendency in temperature (that is, storage of heat). The second term is the divergence of the rate of sensible heat transport by the mean wind. The third term is the (divergence of the) molecular (or conductive) flux of heat, with ν_T being the molecular thermal diffusivity. The most interesting and (in our context, important) term is the fourth, which is (minus) the divergence of the kinematic turbulent heat flux density ($\overline{u'_j T'}$), the transport of heat by the turbulence. The source term R gathers terms such as condensation/evaporation, and (any) radiative flux divergence.

This set of equations¹ for mean velocity and temperature is unclosed, in the sense that (owing to the appearance of statistics like $\overline{u'_i u'_j}$, $\overline{u'_j T'}$) they contain more unknowns than the number of equations: this does not prevent their use in an interpretive sense. In accordance with the particular flow of interest, simplifications may apply. For example generally one may neglect the molecular transport term $\nu \nabla^2 \bar{u}_i$ in Eq. 2.7, because it is very small compared to the other terms — however if one does so, there is the danger one may “forget” (or lose sight of the fact) that in reality, there is a hand over from turbulent to molecular transfer in close proximity to surfaces.

A common simplification, alluded to above, is to reorient the coordinate system. In the natural or streamline coordinate system the x -, y - and z -axes respectively

¹The set may be extended to cover whichever properties are pertinent, e.g. a mean humidity equation can be derived. Furthermore it may be extended by deriving equations for the novel terms, such as the Reynolds stress. However the Reynolds stress equation will contain still higher-order unknowns, such as $\overline{u'_i u'_j u'_k}$ so that the set is irretrievably unclosed.

point along the mean wind direction, across the mean wind, and vertically upward. In this coordinate system, by definition $\bar{v} = 0$. If the x -axis of the (alongwind, crosswind, upward) system deviates from the x -axis of the (eastward, northward, upward) system by an angle α , these two coordinate systems can be transformed to each other by rotating about the z -axis through angle α . Therefore, the earth's angular velocity components in the natural coordinate system are

$$\Omega_{j,nat} = (-\omega \cos \phi \sin \alpha, \omega \cos \phi \cos \alpha, \omega \sin \phi) . \quad (2.10)$$

In the case of the ASL, there are two further potential simplifications of enormous scope, that apply in strictly limited conditions: the assumptions of “horizontal homogeneity,” and of “stationarity.” If the site of interest is horizontally “uniform,” it *may*² be reasonable to postulate that meteorological statistics in the ASL are horizontally invariant (the assumption of horizontal homogeneity, which may be expressed as the assumption that $\partial \bar{q}/\partial x = 0$, $\partial \bar{q}/\partial y = 0$ for any mean property \bar{q} excluding the pressure). If in addition the time variation of statistics can be neglected³ (the assumption of steady state or stationarity, $\partial \bar{q}/\partial t = 0$), then ASL statistics can be taken to depend only on height (z), rather than upon all four coordinates (x, y, z, t).

To clarify the notion of the ASL as being a “constant flux layer,” one may apply the assumptions of horizontal homogeneity and stationarity to the mean heat equation (Eq. 2.9). If, furthermore, one neglects the molecular (conductive) component of the total vertical heat flux transport and assumes that there is no condensation/evaporation and no radiative divergence, then mean thermodynamic (heat)

²There obviously is a degree of subjectivity in such an assessment.

³Effectively, in assuming stationarity one assumes not that statistics are unchanging, but that the storage terms in the governing equations for mean properties are negligible relative to the dominant terms.

equation of the ASL in the streamline coordinate system reduces to

$$\frac{\partial \overline{w'T'}}{\partial z} = 0 \quad (2.11)$$

This indicates that the turbulent heat flux not only does not depend on location (x, y) but that also it does not depend on height in the ASL. Such a statement has to be carefully interpreted — for example, in the limit $z \rightarrow 0$ the conductive flux (neglected in Eq. 2.11) is not in reality negligible: to the contrary, it must carry the entire flow of heat, since the convective velocity w is negligible at microscopic distance from the ground plane.

2.3 Monin-Obukhov similarity theory (MOST)

Broadly stated, a “similarity theory” is a systematic method for finding useful empirical relations (or equations) that inter-relate dimensionless groupings of the *relevant* variables in a physical problem. These dimensionless variables are obtained by normalizing the natural variables of the system (e.g. length of a pendulum) and the available observations or properties (period of pendulum) on appropriate scale factors. Systematic methods exist to carry out such an analysis, and in particular Buckingham’s Π -theorem states the number of dimensionless ratios that must appear in the equation sought, as function of the analyst’s hypothesis as to the set of relevant variables.

Making a carefully reasoned choice of what factors control the statistics of motion and microclimate in the horizontally-uniform ASL, by application of Buckingham’s Π -theorem (Buckingham 1914) Monin and Obukhov proposed their similarity theory (MOST) in 1954. The original paper was in Russian and was not very accessible and well known outside the Soviet Union. However by the 1960’s western scientists were

well aware of the theory and publications in English were soon available (Obukhov 1971, Businger and Yaglom 1971, Foken 2006).

MOST purports to describe the height variation of ASL statistics, in a layer of the horizontally-homogeneous ASL spanning the height range $z_0 \ll z \ll \delta$, where z_0 is the surface roughness length (MOST is said to apply “above the roughness sublayer”) and δ is the ABL depth (say nominally $\delta \approx 1000$ m). MOST posits that the statistical state of the horizontally-uniform ASL is controlled by a small number of key parameters, from which can be derived appropriate scales (in particular, the Obukhov length L) to normalize measured statistics. The details of these key scaling parameters are summarized below (subscript 0 indicates the value at the surface):

Key parameters

- Buoyancy parameter [$\text{m s}^{-2} \text{K}^{-1}$]: g/T_0
- Kinematic surface stress [$\text{m}^2 \text{s}^{-2}$]:

$$\frac{\tau_0}{\rho} = [(\overline{u'w'})_0^2 + (\overline{v'w'})_0^2]^{1/2} \quad (2.12)$$

- Kinematic surface heat flux [$\text{m s}^{-1} \text{K}$]:

$$\frac{H_0}{\rho c_p} = (\overline{w'T'})_0 \quad (2.13)$$

- Height above surface [m]: z

MOST scaling parameters

From the assumption that ASL state is controlled by the above properties, Monin and Obukhov deduced that ASL statistics might be normalized using the following scales:

- Friction velocity [m s⁻¹]:

$$u_* = [(\overline{u'w'})_0^2 + (\overline{v'w'})_0^2]^{1/4} \quad (2.14)$$

- Obukhov length [m]:

$$L = -\frac{u_*^3}{k_v \frac{g}{T_0} (\overline{w'T'})_0} \quad (2.15)$$

- Turbulent temperature scale [K]:

$$T_* = -\frac{(\overline{w'T'})_0}{u_*} \quad (2.16)$$

In the above definitions surface values are taken as being representative for the whole (shallow) layer. The dimensionless von Karman constant ($k_v \approx 0.4$) is included in the definition of the Obukhov length by convention (rather than necessity); c_p is the specific heat of air at constant pressure ($\approx 1000 \text{ J kg}^{-1} \text{ K}^{-1}$).

A successful scaling theory of the ASL must describe the influence of atmospheric stratification, or “atmospheric stability.” In MOST, atmospheric stability is parameterized by the ratio

$$\frac{z}{L} = -\frac{(g/T_0)(\overline{w'T'})_0}{u_*^3/k_v z} \quad (2.17)$$

such that the stability classification is:

$$\frac{z}{L} \begin{cases} > 0 & \text{Stable} \\ = 0 & \text{Neutral} \\ < 0 & \text{Unstable} \end{cases} \quad (2.18)$$

Finally, the “content” of MOST is the prediction that suitably normalized statistics are universal functions of z/L . Some of the important non-dimensional functions

central to MOST are

$$\phi_m = \frac{k_v z}{u_*} \frac{\partial \bar{u}}{\partial z} \quad \text{normalized wind shear} \quad (2.19)$$

$$\phi_h = \frac{k_v z}{T_*} \frac{\partial \bar{T}}{\partial z} \quad \text{normalized vertical gradient of mean temperature}^4 \quad (2.20)$$

$$\phi_w = \frac{\sigma_w}{u_*} \quad \text{normalized standard deviation in } w \quad (2.21)$$

$$\phi_T = \frac{\sigma_T}{|T_*|} \quad \text{normalized standard deviation in } T \quad (2.22)$$

$$\phi_\epsilon = \frac{k_v z \epsilon}{u_*^3} \quad \text{normalized TKE dissipation rate} \quad (2.23)$$

(where σ_w , σ_T are the standard deviations of w and T). Numerous experimenters have proposed functional forms for the universal functions based on field experiments, and some examples that are of interest in the balance of my thesis are:

Dyer and Bradley (1982):

$$\phi_m = (1 - 28 z/L)^{1/4}, \quad -4 \leq z/L \leq -0.004 \quad (2.24)$$

Businger et al. (1971), Högström (1988):

$$\phi_m = \begin{cases} (1 - 19.3 z/L)^{-1/4}, & -2 \leq z/L \leq 0 \\ 1 + 6 z/L, & 0 \leq z/L \leq 1 \end{cases} \quad (2.25)$$

Wyngaard and Coté (1971):

$$\phi_\epsilon = \begin{cases} [1 + 0.5 |z/L|^{2/3}]^{3/2}, & -2 \leq z/L \leq 0 \\ [1 + 2.5 (z/L)^{3/5}]^{3/2}, & 0 \leq z/L \leq 1 \end{cases} \quad (2.26)$$

Kaimal (1978):

$$\phi_\epsilon = [1 + 0.75 |z/L|^{2/3}]^{3/2}, \quad z/L < 0 \quad (2.27)$$

⁴Strictly, Eq. 2.20 gives the gradient in mean *potential* temperature.

Panofsky et al. (1977):

$$\phi_w = 1.3 (1 - 3z/L)^{1/3}, \quad z/L < 0 \quad (2.28)$$

Wilson (2008):

$$\phi_w = 1.0 (1 - 4.5z/L)^{1/3}, \quad z/L < 0 \quad (2.29)$$

Kaimal and Finnigan (1994):

$$\phi_T = \begin{cases} 2 (1 + 9.5 |z/L|)^{-1/3}, & -2 \leq z/L \leq 0 \\ 2 (1 + 0.5 z/L)^{-1}, & 0 \leq z/L \leq 1 \end{cases} \quad (2.30)$$

Tillman (1972):

$$\phi_T = -0.95 (0.05 - z/L)^{-1/3}, \quad -60 < z/L \leq 0.5 \quad (2.31)$$

MOST is expected to be valid provided the wind is not too weak (u_* not too small) (Stull 1988), and poor organization typically occurs when attempting to scale observations stemming from periods when the friction velocity is less than or of order of 10 cm s^{-1} , a level that is typically encountered nocturnally.

2.4 Turbulent kinetic energy (TKE) budget

Let e be the instantaneous fluctuation kinetic energy,

$$e = \frac{1}{2} u_i' u_i' = \frac{1}{2} (u'^2 + v'^2 + w'^2). \quad (2.32)$$

The turbulent kinetic energy is the statistic

$$\bar{e} = \frac{1}{2} \overline{u_i' u_i'} = \frac{1}{2} (\overline{u'^2} + \overline{v'^2} + \overline{w'^2}) \quad (2.33)$$

and is a key turbulence diagnostic, whose behavior is best understood by reference to the ‘‘TKE budget equation’’ obtained as follows. By manipulating the instantaneous

and the mean momentum equations, one can construct an equation for the velocity fluctuation

$$\frac{\partial u'_i}{\partial t} + \bar{u}_j \frac{\partial u'_i}{\partial x_j} + u'_j \frac{\partial \bar{u}_i}{\partial x_j} + u'_j \frac{\partial u'_i}{\partial x_j} = g \frac{T'}{T_0} \delta_{i3} - 2\epsilon_{ijk} \Omega_j u'_k - \frac{1}{\rho_0} \frac{\partial p'}{\partial x_i} + \nu \nabla^2 u'_i + \frac{\partial \overline{u'_i u'_j}}{\partial x_j} \quad (2.34)$$

Multiplying Eq. 2.34 by u'_i and averaging, one obtains (after straightforward algebraic manipulation) the TKE budget equation (Wyngaard and Coté 1971):

$$\begin{array}{cccccccc} \frac{\partial \bar{e}}{\partial t} & + & \bar{u}_j \frac{\partial \bar{e}}{\partial x_j} & = & \frac{g}{T_0} \overline{w'T'} & - & \overline{u'_i u'_j} \frac{\partial \bar{u}_i}{\partial x_j} & - & \frac{\partial \overline{u'_j e}}{\partial x_j} & - & \frac{1}{\rho_0} \frac{\partial \overline{u'_i p'}}{\partial x_j} & - & \epsilon \\ \text{I} & & \text{II} & & \text{III} & & \text{IV} & & \text{V} & & \text{VI} & & \text{VII} \end{array} \quad (2.35)$$

Term I expresses storage of TKE, and Term II the advection or transport of TKE by the mean wind. Term III is the buoyant production term, the gain (in unstable stratification) or loss (stable stratification) of TKE due to the rate of working by buoyancy force. Term IV is the shear production term. Term V represents transport of TKE by the turbulence, and Term VI is pressure transport. Term VII is the viscous dissipation term, i.e. the mean rate of conversion of kinetic into internal energy.

Let us assume we may apply the assumptions of horizontal homogeneity and stationarity to Eq. 2.35. Then the TKE budget equation for the ASL in the natural coordinate ($\bar{v} = 0$) system is

$$0 = \frac{g}{T_0} \overline{w'T'} - \overline{u'w'} \frac{\partial \bar{u}}{\partial z} - \frac{\partial \overline{w'e}}{\partial z} - \frac{1}{\rho_0} \frac{\partial \overline{w'p'}}{\partial z} - \epsilon \quad (2.36)$$

It is often considered that the buoyant production, shear production and viscous dissipation terms dominate, and (in sum) approximately balance each other – such a balance is termed “local equilibrium.” However the validity of assuming local equilibrium ought to be assessed in each experimental situation.

2.5 Velocity spectra in the ASL

The turbulent velocity spectrum conveys the (‘spectral’) distribution of kinetic energy across the scale-range of eddy sizes contributing to a turbulent flow. For example if we consider specifically the spectrum $F_u(\kappa)$ of the streamwise velocity fluctuation as function of eddy wavenumber κ then

$$\sigma_u^2 \equiv \overline{u'^2} = \int_0^{\infty} F_u(\kappa) d\kappa \quad (2.37)$$

A spectrum (or “power spectral density”) is calculated from the time series (in this case, of the velocity fluctuation) either in wave number (κ) or frequency (f) space (more detail follows in Chapter 3). As indicated by Eq. 2.37 the area under the spectral density curve measures the variance of the turbulence, and the shape of the spectrum indicates the relative importance of “fast” and “slow” eddies.

It is useful (and conventional) to think of the turbulence spectrum as separating into three spectral regions (Fig. 2.2).

1. The *energy-containing range* is the spectral region where the energy is created and input to the flow by buoyancy and shear. It usually accounts for a large proportion of the total variance.
2. The *inertial subrange* is defined as that band of wavenumbers across which there is neither TKE production (by shear or buoyancy) nor conversion to heat (by viscosity). However, there exists an “energy cascade” whereby the kinetic energy of larger eddies is transferred to kinetic energy of smaller eddies, without net loss: the physical mechanism for this transfer is vortex stretching.
3. The *dissipation range* encompasses all scales of motion that are directly damped by viscosity, and its upper (frequency) limit defines the smallest/fastest motions

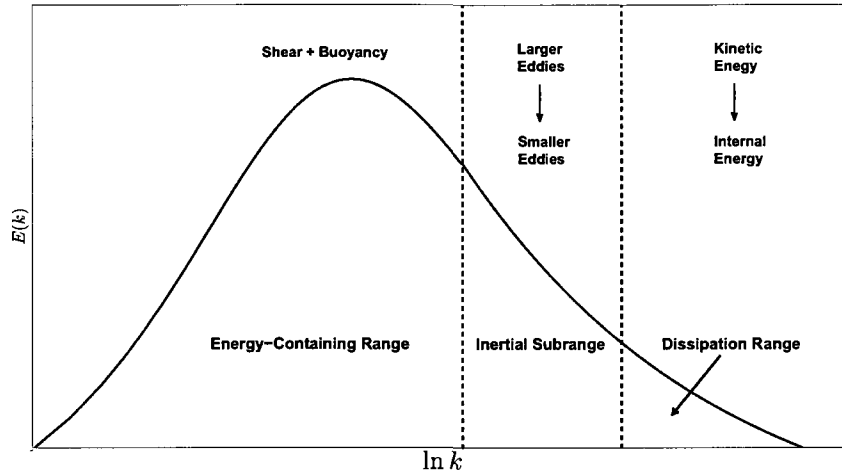


Figure 2.2: The turbulent velocity spectrum can be considered to subdivide into three spectral regions. The “energy-containing range” of scales of motion includes the scales at which turbulent kinetic energy is supplied by shear and buoyant production, and usually accounts for a large proportion of the total variance. At the other end of the spectrum, the “dissipation range” of scales of motion contains those small scale eddies whose motion is affected by viscosity, and its upper (frequency) limit defines the smallest/fastest motions that can survive under the action of viscosity. Between these two spectral regions lies the inertial subrange of scales. In this spectral region neither shear nor buoyant production provide energy directly, and nor does viscosity dampen these eddies. Rather, in a statistical sense energy is passed from the larger to the smaller scales, without net loss (the spectral transfer rate is ϵ), the physical mechanism being vortex stretching.

that can survive under the action of viscosity. It is the spectral region where the kinetic energy is converted to internal energy (i.e. heat).

An analysis by Kolmogorov (Kaimal and Finnigan 1994, Stull 1988) predicts that in the inertial subrange, the u' spectrum in wave number space ($F_u(\kappa)$) obeys the similarity law

$$F_u(\kappa) = \alpha_k \epsilon^{2/3} \kappa^{-5/3}, \quad (2.38)$$

where α_k is Kolmogorov’s universal dimensionless constant whose numerical value is assumed to be 0.5 in my analysis (Sreenivasan 1995). Taking the logarithm of Eq. 2.38 we have

$$\log[\kappa F_u(\kappa)] = \log(\alpha_k \epsilon^{2/3}) - \frac{2}{3} \log \kappa \quad (2.39)$$

and this is the basis for a convenient means to deduce the TKE dissipation rate ϵ . If one plots $\kappa F_u(\kappa)$ vs κ on log-log axes, Eq. 2.39 is in the form of straight line equation with slope $-2/3$ and y -axis intercept at $\log(\alpha_k \epsilon^{2/3})$. Therefore, at $\log \kappa = 0$ or $\kappa = 1$,

$$\log F_u(\kappa) |_{\kappa=1} = \log(\alpha_k \epsilon^{2/3}) \quad (2.40)$$

$$\epsilon = [\alpha_k^{-1} F_u(\kappa)]^{3/2} |_{\kappa=1} \quad (2.41)$$

A small revision is needed. In the Dugway experiment, the data were collected in frequency space, hence, it is more convenient to work in the frequency space rather than the wave number space. Following convention the underlying wave number is related to the (manifested) frequency by way of Taylor's "frozen turbulence" hypothesis, such that

$$\kappa = \frac{2\pi f}{\bar{u}}. \quad (2.42)$$

Accordingly the u' spectra in wave number space $F_u(\kappa)$ and in frequency space $S_u(f)$ can be related to each other: the variance σ_u^2 is the area under the spectral curve, and must be preserved irrespective of whether f or κ is taken as spectral coordinate. Therefore,

$$\int_0^\infty F_u(\kappa) d\kappa = \sigma_u^2 = \int_0^\infty S_u(f) df \quad (2.43)$$

More basically, it is evident that by virtue of the meaning of the spectral density it must be true that

$$\kappa F_u(\kappa) = f S_u(f) \quad (2.44)$$

Many studies of ASL spectra use the normalized frequency n , defined by

$$n = \frac{fz}{\bar{u}} \quad (2.45)$$

The relation in Eq. 2.44 still holds in this space, i.e.

$$\kappa F_u(\kappa) = f S_u(f) = n S_u(n) \quad (2.46)$$

2.6 McNaughton’s ASL scaling theory

MOST neglects any influence of the outer ABL on surface layer statistics, other than that expressed through the imposed mean momentum and heat fluxes. According to McNaughton (2006), this is unrealistic: “MOST is flawed because it fails to account for the variations in the forcing of the whole surface layer imposed by the large eddies of the outer layer.” McNaughton proposes that ASL turbulence is “self-organizing system, which is insensitive to the stability and the surface layer is driven from above.” In this model, instead of using the Reynolds two part decomposition, properties are decomposed into three parts: the long-time mean component \bar{q} , a slow fluctuation caused by the outer-scale forcing (from the layer above) \tilde{q} , and a rapid “inner-layer” fluctuation q'' (McNaughton 2006, Nakamura and Mahrt 2006). Thus the three part decomposition is

$$q = \bar{q} + \tilde{q} + q'' \quad (2.47)$$

(Note: the sum of the slow and rapid fluctuations is equivalent to the total fluctuation q' in the Reynolds decomposition). McNaughton assumes that:

- Mean and outer-scale components of vertical velocity are zero,
- Outer-scale motions do not carry momentum in the ASL,
- Cross-scale covariance terms vanish.

The new scheme leads to an alternative set of scaling parameters (McNaughton 2006, McNaughton et al. 2007) in lieu of MOST-scaling, viz.

Length scale [m]

$$z_s = \frac{w_*^3}{k_v \epsilon_0}, \quad (2.48)$$

Velocity scale [m s⁻¹]

$$u_\epsilon = (k_v z \epsilon)^{1/3}, \quad (2.49)$$

and temperature scale [K]

$$T_\epsilon = -\frac{(\overline{w'T'})_0}{u_\epsilon} \quad (2.50)$$

where ϵ_0 is the TKE dissipation rate in the outer layer above the ASL. Unlike MOST's velocity scale u_* , McNaughton's velocity scale explicitly varies with height (unless it should happen that $\epsilon \propto z$, which is a circumstance commonly *assumed* for the neutral ASL or wall shear layer).

McNaughton's is a new scaling theory, and the Dugway experiment was largely oriented towards testing it.

Chapter 3

Spectral analysis

Spectral analysis decomposes a stochastic signal into its frequency or wave number components (Stull 1988) to provide a diagnostic that complements the more elementary statistical properties, e.g probability density functions or their moments, the means, variances etc. In the turbulent ABL, spectral analysis reveals the range of eddy sizes contributing to the motion. As a digression intended only to convey the usefulness of the velocity spectrum as a descriptor, consider the information that would be needed as a precursor to designing an anemometer capable of responding to all turbulent fluctuations. The power spectrum of velocity defines (in a rather complete technical sense) what is meant by “all turbulent fluctuations,” and if the power spectrum of the wind is known, it reveals the necessary speed of response and spatial resolution of an anemometer for satisfactory operation under those conditions. There is (or was) evidently an interesting chicken-and-egg problem in the development of suitable turbulence sensors for the ASL: one could not design an anemometer adequate to capture the entire spectrum of wind velocity without knowing the spectrum, and what level of performance (by implication) would be needed.

Although velocity spectra are of interest in their own right, in this thesis they have been computed as a means to an end, namely because it is possible to estimate

from them other interesting global (ABL depth, δ) or local (TKE dissipation rate, ϵ) properties of the ABL. The possibility to do so hinges on the fact that earlier experiments have permitted the development of empirical formulae for the velocity spectra, formulae that involve these parameters: thus by fitting those pre-existing empirical formulae to measured spectra, one may extract δ, ϵ and so on. Of course before doing so, one would wish to feel justified in believing that the Dugway spectra do not differ qualitatively from the spectra of the earlier, classic experiments (such as the Kansas and Minnesota experiments). To the extent that the ASL really does have a universal statistical structure (for given overall state δ, L etc.), it should be surprising if Dugway spectra differed in a systematic way from classic spectra, or from the spectral formulae derived from them.

Spectra reported in this thesis were computed using MATLAB's periodogram code. However, as a precursor and to be confident regarding its performance, I first tested the MATLAB code relative to the known spectrum of an idealized stochastic process, namely a "Markov chain."

3.1 Power spectral density (PSD)

Let $x = x(t)$ be a stochastic signal. Its two-sided Power Spectral Density $S_x(f)$ is the Fourier transform of the autocovariance function $R_x(\tau)$ (Stoica and Moses 1997, Broersen 2006, Priestley 1981)

$$S_x(f) = \int_{-\infty}^{\infty} R_x(\tau) e^{-2i\pi f\tau} d\tau \quad (3.1)$$

where the autocovariance function is

$$R_x = E[(x_{t_0} - \mu)(x_{t_0+\tau} - \mu)] \quad (3.2)$$

(f is frequency (Hz), and $\mu \equiv E[x]$ is the mean or expectation value of x). If $[x]$ represents the “units of x ” then the spectral density $S_x(f)$ has the units of $[x]^2$ per unit frequency. The power spectral density and the autocovariance function constitute a Fourier transform pair, and from the inverse transform (the companion to Eq. 3.1) it follows that at $\tau = 0$

$$R_x(0) = \sigma_x^2 = \int_{-\infty}^{\infty} S_x(f) df , \quad (3.3)$$

where σ_x^2 is a variance of the signal x — by definition, the total “power” of the signal.

3.2 PSD estimation by periodogram

There are many variations in the technique used to estimate the PSD of a signal. One of the most popular and basic methods is founded on the “periodogram” of the signal . The periodogram method is non-parametric (makes no assumption about the underlying probability distribution of the signal) and estimates the PSD directly from the signal (as opposed to requiring calculation of the autocovariance function). The heavy computational burden of the periodogram approach, which once limited its popularity, was overcome by the development of the “fast fourier transform” (FFT). FFT demands that the number of samples in the time series be some integer power of 2, therefore if this is not the case there series is normally padded with zeros or truncated.

Consider the time series $[x_{-n}, x_{-n+1}, \dots, x_{n-1}]$, having $N = 2n$ samples separated by intervals Δt . The time duration of the series is

$$\mathbb{P} = (N - 1) \Delta t = (2n - 1) \Delta t , \quad (3.4)$$

and defines a fundamental frequency

$$\Delta f = 1/\mathbb{P} \quad (3.5)$$

The two-sided periodogram of this time series is by definition

$$S_x(f_k) = \frac{\mathbb{P}}{N^2} \left| \sum_{r=-n}^{n-1} (x_r - \bar{x}) e^{-j2\pi kr/N} \right|^2, \quad -n \leq k \leq n-1 \quad (3.6)$$

where

$$f_k \equiv \frac{k}{\mathbb{P}} = k\Delta f \quad (3.7)$$

For real signals the periodogram is symmetric in k , so the two-sided PSD is identical to one half of the one-sided PSD (positive k).

Sampling on intervals Δt , that is at sampling frequency $f_s = 1/\Delta t$, implies a maximum resolvable frequency, called the ‘Nyquist frequency,’

$$f_N = \frac{f_s}{2}. \quad (3.8)$$

If the signal x contains power at frequencies exceeding f_N , in its computed spectrum that spectral power will be “folded” to appear (spuriously) as power at lower frequency, an effect known as ‘aliasing.’

3.3 Periodogram by MATLAB

In MATLAB a one-sided PSD by periodogram is calculated (using the FFT method) by invoking the command:

```
[pxx,f]=periodogram(x>window,nfft,fs)
```

with

pxx = PSD of timeseries x	f = frequency (Hz)
x = timeseries (non-zero mean allowed)	windows = data window
nfft = length of FFT	fs = sampling freq

By default, for real signals this command will return the one-sided PSD, which contains the total power (or variance) of the input signal.

3.4 Gaussian-Markov process as a test case

To test the MATLAB procedure I have computed the PSD of an artificial time series generated using a “Markov chain,”

$$x_{i+1} = \alpha x_i + \beta \sigma_x \delta_{i+1}, \quad (3.9)$$

where $0 \leq \alpha \leq 1$ is a memory coefficient, and the δ_k are independent samples from a standardized Gaussian distribution (i.e. $E[\delta] = 0$, $E[\delta^2] = 1$). If this series is initialized by a Gaussian random sample (mean zero, standard deviation σ_x), and provided (also) that the coefficient β is specified as $\beta = \sqrt{1 - \alpha^2}$, this algorithm will produce a series having zero mean and variance σ_x^2 . Furthermore its autocorrelation coefficient is also known — for example if the sampling interval is Δt then $R_x(\Delta t) \equiv \alpha$, while $R_x(2\Delta t) \equiv \alpha^2$. Eq. 3.9 defines a ‘Gaussian-Markov process,’ i.e. a stochastic process $\{x_t : t \geq 0\}$ that is both Gaussian (normally distributed, with mean zero and variance σ_x^2) and ‘Markovian’ in the sense that a ‘future’ value x_{i+1} depends on the ‘present’ (x_i), but not on the past (Finch 2004).

Regarding the specification of α , I chose

$$\alpha = \exp\left(-\frac{\Delta t}{\Gamma}\right) \quad (3.10)$$

where Γ is the desired autocorrelation timescale ($\Delta t \ll \Gamma$). The initial condition can be written

$$x_1 = \delta_1 \quad (3.11)$$

With these specifications, the Markov chain generates a series having the following

properties:

$$\begin{aligned}
 \text{mean} & & E[x_i] &= 0 \\
 \text{variance} & & E[x_i^2] &= \sigma_x^2 \\
 \text{covariance} & & \text{cov}(x_i, x_{i+1}) &= E[(x - \bar{x}_i)(x_{i+1} - \bar{x}_{i+1})] = \sigma_x^2 \exp[-\Delta t/\Gamma]
 \end{aligned}$$

From Eq. 3.9, the two-sided PSD can be computed analytically by using Eq. 3.1 as

$$S_x(f) = \int_{-\infty}^{\infty} \sigma_x^2 e^{-t/\Gamma} e^{-2i\pi ft} dt \quad (3.12)$$

Reference to a Table of Integrals (or a Fourier Transform Table) shows that

$$\int_{-\infty}^{\infty} e^{-bx} e^{-iax} dx = \frac{2b}{a^2 + b^2} \quad (3.13)$$

If we define

$$f_0 \equiv (2\pi\Gamma)^{-1} \quad (3.14)$$

then the PSD of the Markov chain is

$$S_x(f) = \frac{2\sigma_x^2 \Gamma}{1 + (f/f_0)^2} \quad (3.15)$$

In micrometeorology it is usual to use the one-sided PSD, whose integral over positive frequencies yields the total variance. Obviously (from Eq. 3.15) $S_x(f)$ is symmetric in f , thus the one-sided PSD, $S_x^{(1)}(f)$, is twice the two-sided PSD:

$$S_x^{(1)}(f) = \frac{4\sigma_x^2 \Gamma}{1 + (f/f_0)^2} \quad (3.16)$$

3.5 PSD comparison: MATLAB vs standard code

To test the MATLAB routine for spectral analysis, I generated a set of sixteen independent Markov chains, each having the identical specification:

Number of samples: $N = 1024$	Time interval: $\Delta t = 0.05$ s
Variance: $\sigma_x^2 = 1$	Sampling frequency: $f_s = 20$ Hz
$\Gamma = 1$ s	Period: $\mathbb{P} = 51.15$ s
$\alpha = 0.9048$	$\beta = \sqrt{1 - \alpha^2} = 0.4258$

Fig. 3.1 gives one of the sixteen artificial signals. Of course since the δ 's are independent, the sixteen sequences were not identical. For each sequence I computed the PSD by the periodogram method, then averaged those sixteen spectra to provide my spectral estimation.

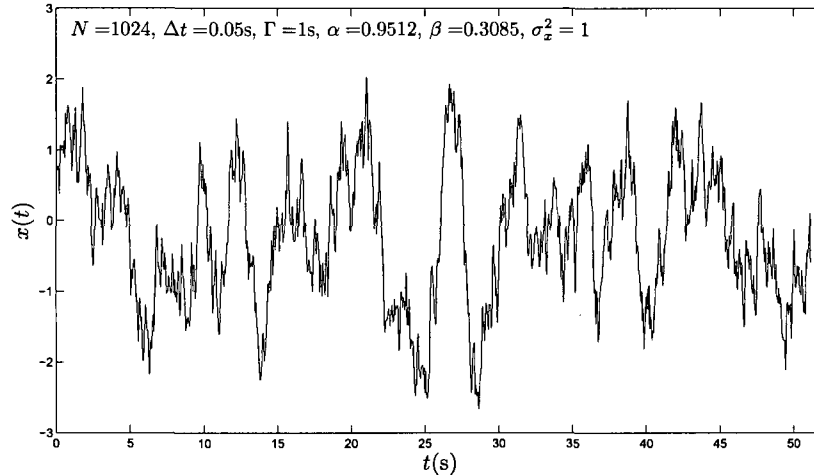


Figure 3.1: Gaussian-Markov process time series were generated with the following parameters $N = 1024$, $\Delta t = 0.05$ s, $\sigma_x^2 = 1$, $f_s = 20$ Hz.

Fig. 3.2 compares this PSD (labeled “Matlab 1-sided”) with the periodogram computed directly¹ using Eq. (3.6). The two spectra are almost identical as well as the area under each curve.

One-sided and two-sided PSDs of the Gaussian-Markov process estimated by MATLAB are compared in Fig. 3.3. As expected, the one-sided PSD is almost identical to twice the two-sided PSD.

¹To compare with the result obtained using MATLAB, I applied Eq. (3.6) to each of the sixteen sequences, and averaged.

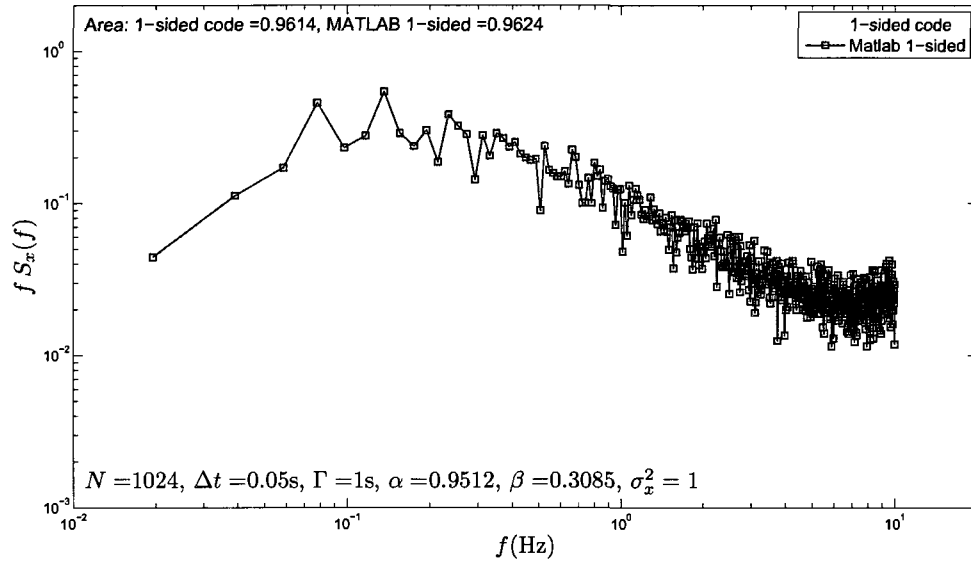


Figure 3.2: One-sided PSDs of Gaussian-Markov process by MATLAB and a standard code are almost identical. The areas under each curve, which represents the variance, are almost identical as well. This Gaussian-Markov process was artificially generated with indicated parameters. Note that the one-sided PSD by a standard code was plotted with the thicker line in order to differentiate it from the MATLAB PSD.

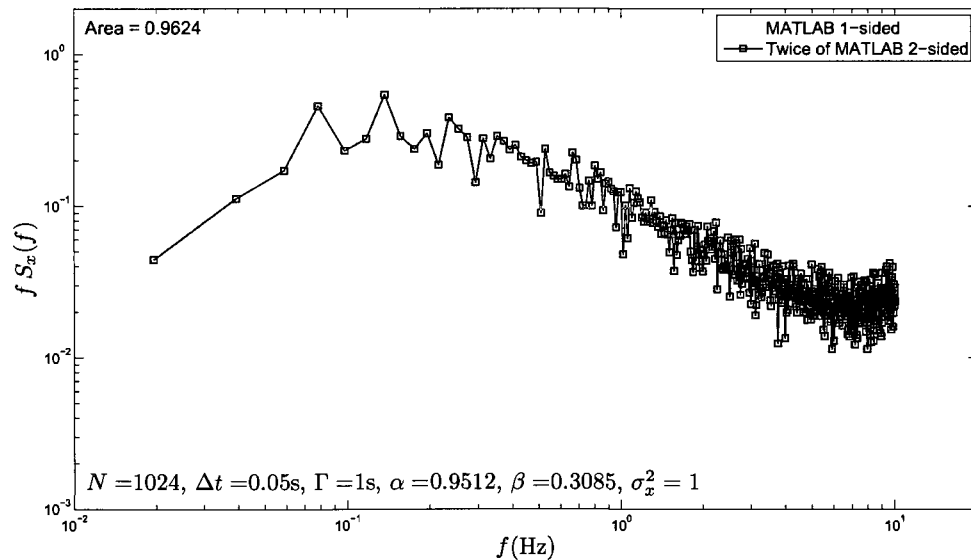


Figure 3.3: Comparison between one-sided and two-sided PSDs of Gaussian-Markov process estimated by MATLAB. The one-sided PSD is equal to twice of two-sided PSD. This Gaussian-Markov process was artificially generated with indicated parameters.

The analytical PSDs (Eq. 3.15 and 3.16) and those estimated by MATLAB are compared in Fig. 3.4. The one-sided analytical PSD nicely fits the one-sided MATLAB PSD, while the two-sided analytical PSD nicely fits the two-sided MATLAB PSD.

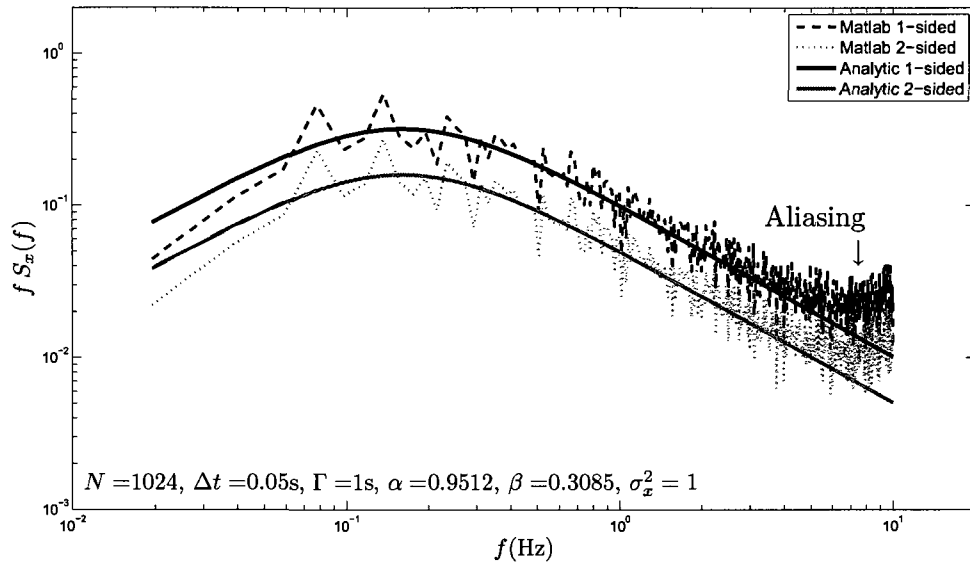


Figure 3.4: The analytical one-sided PSDs is best fit with the one-sided periodogram by MATLAB. Similar results for the two-sided PSD as well.

These results confirm that the one-sided PSDs estimated by MATLAB and by a standard (first-principles) code are equivalent and consistent with the known (analytical) spectrum. Therefore, one-sided PSD estimates provided by MATLAB can be used with confidence throughout my analysis.

3.6 Aliasing

From Fig. 3.4, there is aliasing observed at the high frequency end of the spectrum (near f_N). As stated earlier, the aliasing effect is caused by the folding to resolved frequencies of unresolved power at frequencies exceeding the Nyquist frequency. From

Eq. 3.16, the one-sided PSD of the Gaussian-Markov actually extends to infinity. Hence, the aliasing can be interpreted as the addition of some spurious power above the Nyquist frequency,

$$Al = \int_{f_N}^{\infty} S^{(1)}(f)df \quad (3.17)$$

Since

$$\begin{aligned} \int_0^{\infty} S^{(1)}(f)df &= \sigma^2 \\ &= \int_0^{f_N} S^{(1)}(f)df + \int_{f_N}^{\infty} S^{(1)}(f)df \end{aligned} \quad (3.18)$$

it follows that

$$\begin{aligned} Al &= \int_{f_N}^{\infty} S^{(1)}(f)df = \sigma^2 - \int_0^{f_N} S^{(1)}(f)df \\ &= \sigma^2 \left[1 - \frac{2}{\pi} \arctan(2\pi\Gamma f_N) \right] \\ &= \sigma^2 \left[1 - \frac{2}{\pi} \arctan(\pi\Gamma f_s) \right] \\ &= \sigma^2 \left[1 - \frac{2}{\pi} \arctan\left(\frac{\pi\Gamma}{\Delta t}\right) \right] \end{aligned} \quad (3.19)$$

Evidently the integral beyond the Nyquist frequency is not zero. This causes the aliasing effect at the high frequency end of the PSD. It is controlled by Γ and Δt . By using the parameters defined in the last section, the integral on the RHS of Eq. 3.19 is evaluated to be 0.99. Therefore, the contribution of aliased energy to the computed spectrum is 0.01.

Let's examine the aliasing effect further by generating Gaussian-Markov process signals with the same specification ($N=2048$, $\sigma_x^2 = 1$), but with differing Δt , Γ . The numerical results of the aliasing are shown in Table 3.1. At constant Γ , aliasing increases with increasing Δt . If Δt is fixed, aliasing decreases with increasing Γ .

Table 3.1: Aliasing effects of Gaussian-Markov process with $N=2048$ and $\sigma_x^2 = 1$.

$\Gamma = 1$ s,	Δt (s)	0.01	0.5	0.1
	<i>Al</i>	0.002	0.01	0.02
$\Gamma = 10$ s,	Δt (s)	0.1	1	5
	<i>Al</i>	0.002	0.02	0.1

3.7 Improving the PSD

We have seen that the PSD of the artificial Markov process as estimated by the periodogram is quite noisy – even when the PSD is formed as the average of sixteen periodograms. In my experience PSD’s computed from real atmospheric signals are even noisier. Hence, spectral smoothing is a necessary intervention.

Let’s generate a Gaussian-Markov time series with the following parameters, $N=32768$ ($=2^{15}$), $\sigma_x^2 = 1$, $\Delta t = 0.05$ s and $\Gamma = 1$ s. Its periodogram (labeled “raw”) and analytical PSD (labeled “analytic”) were plotted in Fig. 3.6. The raw periodogram is very noisy, and can be improved by these methods:

- Applying a data window to the raw signal. This will remove the discontinuity between beginning and end of the signal, by tapering the end points of the signal. There are many popular shapes of data windows, one example being the Hamming window (Fig. 3.5). In Fig. 3.6 (a), the 2^{15} -point Hamming window has been applied to the original time series. The new PSD (labeled “with 2^{15} Hamming window”) is somewhat less noisy than the raw one. The variance recovered from the area is very close to the raw and analytical variances.
- Block averaging the original time series before calculating the PSD (one may also apply a data window). This method will modify the high frequency end of the PSD, for what is computed is the PSD of an altered signal, formed from

the original by the operation of low-pass filtering. As shown in Fig. 3.6 (b), the new time series (labeled “block average”) was created by blocking average the original time series over 16 consecutive points of data (non-overlapping block). The ‘block average PSD,’ for which a 2048-point Hamming windows has been applied, is less noisy than the raw PSD. The variance recovered from the area is (of course) lower than the raw and analytical variance. The high frequency region of the true PSD is misrepresented (missing power), and for that reason aliasing is removed.

- Dividing the original time series into multiple shorter time series (each may overlap), then calculating the PSDs (may apply data window) of each shorter time series, and averaging all resulting PSDs together. This method will remove the low frequency power from the computed spectrum (since in effect one has high-pass filtered the signal), and is known as the ‘Welch’ method (Welch 1967). From Fig. 3.6 (c), the original time series has been divided into 16 non-overlapping blocks (where each block contains 2048 points). The periodograms (computed after application of a 2048-point Hamming window to each block) were averaged together to get the ‘Welch PSD’ (labeled “Welch”), which is much smoother than the raw one. However, the low frequency power is missing. The variance recovered from the area is very close to the raw and analytical variances.
- Averaging the PSDs in bins having constant logarithmic width. From Fig. 3.6 (d), the raw PSD has been averaged in 50 constant logarithmic bins. The ‘log average PSD’ (labeled “Log average”) is much smoother than the raw one. Its variance is very close to the variances of the raw and analytical PSDs. Similar to the Welch PSD, it is very consistent with the analytical PSD.

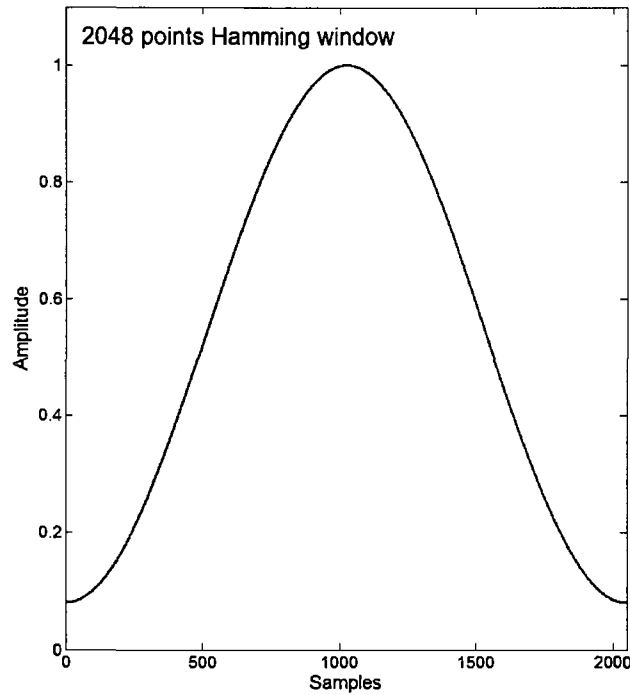


Figure 3.5: Shape of 2048 points Hamming window.

3.8 Empirical spectral formulae for atmospheric velocity spectra

In the balance of my thesis I will make use of formulae provided by others that summarize or encapsulate the measurements of the classical Kansas and Minnesota experiments. Our focus is the spectrum of the ‘longitudinal’ or ‘streamwise’ velocity fluctuation u' , as observed in the horizontally-homogeneous ABL. Needless to say, in order to provide an abstract formula covering a wide range of atmospheric conditions, it was necessary to discover how to “scale” the power spectrum — and indeed the search to optimize scaling of atmospheric velocity spectra still continues.

I concentrate on the spectrum in unstable (generally, daytime) stratification. In

the formulae I shall later use, the streamwise velocity spectrum for unstable stratification was divided into three spectral regions or wavebands (Kaimal 1978). Region I, which covers the high frequency region (or large wavenumbers), obeys Monin-Obukhov scaling, and in particular the relevant length scale is the height z . In this region spectral power rolls off in proportion to $f^{-5/3}$, as in the inertial subrange. In contrast in region III, which contains the spectral peak (and so may be called the energy containing region), the relevant length scale is the boundary layer depth (δ), rather than distance z from ground. Region III covers the low frequency region (or small wavenumbers) and scales with the mixed-layer (rather than Monin-Obukhov) scales. Region II is the transition between regions I and III, and is represented in the formulae by a straight line (in logarithmic axes) connecting the spectra of regions I and II. By combining all regions together, the u' spectrum of the unstable ASL is (Fig. 3.7)

$$\frac{f S_u(f)}{u_*^2 \phi_\epsilon^{2/3}} = \begin{cases} 0.3n^{-2/3}, & \lambda \leq 2z \quad \text{Region I} \\ 0.48 (2n)^{-q}, & 0.67\delta \geq \lambda \geq 2z \quad \text{Region II} \\ ABn/[1 + 3.1(Bn)^{5/3}], & \lambda \geq 0.67\delta \quad \text{Region III} \end{cases} \quad (3.20)$$

The spectral density is normalized on $u_*^2 \phi_\epsilon^{2/3}$ and expressed as a function of the normalized or dimensionless frequency:

$$n = \frac{f z}{\bar{u}} = \frac{z}{\lambda} \quad (3.21)$$

where wavelength λ is defined:

$$\lambda = \frac{\bar{u}}{f}. \quad (3.22)$$

The parameters in Eq. (3.20) are defined by:

$$A = \frac{(12 + 0.5|\delta/L|)^{2/3}}{1 + 0.75|z/L|^{2/3}} \quad (3.23)$$

$$B = \frac{\delta}{z} \quad (3.24)$$

$$q = \frac{\ln 0.44 A}{\ln 0.33 B} \quad (3.25)$$

The normalized TKE dissipation rate is defined as in Eq. 2.27. At the location of the spectral peak (in region III),

$$\left(\frac{fz}{\bar{u}}\right)_{peak} = 0.6469 \frac{z}{\delta} \quad (3.26)$$

This relation expresses the dependence of the spectral peak on the height of measurement. As z increases, the spectral peak moves to higher frequency. However, this move is expected to be very small, because δ is normally much bigger than z in most experiments. Region I seems to be the only one that clearly depends on height, e.g. spectral density of the u' spectra decreases with increasing height (Fig. 3.8 a). Once these spectra are normalized with $u_*^2 \phi_\epsilon^{2/3}$, their inertial subranges collapse together (Fig. 3.8 b).

Kaimal's model worked very well with the conditions given by the Minnesota experiment, $30 \leq -\delta/z \leq 367$ and $z \geq 4$ m. Its fit to observations deteriorated with increasing proximity to ground, and with approach to neutral stratification. Højstrup (1982) aimed to remedy these deficiencies, providing a spectral formula that divides the u' spectrum into (only) two regions, the low and the high frequency parts. The low frequency (or small wavenumber) region is similar to Kaimal's Region III, which adopts boundary layer depth as length scale and uses normalized frequency $n_\delta = f \delta/\bar{u}$. The high frequency (or large wavenumber) region depends on normalized frequency $n = f z/\bar{u}$. The u' spectrum of this model is normalized with u_*^2 and can

be written as (Liu and Ohtaki 1997)

$$\frac{f S_u(f)}{u_*^2} = \frac{0.5n_\delta}{1 + 2.2n_\delta^{5/3}} \left(-\frac{\delta}{L}\right)^{2/3} + \frac{105n}{(1 + 33n)^{5/3}} \quad (3.27)$$

At the spectral peak, $n_{\delta,\text{peak}} = 0.7947$. This also leads to a relation linking the spectral peak to height. Similar to Kaimal's model, Højstrup's spectral peak moves to higher frequency as z increases (although the shift, in practise, is almost unnoticeable).

$$\left(\frac{fz}{\bar{u}}\right)_{\text{peak}} = 0.7947 \frac{z}{\delta} \quad (3.28)$$

Fig. 3.9 compares Kaimal's and Højstrup's spectra for the same atmospheric conditions. They are almost identical in unstable stratification and far from ground (Fig. 3.9 (1)). The two curves begin to deviate in the low frequency region as it is less unstable (Fig. 3.9 (2)) or closer to the ground (Fig. 3.9 (3)). However, the locations of the spectral peaks do not change very much. The difference between these two curves is maximal near ground and in nearly neutral stratification (Fig. 3.9 (4)). Note that in the inertial subrange both curves agree very well under all conditions. The Højstrup spectra vary with height as well, especially in the inertial subrange, where the u' spectral densities decrease with height. Their inertial subranges also collapse, when normalized with $u_*^2 \phi_\epsilon^{2/3}$.

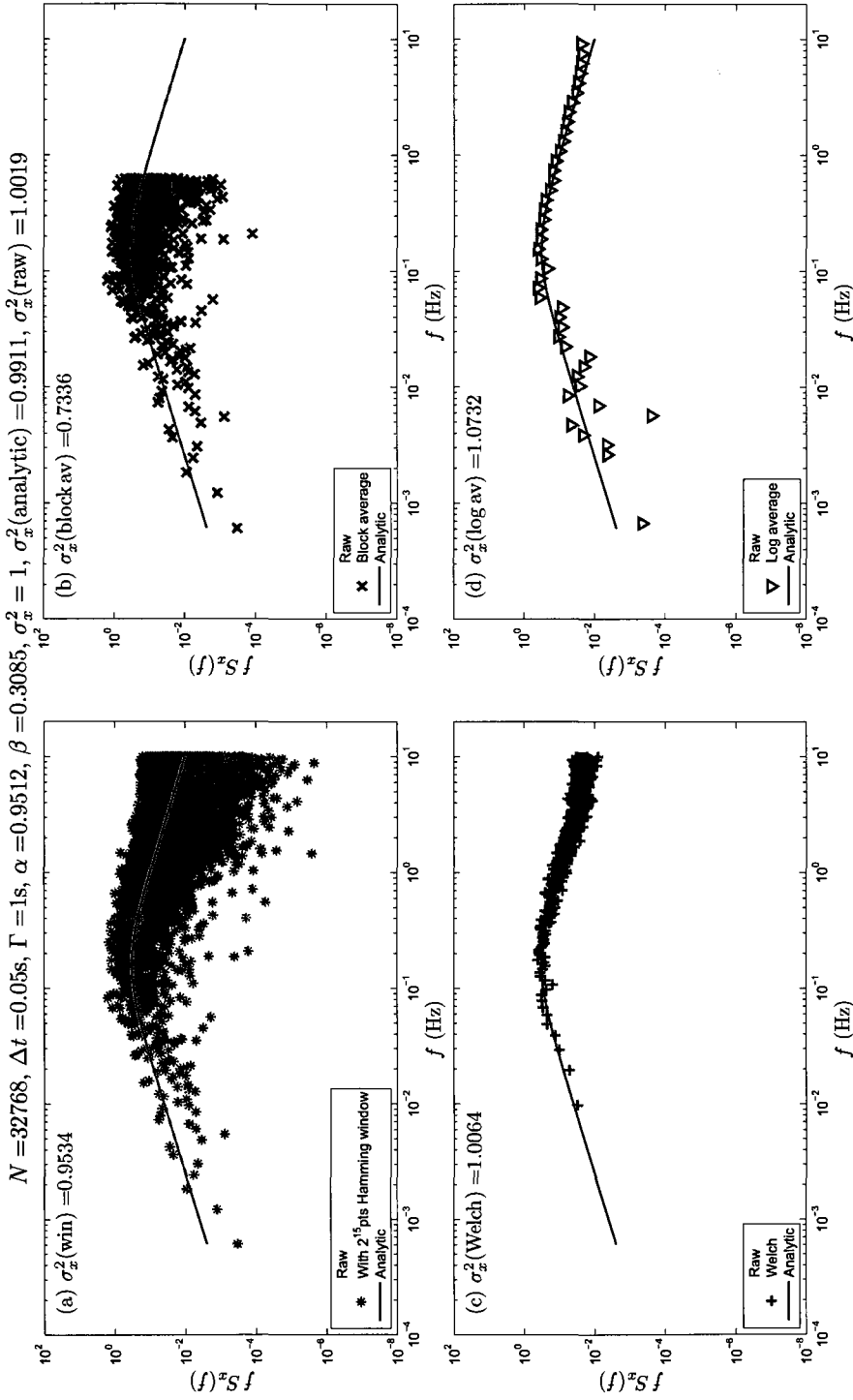


Figure 3.6: The PSD estimation by periodogram ('raw') of Gaussian-Markov process with above indicated parameters, is very noisy. (a) By applying the 2^{15} -point Hamming window, the new PSD ('with 2^{15} pts Hamming window') is less noisy. (b) By block averaging the original time series over 16 consecutive points of data (blocks are non-overlapping), the resulting 'block average PSD' ('Block average') is less noisy than the raw one, but information (or misinformation) in the high frequency region (including the aliasing effect) is removed. (c) The original time series was divided into 16 non-overlapping blocks (each with 2048 points of data), the periodograms (computed after applying the 2048-point Hamming window to each block) were averaged together to get the 'Welch PSD' ('Welch'). This is much smoother than the raw PSD, but provides no information in the low frequency region. (d) The raw PSD has been smoothed by block averaging in 50 bins of equal width on the log(frequency) axis. The 'log average' PSD ('Log average') is much smoother than the raw one. All of the improved PSD's are very consistent with the analytical PSD ('Analytic'), and especially so the Welch and the log average PSD. The variances recovered from the area under each plot are very close to the variance of the raw and analytical PSD's, except in the case of the block average PSD.

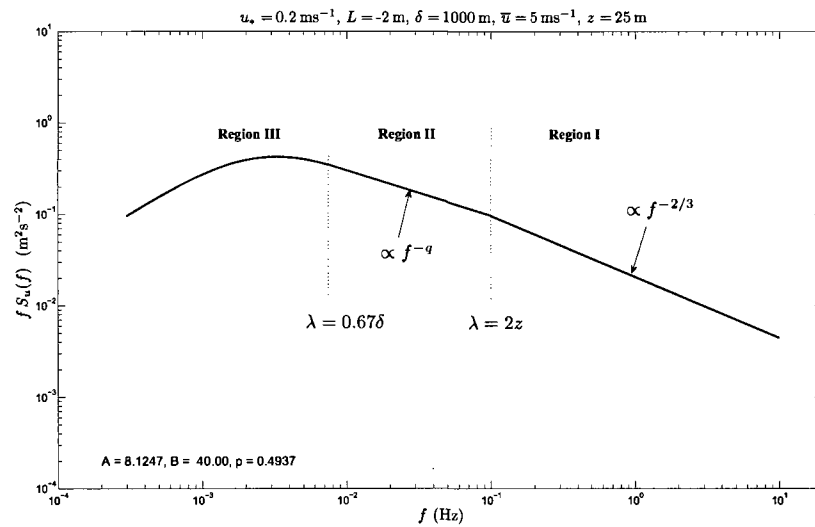


Figure 3.7: The theoretical u' spectrum from Eq. 3.20 (Kaimal 1978) is divided into 3 regions. Region I is the inertial subrange region, which obeys MOST, and its u' spectrum decreases with $f^{-5/3}$. Region III, which models the mixed-layer u' spectrum, depends on the boundary layer depth (δ). Region II is the transition between regions I and III, which is proportional to f^{-q} . The spectral curve in this figure was artificially generated with indicated parameters.

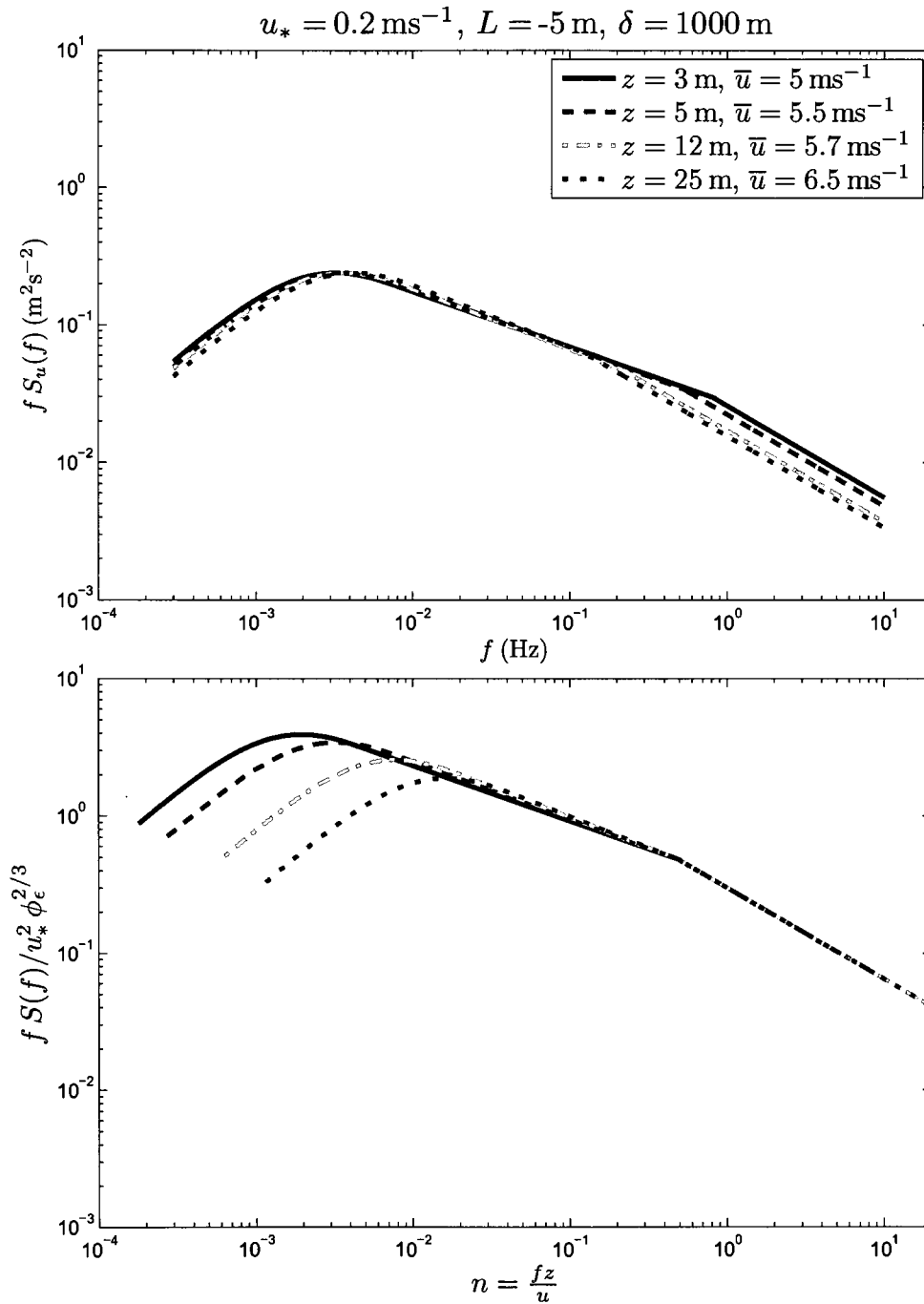


Figure 3.8: Various Kaimal u' spectra were artificially generated in similar atmospheric conditions at different heights. The variations are almost unnoticeable in region II and III. However in region I, the u' spectra clearly decrease with height. Their inertial subranges collapse together, when normalized with $u_*^2 \phi_\epsilon^{2/3}$.

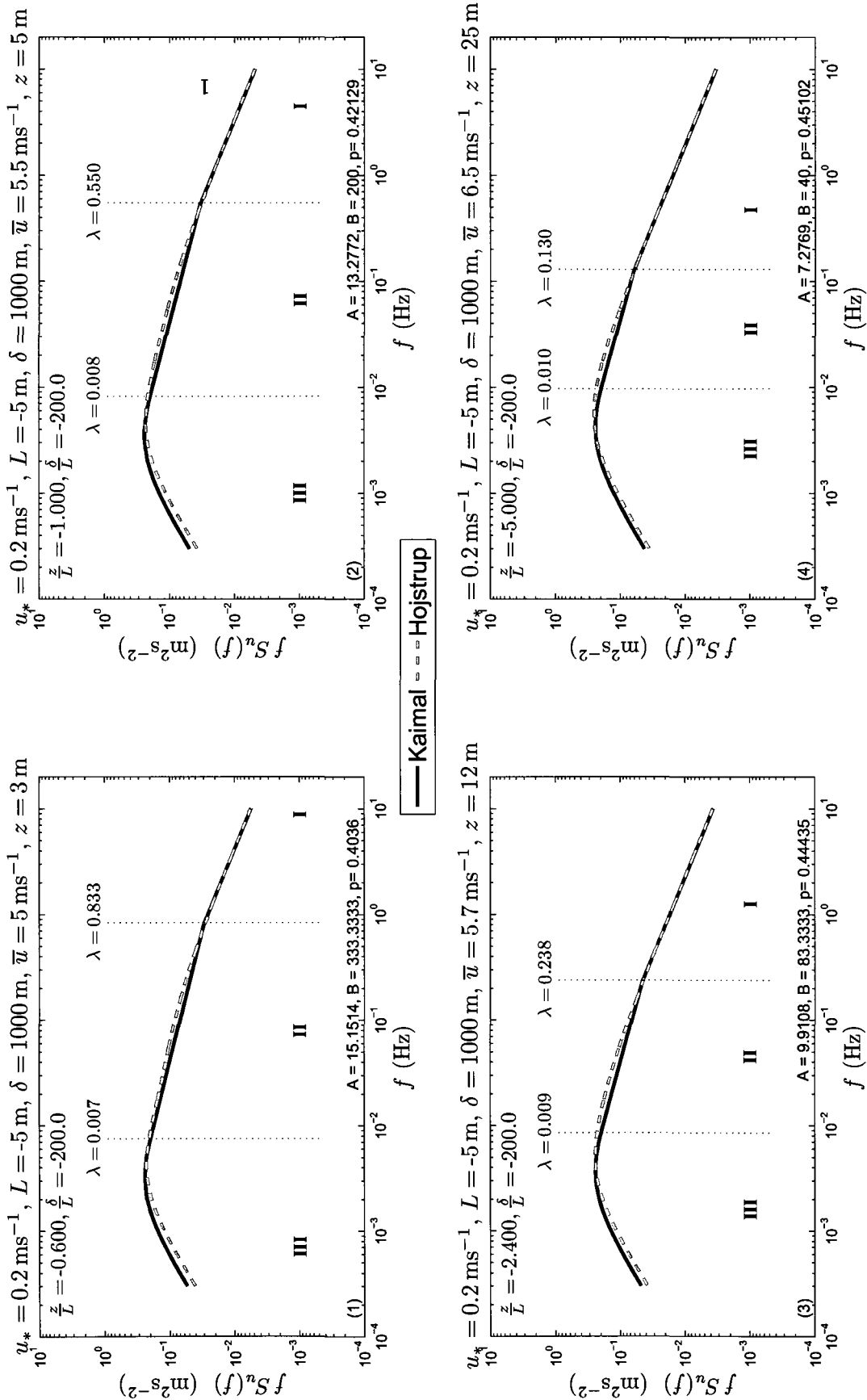


Figure 3.9: Kaimal's and Højstrup's spectra were artificially generated at different conditions. Both of them are almost identical in unstable stratification and away from ground (1). The differences become bigger close to the ground (3) or in less unstable stratification (2) and are maximal near ground in near neutral conditions (4).

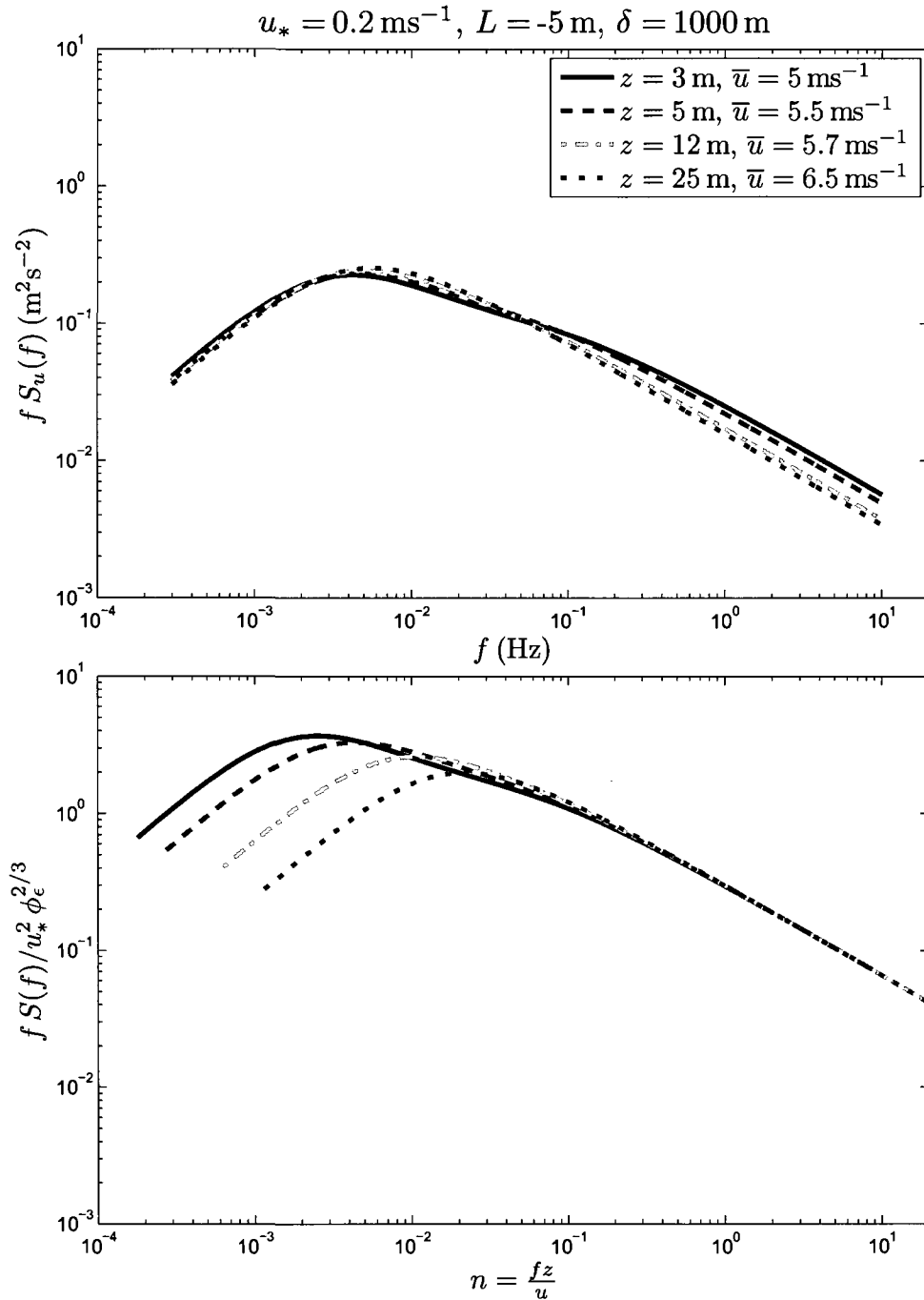


Figure 3.10: Various Højstrup u' spectra were artificially generated in similar atmospheric conditions at different heights. Similar to Kaimal's spectra, the u' spectral densities decrease with height in the inertial subrange. If these curves are normalized with $u_*^2 \phi_\epsilon^{2/3}$, their inertial subranges collapse together.

Chapter 4

Experimental background and data preparation

Previous chapters have set the stage for my examination of velocity spectra from measurements made (by others) over a salt flat in Western Utah. In particular, Chapter 3 documented the method I have used to compute velocity spectra. This chapter briefly covers details of the experiment and analysis.

The Dugway experimental site is normally known as SLTEST (the surface layer turbulence and environmental science test) or Dugway Proving Grounds. It is located in the desert of Western Utah at $113^{\circ}27.5'W$ and $40^{\circ}8.50'N$ (Fig. 4.1). The site's surface is ideally flat, thus very suitable for ASL experiments. This experiment was performed during May 23, 2005 - Jun 2, 2005, and it was expected that winds would blow from the North. The time zone of Utah is Mountain Daylight time (MDT=GMT-6 hours) during summer, and Mountain Standard time (MST=GMT-7 hours) during winter (GMT is Greenwich Mean time).

4.1 Instrumentation

In the Dugway 2005 experiment a total of 18 sonic anemometers (CSAT3 Campbell Scientific Inc.) synchronously sampled the three components of wind veloc-

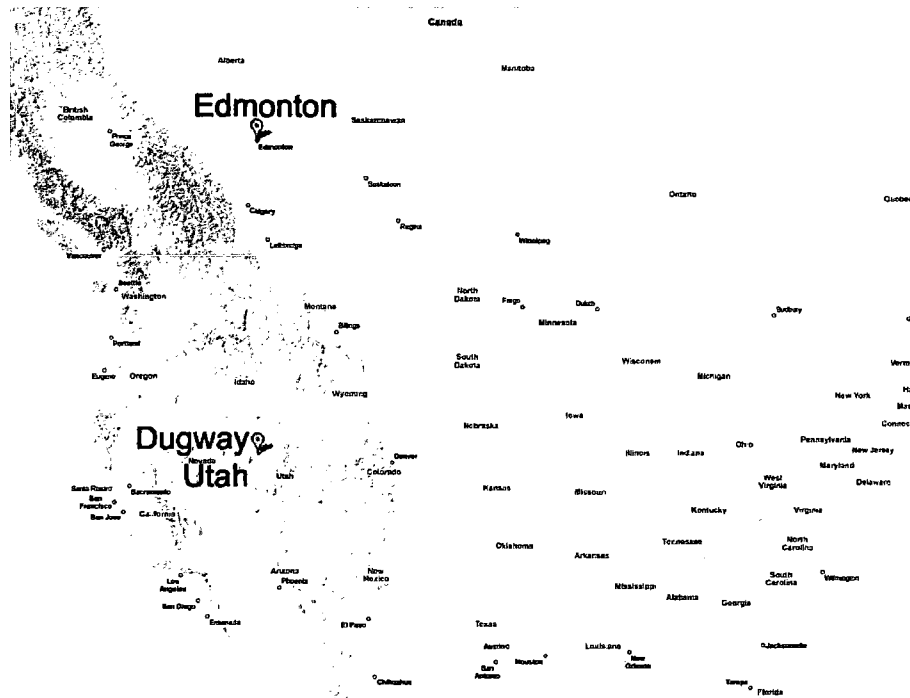


Figure 4.1: Location of Dugway experiment (map generated by Google Maps).

ity (u, v, w) and temperature (T) , at sampling frequency 20 Hz. All anemometers were oriented (by eye) to face a peak on the horizon, nominally marking the North. The first nine anemometers (nos. 1-9) were placed on a tall tower at heights $z = (1.42, 2.14, 3.00, 4.26, 6.14, 8.71, 12.52, 17.94, 25.69)$ m above ground. The remaining instruments (nos. 10-18) were placed on a cross-wind transect at 3 m above ground; six of the transect sonics stood west of the tower, and three east of the tower. For the runs analysed in my thesis, instruments on the transect were separated laterally from each other by 10 m. In order to define the horizontal position of each transect sonic (x) , the position of the tower was treated as a reference point. For all the transect sonics on the west of the tower, x gives the negative of the distance between a given transect sonic and the tower, while for the sonics on the east transect, x gives the distance from the tower to the given sonic.

Therefore, from the west to east of the transects sonics, the horizontal positions are $x = (-60, -50, -40, -30, -20, -10, 0, 10, 20, 30)$ m. Fig. 4.2 shows the experimental setup at the Dugway site. Please note that all the sonic anemometers had been checked by their manufacturer immediately prior to the experiment.

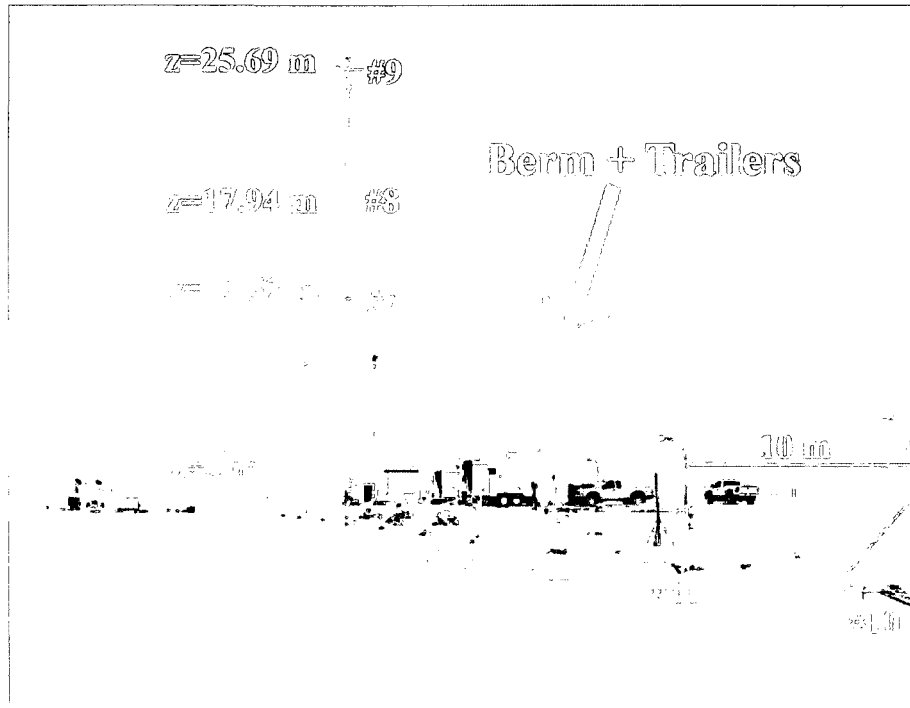


Figure 4.2: Instrumental setup at Dugway site. Sonic anemometers nos. 1-9 were mounted on the tower at different heights above ground, while nos. 10-18 were mounted on the transect at 3 m above ground. They were all facing the North. Near this array of sonic anemometers, there is a berm, which is 0.8 m higher than the desert surface. This berm and many trailers certainly disturb the flow nearby.

4.2 Flow disturbance

During the experimental setup, the desert surface was very wet and consequently too soft to permit equipment to drive on it. Hence the tower and transect were established rather too close to a parking area or berm, which elevated above the desert surface by 0.8 m. Furthermore during the measurements several large trailers

were parked on the berm (Fig. 4.2). The berm and the trailers certainly disturbed the nearby flow, therefore the data selection has to be made carefully.

As observed from the recorded data from sonic anemometers mounted 3 m above ground (Fig. 4.3), most runs show that the mean streamwise velocity (\bar{u}) – here averaged over 1-hr periods – starts to drop at the sonic anemometer no. 14 or 15 (20 or 30 m west of the tower). If we accept the proposition that the flow is horizontally homogeneous remote from the road and berm, then this decrease must be caused by the flow disturbance from the berm and obstacles. Therefore, analysis of the transects should include only the sonic anemometers nos. 10-13 ($x = -60\text{m}$, -50m , -40m and -30m respectively)

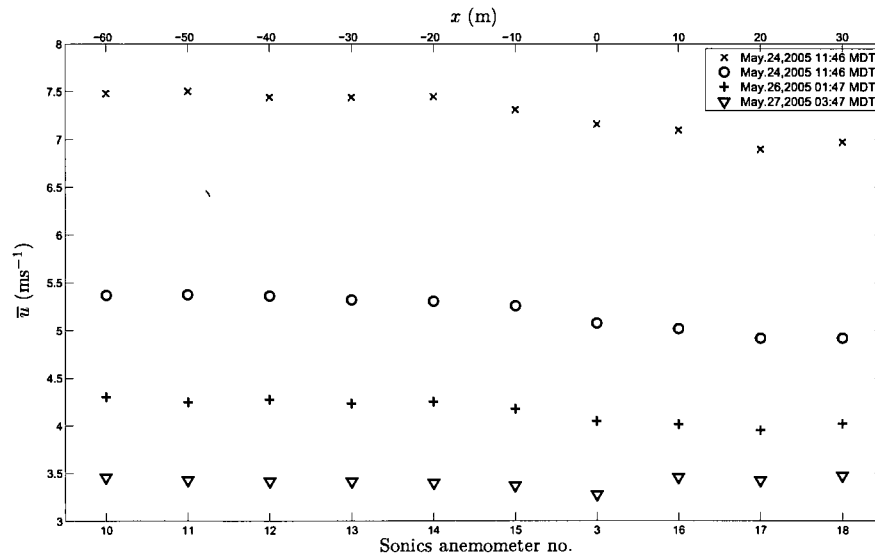


Figure 4.3: Dugway’s mean streamwise velocities \bar{u} recorded by sonic anemometers on the transect at 3 m above ground.

This does not establish to what *height* the obstacles may have disturbed the flow measured on the tower. The roof of the tallest trailer stood 3.2 m above the berm, or 4 m above the desert surface. To exclude flow disturbance, the analysis should be restricted to instruments somewhat higher than that. Therefore, only sonic anemome-

ters no.6 (at $z = 8.71$ m) and above on the tower have been taken into account. In conclusion, to avoid processing signals that had been subject to the flow disturbance, the present analysis considers sonic anemometers nos. 6-13 only.

4.3 Other remarks

This experimental site belongs to a military base. Regulations required that the site be unattended during the weekend (late evening of May 27 to morning of May 30, 2005). Thus the data collected from the evening of May 27 to the early morning of May 30 were not included in the analysis. Furthermore, during May 30 to Jun 2 rain occurred, which certainly affected the accuracy of the sonic anemometers. There was also an interval of southerly winds during this period. Therefore, those data also were excluded from the analysis. Thus the analysis includes only the record up until around 20:00 MDT of May 27.

4.4 Data preparation and period of calculation

During the experiment, unknown circumstances occasionally caused a defect in the recorded data, i.e. one or more signals occasionally registered a 'NaN' (not a number). This kind of data can not be calculated numerically and would need to be fixed before further calculation. However since there were few runs containing one or more NaN's, all such were rejected in my analysis.

The spectral calculations in this thesis follow the method used to compute the 'Kansas' spectra (Kaimal et al. 1972), which were based on records of approximately 1 hour ($2^{16} = 65536$ points of data or 54.61 minutes). Hence all other calculations have been conducted with the same interval as well.

4.5 Coordinate rotation

The analysis in this thesis was based on the streamline coordinate system, whose x -axis points along the mean wind direction. At the beginning of the experiment, all the sonic anemometers were aligned to point north, i.e. were oriented for best accuracy in northerly winds. During the period of this analysis, winds were indeed from the north quadrants.

To focus on velocity statistics in the streamline coordinate system I performed a double coordinate rotation (Wilczak et al. 2001). The first rotation set $\bar{v} = 0$ by rotating the x - and y -axes about the z -axis through angle θ (also known as mean wind direction), which is

$$\theta = \arctan\left(\frac{\bar{v}_m}{\bar{u}_m}\right) \quad (4.1)$$

(where subscript m denotes the velocities measured in the individual coordinate frame of the sonic anemometer). The new velocities after this first rotation become

$$u_1 = u_m \cos \theta + v_m \sin \theta \quad (4.2)$$

$$v_1 = -u_m \sin \theta + v_m \cos \theta \quad (4.3)$$

$$w_1 = w_m. \quad (4.4)$$

The second rotation, by angle ϕ , rotates the x_1 - and z_1 -axes about the y_1 -axis, where

$$\phi = \arctan \frac{\bar{w}_1}{\bar{u}_1} \quad (4.5)$$

This rotation sets the mean vertical velocity to zero ($\bar{w}_2 = 0$) and aligns the x_2 -axis in the streamline direction as well as setting the z_2 -axis along the real vertical axis. The transformed instantaneous velocities (denoted by subscript 2) after the second

rotation are

$$u_2 = u_m \cos \phi + w_1 \sin \phi \quad (4.6)$$

$$v_2 = v_m \quad (4.7)$$

$$w_2 = -u_m \sin \phi + w_m \cos \phi \quad (4.8)$$

After these two rotations, the recorded time series are ready for further analysis.

Chapter 5

Analysis of intervals of unstable stratification

In this chapter, MOST parameters were calculated from post-rotation Dugway data for all measurement intervals up until 20:00 MDT on May 27. Then runs meeting selection criteria were tested against MOST by comparing their normalized standard deviations in vertical velocity and temperature with the results of previous ASL experiments. Consistency with the earlier ASL experiments would confirm the validity of MOST as basis for interpretation of the Dugway experiment.

5.1 Basic MOST parameters

In order to calculate MOST parameters, many velocity and temperature statistics were needed, e.g. mean, standard deviation, variance of each time series. I then used these values to calculate fluctuations times series and the following covariances:

kinematic momentum flux densities : $\overline{u'w'}$, $\overline{v'w'}$

kinematic heat flux density : $\overline{w'T'}$

The MOST scaling parameters (L, u_*, T_*) can be calculated according to Eqs. 2.14 - 2.15. The average values from sonic anemometers nos. 10-13 were used in place of

momentum and heat fluxes at the surface, while the average temperature over sonic anemometers nos. 6-13 was used in place of T_0 . Hence,

$$u_* = [(\overline{u'w'})_h^2 + (\overline{v'w'})_h^2]^{1/4} \quad (5.1)$$

$$T_* = -\frac{(\overline{w'T'})_h}{u_*} \quad (5.2)$$

$$L = -\frac{u_*^3}{k_v \left(\frac{g}{T_{av}}\right) (\overline{w'T'})_h} \quad (5.3)$$

with

$$(\overline{u'w'})_h = \frac{1}{4} \sum_{i=10}^{13} (\overline{u'w'})_i$$

$$(\overline{v'w'})_h = \frac{1}{4} \sum_{i=10}^{13} (\overline{v'w'})_i$$

$$(\overline{w'T'})_h = \frac{1}{4} \sum_{i=10}^{13} (\overline{w'T'})_i$$

$$T_{av} = \frac{1}{8} \sum_{i=6}^{13} \overline{T}_i$$

where subscript i is to identify each sonic anemometer. These MOST parameters capture the atmospheric condition during each run. The next step was to choose the data suitable for further analysis, for which purpose I used the selection criteria described in the next section.

5.2 Data selection

Since my first analysis was focused on the unstable stratification, only the runs with negative Obukhov length were included. Other than this, there were still factors to consider, e.g. rain, and flow disturbance. My selection criterion can be summarized as follows:

1. Unstable stratification: $L < 0$ m
2. Daytime runs: 1 hour after sunrise until 1 hour before sunset (See Table 5.1).
3. Northerly wind: mean wind direction averaged over 8 sonic anemometers $|\bar{\theta}_8| \leq 30^\circ$. Since all the sonic anemometers were facing north, the optimized wind direction that the sonic anemometers can record properly lie with in this range.
4. Wind not too weak: $u_* \geq 0.1$ m s⁻¹. This is to make sure that the recorded signal levels were much larger than the level of instrumentation noise.
5. To avoid the flow disturbance caused by the berm and trailers, only the data from the sonic anemometers nos. 6-13, which were the top 4 sonic anemometers on the tower and the 4 sonic anemometers on the west side of the tower were considered
6. No NaN entries in each run.

Table 5.1: Sunrise and sunset time in Dugway, Utah (112°45'W and 40°14'N).

Date	Sunrise (MST)	Sunset (MST)
May 24, 2005	5:08 am	7:48 pm
May 25, 2005	5:07 am	7:49 pm
May 26, 2005	5:06 am	7:50 pm
May 27, 2005	5:06 am	7:51 pm
May 28, 2005	5:05 am	7:52 pm

Data taken from U.S. Naval Observatory (<http://www.usno.navy.mil/>).

After this selection, there remained 34 unstable runs (Table 5.2), whose results were tested against MOST.

Table 5.2: MOST parameters for runs selected by the criteria: $L < 0$ m, $|\bar{\theta}_8| < 30^\circ$ and $u_* \geq 0.1 \text{ ms}^{-1}$. The time stated in this table is the mid-period time.

Date/Time (GMT)	Date/Time (MDT)	u_* (m s^{-1})	L (m)	T_* (K)
May 24,2005 14:46	May 24,2005 08:46	0.274	-47.69	-0.115
May 24,2005 15:46	May 24,2005 09:46	0.295	-25.10	-0.255
May 24,2005 16:46	May 24,2005 10:46	0.332	-21.39	-0.380
May 24,2005 17:46	May 24,2005 11:46	0.260	-8.67	-0.579
May 24,2005 18:46	May 24,2005 12:46	0.255	-6.52	-0.745
May 24,2005 19:46	May 24,2005 13:46	0.194	-2.91	-0.963
May 24,2005 20:46	May 24,2005 14:46	0.260	-6.83	-0.743
May 24,2005 21:46	May 24,2005 15:46	0.215	-3.98	-0.874
May 25,2005 00:47	May 24,2005 18:47	0.287	-12.09	-0.516
May 25,2005 17:47	May 25,2005 11:47	0.259	-8.42	-0.583
May 25,2005 18:47	May 25,2005 12:47	0.243	-5.77	-0.754
May 25,2005 19:47	May 25,2005 13:47	0.220	-3.69	-0.972
May 25,2005 20:47	May 25,2005 14:47	0.142	-1.12	-1.347
May 25,2005 21:47	May 25,2005 15:47	0.192	-2.76	-1.000
May 25,2005 22:47	May 25,2005 16:47	0.147	-1.35	-1.197
May 25,2005 23:47	May 25,2005 17:47	0.167	-2.14	-0.972
May 26,2005 00:47	May 25,2005 18:47	0.203	-5.16	-0.602
May 26,2005 14:47	May 26,2005 08:47	0.184	-32.49	-0.076
May 26,2005 15:47	May 26,2005 09:47	0.207	-13.46	-0.233
May 26,2005 16:47	May 26,2005 10:47	0.201	-6.96	-0.427
May 26,2005 18:47	May 26,2005 12:47	0.156	-1.98	-0.911
May 26,2005 19:47	May 26,2005 13:47	0.148	-1.58	-1.036
May 26,2005 20:47	May 26,2005 14:47	0.180	-2.70	-0.903
May 26,2005 21:47	May 26,2005 15:47	0.112	-0.70	-1.354
May 26,2005 22:47	May 26,2005 16:47	0.182	-3.54	-0.708
May 27,2005 14:47	May 27,2005 08:47	0.146	-27.15	-0.058
May 27,2005 15:47	May 27,2005 09:47	0.203	-15.95	-0.191
May 27,2005 16:47	May 27,2005 10:47	0.191	-7.16	-0.379
May 27,2005 18:47	May 27,2005 12:47	0.152	-2.78	-0.619
May 27,2005 19:47	May 27,2005 13:47	0.171	-2.88	-0.758
May 27,2005 20:47	May 27,2005 14:47	0.211	-7.17	-0.470
May 27,2005 22:47	May 27,2005 16:47	0.115	-1.23	-0.820
May 27,2005 23:47	May 27,2005 17:47	0.144	-2.83	-0.556
May 28,2005 00:47	May 27,2005 18:47	0.166	-6.72	-0.312

5.3 Normalized standard deviation in vertical velocity ($\phi_w = \sigma_w/u_*$)

I began by examining whether Monin-Obukhov scaling would organize the observed values of the standard deviation in vertical velocity. According to MOST, the property $\phi_w = \sigma_w/u_*$ is a universal function of z/L . From the earlier authors, in unstable stratification this function is bounded by neutral and free convection limits (Monji 1973), which suggest the functional form

$$\phi_w = C_{w1} (1 + C_{w2} |z/L|)^{1/3}, \quad (5.4)$$

where C_{w1} and C_{w2} are free parameters. As $|z/L|$ approaches zero (neutral stratification), ϕ_w approaches C_{w1} (neutral limit). On the other hand, under very unstable conditions (large $|z/L|$), ϕ_w is proportional to $|z/L|^{1/3}$ as in free convection. By using a non-linear least squares fitting with the 1 hr Dugway data, I obtained the result that

$$\frac{\sigma_w}{u_*} = 0.96 (1 + 5.8 |z/L|)^{1/3} \quad (5.5)$$

That is,

$$C_{w1} = 0.96 \text{ and } C_{w2} = 5.8$$

with $R^2 = 0.97$. From this equation, its neutral limit is 0.96 and ϕ_w starts to vary with $|z/L|^{1/3}$ at about $|z/L| \gtrsim 3$. Fig. 5.1 shows the 1-hr Dugway statistic of ϕ_w and its least square fitting (Eq. 5.5) as well as the formula of Eq 2.29 (Wilson 2008) based on 30-min statistics (neutral limit 1.0; ϕ_w varying with $|z/L|^{1/3}$ at $|z/L| \gtrsim 1.5$). The 1-hr and 30-min statistics agree well with each other, but both differ greatly from the standard formulation in Eq. 2.28 (Panofsky et al. 1977), whose neutral limit is 1.3. A similar disparity (relative to the paradigm of 1.3 as the neutral limit) is also reported by Högström (1990), Moraes (2000) and Pahlow et al. (2001).

5.4 Normalized standard deviation in temperature ($\phi_T = \sigma_T/|T_*|$)

Unlike the wind velocity fluctuation, the temperature fluctuation is “unusual” (Tillman 1972). Its distribution clearly deviates from Gaussian and its time series also shows some unique characteristics, as seen in Fig. 5.2. Almost all T' distributions at Dugway during unstable stratification were positively skewed.

Tillman (1972) suggested that a high-pass filter should be applied to the original temperature time series, in order to remove any variation or trend due to scales of motion larger and slower than “turbulence” (e.g. mesoscale or synoptic scale variation). In my analysis, a high-pass filter has been applied by subtracting from the original temperature time series a 72 second (or 1441 point) running mean. The 72 second running mean of time series x_i (low-pass filter) is defined as

$$\tilde{x}_i = \frac{1}{1441} \sum_{j=i-720}^{i+720} x_j \quad (5.6)$$

The new time series after removing the running mean is the high-pass filtered series

$$\hat{x}_i = x_i - \tilde{x}_i \quad (5.7)$$

(I henceforth drop the ‘hat’). This new time series spans indices $i = 721$ to $i = 2^{16} - 720$. Once applied, this high-pass filter renders Dugway T' distributions that are less skewed (Fig. 5.3).

Similar to σ_w/u_* , the normalized temperature standard deviation $\sigma_T/|T_*|$ under unstable condition is bounded by neutral and free convective limits (Monji 1973, Tillman 1972). It is best described by

$$\phi_T = C_{T1} (1 + C_{T2} |z/L|)^{-1/3}, \quad (5.8)$$

where C_{T1} and C_{T2} are free parameters. This function approaches the neutral limit (small $|z/L|$) of C_{T1} and varies with $|z/L|^{-1/3}$ in the convective limit (large $|z/L|$).

The Dugway 1-hr values of $\sigma_T/|T_*|$ before and after high-pass filtering were plotted against $|z/L|$ in Fig. 5.4. Application of the high-pass filter made $\sigma_T/|T_*|$ less scattered. The non-linear curve best fitting $\sigma_T/|T_*|$ after high-pass filtering is

$$\phi_T = 2.9 (1 + 22 |z/L|)^{-1/3} , \quad (5.9)$$

with $R^2 = 0.97$. Its neutral limit is 2.9 and ϕ_T varies with $|z/L|^{-1/3}$ at $|z/L| \gtrsim 0.8$. This equation along with the earlier result by Kaimal and Finnigan (1994) from Eq. 2.30, which reaches a neutral limit at 2, and Tillman (1972) from Eq. 2.31, which has a neutral limit of 2.6 and varies with $|z/L|^{-1/3}$ at $|z/L| \gtrsim 3$, were plotted in Fig. 5.4. The Dugway data resemble Tillman's result more closely than that of Kaimal.

Observed values of σ_w/u_* and $\sigma_T/|T_*|$ from the Dugway experiment are broadly consistent with those of earlier experiments, and scale reasonably well with Monin-Obukhov scaling. On this evidence — though only if we overlook the fact that the neutral limit for σ_w/u_* may not in fact be universal — we might conclude MOST is a satisfactory scaling theory for the unstable ASL.

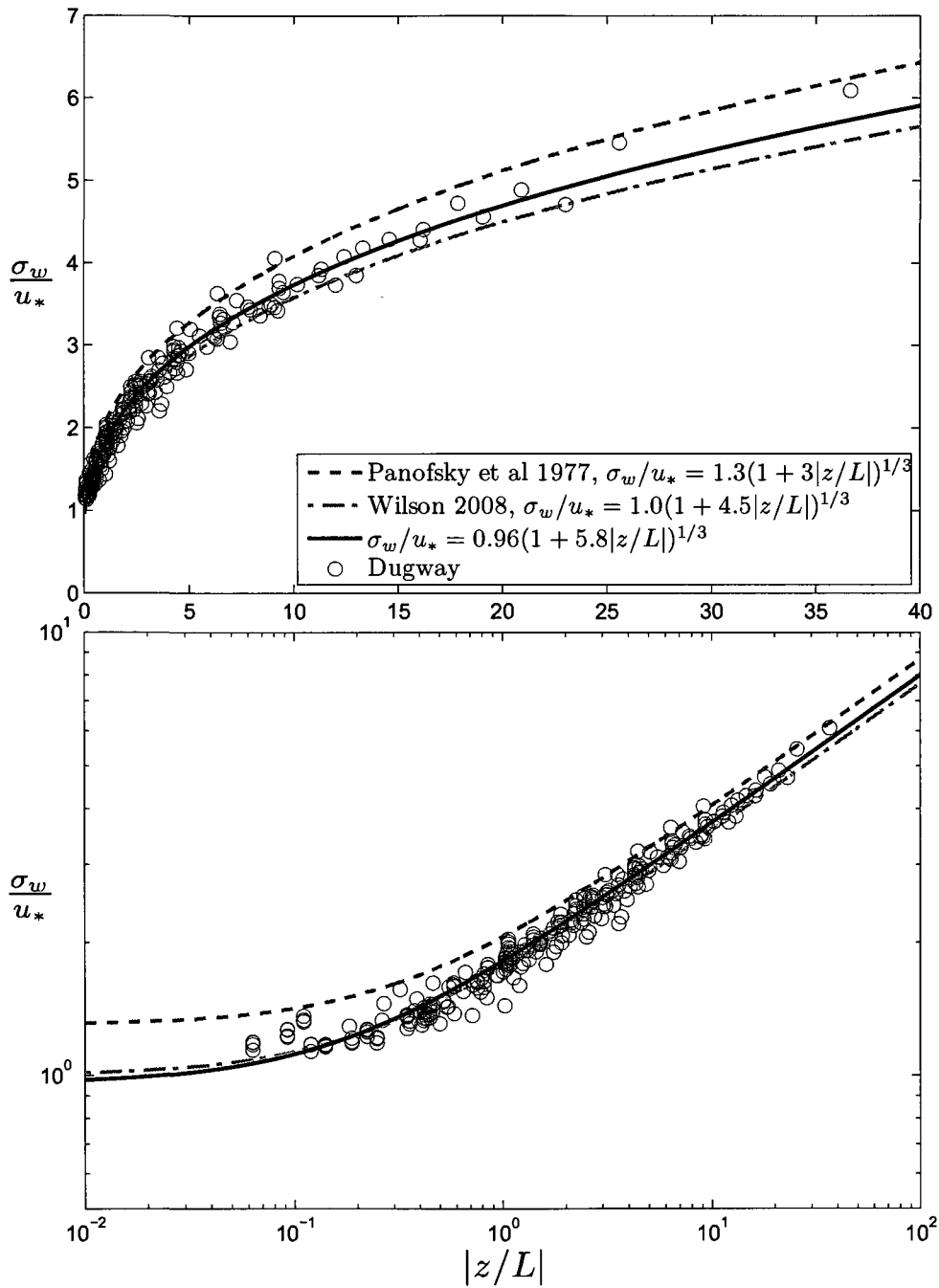


Figure 5.1: Dugway's 1 hr statistic of $\frac{\sigma_w}{u_*}$ for unstable stratification in linear- and log-log axes, and its non-linear least square curve $\frac{\sigma_w}{u_*} = 0.96(1 + 5.8|z/L|)^{1/3}$. Its neutral limit is 0.96, which is close to the neutral limit of 30 minutes statistic (Wilson 2008) of 0.8 as described by $\frac{\sigma_w}{u_*} = 0.8(1 + 9.5|z/L|)^{1/3}$. However, it is quite different from the standard value 1.3 (Panofsky et al. 1977), obtained from $\frac{\sigma_w}{u_*} = 1.3(1 + 3|z/L|)^{1/3}$. (Selection criterion: $L < 0$ m, $|\bar{\theta}_8| < 30^\circ$ and $u_* > 0.1$ m s $^{-1}$.)

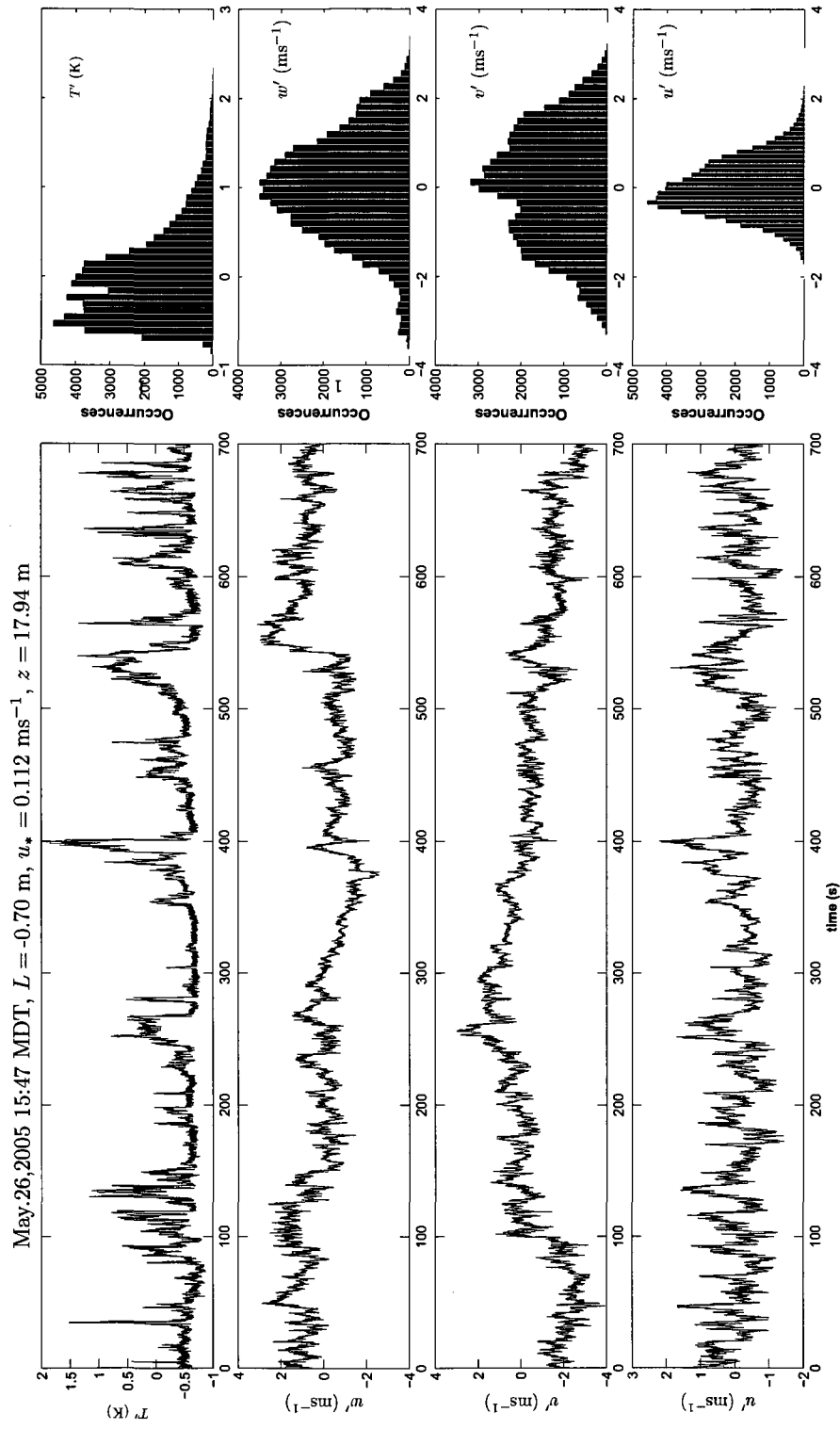


Figure 5.2: Time series of 3 components of wind velocity and temperature fluctuations of the sonic anemometers no. 8 ($z = 17.94$ m) at 15:47 MDT of 26 May 2005 are shown on the left hand side, while on the right hand side are their histograms. The T' time series differs very visibly from the velocity fluctuation time series. From the histograms, the T' distribution is positively skewed, while the distributions of velocity fluctuation are approximately Gaussian.

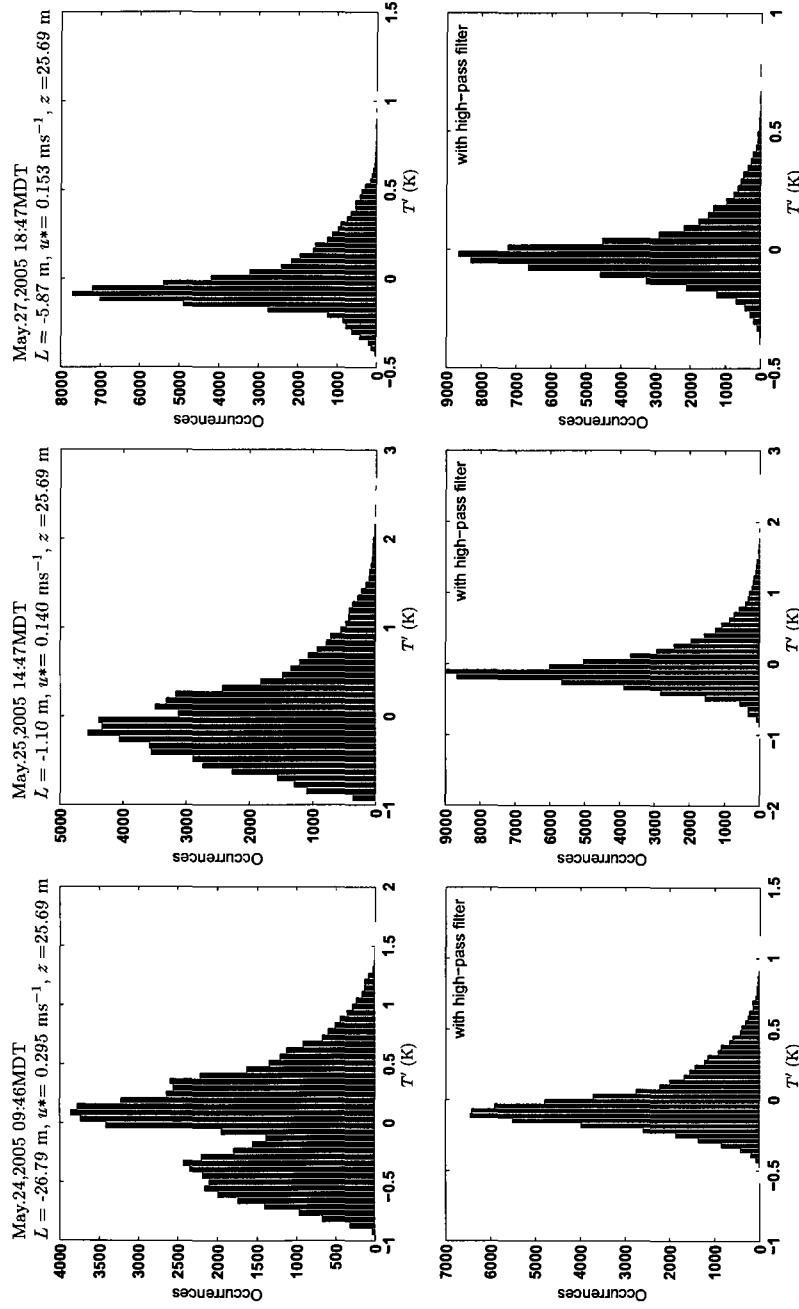


Figure 5.3: T' distributions before (upper) and after (lower) removing a 72 second running mean; showing 3 different runs of the top sonic anemometer ($z = 25.69$ m). From these diagrams, the T' distributions were less skewed after high-pass filtering.

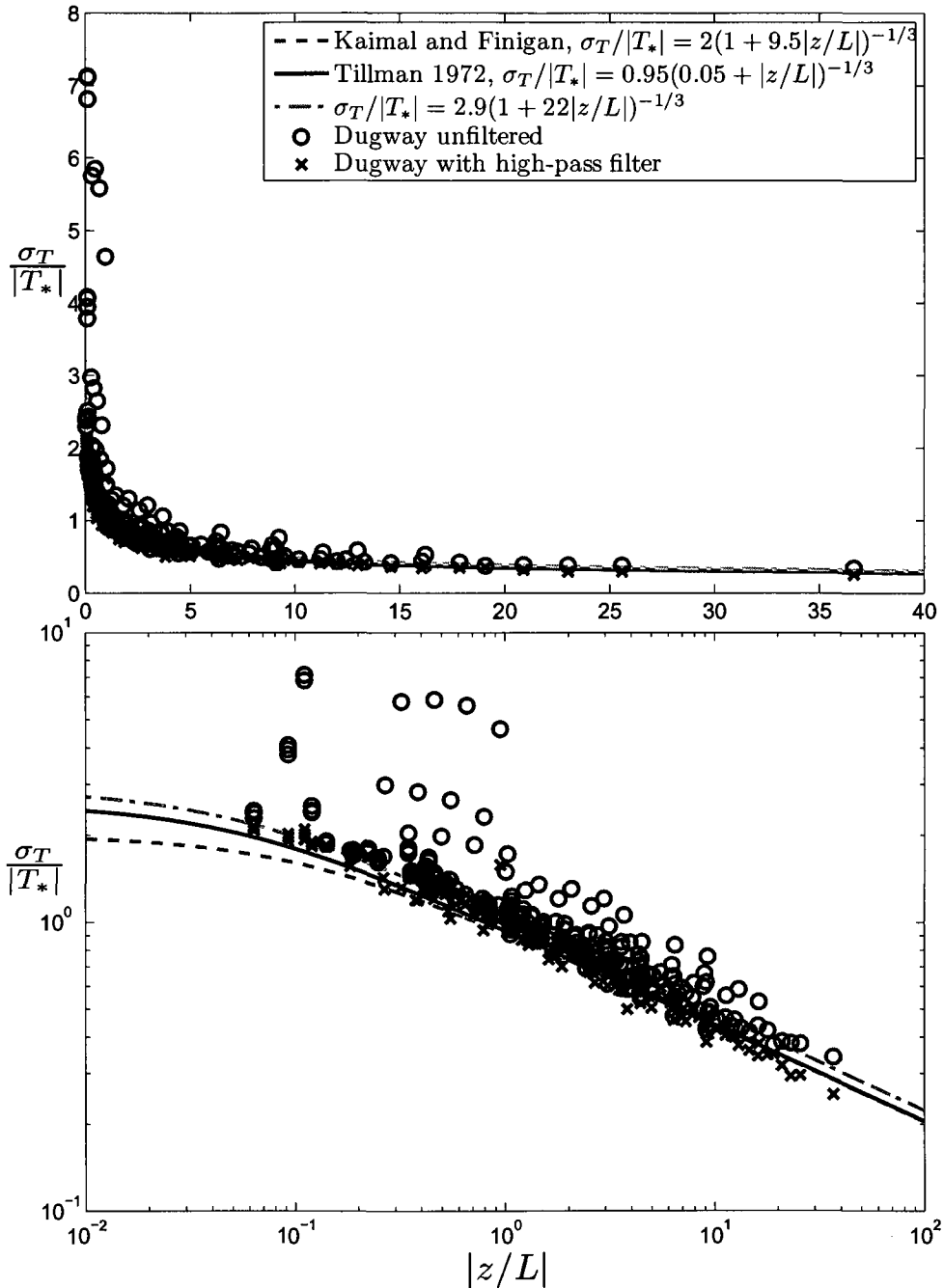


Figure 5.4: Dugway's 1hr values of $\sigma_T/|T_*|$ with and without high-pass filter. The one with high-pass filter is best fit with $\sigma_T/|T_*| = 2.9(1 + 22|z/L|)^{-1/3}$, which approaches the neutral limit at 2.9 and varies with $|z/L|^{-1/3}$ at $|z/L| \gtrsim 0.8$. Between the earlier results by Kaimal and Finnigan (1994) and Tillman (1972), Dugway's result is closer to the latter one. (Selection criterion: $L < 0$ m, $|\bar{\theta}_8| < 30^\circ$ and $u_* > 0.1 \text{ ms}^{-1}$.)

Chapter 6

Streamwise velocity spectra and boundary layer depth

The longitudinal or streamwise (u') velocity spectra in this chapter were calculated by the methods described in Chapter 3. In order to compare the computed Dugway spectra with pre-existing empirical spectral curves that summarize the spectra of prior experiments, the value of the boundary layer depth (δ) is needed. Since the Dugway experiment did not measure this quantity directly, an estimate of (δ) had to be made. One approach is based on the heat budget. Alternatively, δ can be deduced by reference to the location the spectral peak of the u' spectrum. Once δ has been estimated, one may compare the computed (measured) spectra with the empirical curves of Kaimal et al. (1976).

6.1 Streamwise velocity spectra at Dugway

As described in Chapter 3, the spectral calculation is based on the FFT method, for which the number of samples in the time series should be a power of 2. Each time series of one hour Dugway data consists of 72000 points. The closest power of 2 to this number is $2^{16} = 65536$. Therefore, in each 1 hr run, only the first 65536

points (equal to 54.61 minutes) of u velocity time series will be used (the time series is truncated).

As real atmospheric data, the Dugway velocity spectra can be expected to be very noisy. The ‘raw’ spectrum was calculated by computing the periodogram after first applying a 2^{16} -point Hamming window to the original time series. The spectral range of the computed raw spectrum is $0.0003 \leq f \leq 10$ Hz. An example of the raw spectrum is given in the upper panel of Fig. 6.1. It was taken from the run on May 25, 2005 14:47 MDT (mid period time) of the sonic anemometer no.9 ($z = 25.69$ m). The atmosphere was very unstable ($L = -1.12$ m). The raw spectrum is very noisy and clearly affected by aliasing at the high frequency end.

To obtain a better spectral estimate, I followed the example of the analysis of the Kansas experiment, wherein the u' spectra were independently calculated (using FFT technique) over low and high frequency regions (Kaimal et al. 1972). For the low frequency region, a new “block average time series” was created by applying a 16-point block average to the original time series (non-overlapping blocks). I then calculated the periodogram after first applying a 4096-point Hamming window to this new time series. This spectrum for the low frequency region will be named the “block average spectrum.” Since the block average time series has lower sampling frequency than the original one, its Nyquist frequency (upper limit) is lower. Hence, it is equivalent to the spectrum of a low-pass filtered record. The example of a block average spectrum from the same run as above, is shown in the lower panel of Fig. 6.1 (labeled “block av”). This spectrum covers spectral range $0.0003 \leq f \leq 0.625$ Hz. It is not much less noisy than the raw spectrum, but the aliasing effect is gone.

The high-frequency spectral estimate is obtained by calculating Welch spectra. The original time series was divided into 16 non-overlapping consecutive blocks, where

each block contains 4096 points of data. I then calculated the periodogram for each block (after having first applied a 4096-point Hamming window) and averaged the 16 spectra together to get what will be named the “composite spectrum.” The principle or conjecture behind this approach is that the sixteen blocks should offer sixteen different and independent samplings of the high frequency behavior of the atmosphere. Since each block is much shorter than the original time series, its lowest frequency is higher than that of the raw spectrum. This is equivalent to the high-pass filter. An example of the composite spectrum is shown in the lower panel of Fig. 6.1 (labeled “composite”). It decreases with $f^{-2/3}$ (dashed lines are $-2/3$ reference lines) at the high frequency end. Even if it is much smoother than the raw spectrum, it remains noisy and is affected by aliasing at the high frequency end. The range of the composite spectrum is $0.005 \leq f \leq 10$ Hz.

The low- and high-frequency spectral estimates, thus computed, overlap over two decades (0.005-0.625 Hz). The agreement between the two estimates is generally quite good, as described in (Kaimal et al. 1972). The variances, recovered from the areas under each plot, are very close to the variance of the original time series of post-rotation u velocity. In Kansas spectra, the composite spectrum was treated as the basic spectrum, while the block average spectrum was computed in order to extend to the lower frequency region. In my analysis, the composite spectrum was used for calculating the TKE dissipation rate ϵ , as well as for comparing with the theoretical spectrum. The block average spectrum was used for extracting the boundary layer depth for the cases with unstable stratification.

The discussion above will have made it clear that even with one hour data records, computed spectra are noisy — which is a well-known problem. The averaging together of spectra deduced from records that had been measured under an invariant (or

similar) condition as regards governing (“external”) variables (such as, in our case, z, L, δ, u_*) is a legitimate way to improve the spectral estimate. Accordingly spectra from the sonic anemometers on the transect (nos. 10-13), since they all “see” the same atmospheric condition, may be averaged together to represent the spectrum at 3 m above ground.

Another technique to smooth the spectrum is to average the raw spectrum in bins of constant width in log-frequency space. For example, the raw spectrum from the above Dugway run was averaged in 50 equal logarithmic bins to get the “log average spectrum.” This spectrum is much smoother than the other spectral estimates, and covers the entire available frequency range. However, there might be no data at all in some bins, especially in the low frequency region.

By comparing u' spectra from different heights but during the same run (Fig. 6.2 *upper*), one may note that spectral density decreases with increasing height at the high frequency end, and that the spectral slope (or roll-off) goes as $f^{-2/3}$ (dashed lines are $-2/3$ reference lines). However in the low frequency region, one sees barely any difference between the spectral curves for different heights. If these spectra are normalized by $u_*^2 \phi_\epsilon^{2/3}$ and plotted as function of normalized frequency (Fig.6.2 *lower*), all spectra in the high frequency region collapse into the same curve.

6.2 The boundary layer depth (δ)

In order to compare the Dugway spectra with the theoretical curves (Eq. 3.20 and 3.27), the boundary layer depth (δ) is needed as an input. Unfortunately, there was no direct measurement of this quantity in the Dugway experiment. However it can be estimated from the heat flux and the temperature trend ($\frac{\partial T}{\partial t}$), by adoption of

the following rather simplistic heat budget equation

$$\frac{\overline{\partial T}}{\partial t} = 1.2 \frac{\overline{w'T'}}{\delta}, \quad (6.1)$$

(this assumes the entrainment heat flux through the capping inversion equals minus 20% of the surface heat flux that is driving the boundary layer). To extract δ , $\overline{w'T'}$ and $\frac{\overline{\partial T}}{\partial t}$ were averaged over sonic anemometers nos. 6 -13, i.e. ‘grand averages’ were formed

$$\overline{\overline{w'T'}} = \frac{1}{8} \sum_{i=6}^{13} (\overline{w'T'})_i, \quad \overline{\frac{\partial T}{\partial t}} = \frac{1}{8} \sum_{i=6}^{13} \left(\frac{\partial T}{\partial t} \right)_i \quad (6.2)$$

Then,

$$\delta = 1.2 \overline{\overline{w'T'}} \left(\overline{\frac{\partial T}{\partial t}} \right)^{-1} \quad (6.3)$$

In my analysis, the temperature trend of each run was deduced from the slope of a straight line linearly fitted to the temperature time series. The boundary layer depth deduced by this procedure will be denoted as δ_{HF} .

Independently of this estimate, the boundary layer depth can also be deduced from the location of the spectral peak. Liu and Ohtaki (1997) assumed that u' spectra should resemble the theoretical curves of Højstrup (Eq. 3.27). Based on the location of the spectral peak (Eq. 3.28), the boundary layer depth is

$$\delta = 0.7947 \left(\frac{\bar{u}}{f} \right)_{peak} \quad (6.4)$$

Analogously with the Kaimal’s formula (Eq. 3.26) we have

$$\delta = 0.6469 \left(\frac{\bar{u}}{f} \right)_{peak} \quad (6.5)$$

The reader has seen, however, that computed spectra are ‘noisy.’ It was therefore impossible to precisely locate the peaks of the Dugway spectra. However instead of visually locating the spectral peak, a provisional estimate of the boundary layer

depth could be systematically varied until the difference between the theoretical and experimental curves was minimized. In my analysis, the experimental curve was represented by the block average low frequency spectrum. Although it was very noisy, it covers the spectral region most influenced by the depth of mixing (boundary layer depth), and is not affected by aliasing. The theoretical spectrum was represented by Kaimal's spectrum rather than Højstrup's (the two are almost identical in unstable conditions). Then in each run and for each sonic anemometer, the boundary layer depth was varied across the range $1 \leq \delta \leq 5000$ m to find a best match of Kaimal's spectrum with the experimental curves. I then averaged together the several independent estimates of boundary layer depth stemming from different sonic anemometers, to obtain the average boundary layer depth of each run. The boundary layer depth deduced in this manner by best fitting Kaimal's spectral curve will be denoted as δ_K .

Fig. 6.3 and Table 6.1 compare the two estimates δ_K and δ_{HF} of boundary-layer depth. Fig. 6.3 clearly shows the diurnal cycle. ABL depth starts to increase in the morning and reaches its maximum value in the late afternoon. Its values lie in a reasonable range (up to a few kilometers). In many cases δ_K and δ_{HF} agree quite well. In a few runs where δ_{HF} was unusually low, δ_K gave more reasonable values. Since there was no direct measurement of the boundary layer depth during the Dugway experiment, no comment can be offered on the relative accuracies of the two procedures.

6.3 Discussion

Appendix A collects the spectral curves from all the selected unstable runs. An example of these plots was shown on the left hand side of Fig. 6.4. In the high frequency region most of the observed Dugway u' spectra exhibit a spectral density

Table 6.1: The boundary layer depth deduced from heat fluxes and spectral peak.

MDT	δ_{HF} (m)	δ_K (m)
May 24,2005 08:46	398.9	469.3
May 24,2005 09:46	227.4	279.3
May 24,2005 10:46	852.4	343.9
May 24,2005 11:46	320.6	567.5
May 24,2005 12:46	542.2	479.0
May 24,2005 13:46	642.2	924.3
May 24,2005 14:46	1124.2	1033.8
May 24,2005 15:46	1002.7	807.3
May 24,2005 18:47	1294.9	1015.0
May 25,2005 11:47	743.6	424.5
May 25,2005 12:47	659.6	1308.9
May 25,2005 13:47	597.7	788.1
May 25,2005 14:47	691.2	1454.4
May 25,2005 15:47	906.8	1038.1
May 25,2005 16:47	1138.8	1682.3
May 25,2005 17:47	1498.2	1368.0
May 25,2005 18:47	1278.0	1142.5
May 26,2005 08:47	67.8	668.8
May 26,2005 09:47	441.1	261.5
May 26,2005 10:47	223.6	182.8
May 26,2005 12:47	382.1	698.3
May 26,2005 13:47	539.4	842.3
May 26,2005 14:47	807.5	1181.4
May 26,2005 15:47	756.8	1374.4
May 26,2005 16:47	789.2	1704.4
May 27,2005 08:47	19.2	117.0
May 27,2005 09:47	1008.9	222.4
May 27,2005 10:47	359.5	147.4
May 27,2005 12:47	353.4	439.4
May 27,2005 13:47	418.2	763.8
May 27,2005 14:47	349.8	1301.9
May 27,2005 16:47	556.0	1545.0
May 27,2005 17:47	818.3	2151.3
May 27,2005 18:47	1716.2	2117.0

that rolls off with $f^{-2/3}$, and decreases with increasing height. In the low frequency region the spectra are not well organized, and the peaks are not well defined.

Since the boundary layer depth only affects the spectral curve in the low frequency region, the Kaimal curves corresponding to different estimates of δ are identical in the high frequency region. Most of Dugway's u' spectra resemble the Kaimal empirical curve, especially in the high frequency region. Even at 3 m above ground, which is outside the range of the Minnesota experiment ($z \geq 4$ m), the spectra agree very well with the Kaimal's curves.

A few runs that clearly deviate from the empirical curves seem to have been associated with a particularly strong horizontal wind (9-10 m s⁻¹). The least unstable run is from May 24, 2005 8:46 MDT and has Obukov length $L = -48$ m. At 3 m above ground, for this run $|z/L| = 3/48$ which represents the nearest to neutral of all the selected data: and here the observed spectrum still agrees very well with Kaimal's curve. Once these spectra were normalized with $u_*^2 \phi_\epsilon^{2/3}$ and plotted versus normalized frequency, their high frequency regions approximately collapsed.

When spectra are plotted on a linear axis, agreement with the theoretical curves is less satisfactory (e.g. right hand side of Fig. 6.4), especially in the low frequency region – that is, use of log axes tends to hide the differences between the observed spectra and the empirical curves. However, in the inertial subrange, they still agree very well with the theoretical curve. Once they are normalized with $u_*^2 \phi_\epsilon^{2/3}$ in normalized frequency space, they collapse together as well.

In summary, the inertial subrange of the observed Dugway u' spectra is very consistent with the theoretical spectra. Their inertial subranges approximately collapse onto the same curve, once normalized with $u_*^2 \phi_\epsilon^{2/3}$. Since this spectral region obeys MOST theoretically, it can confirm that the observed Dugway u' spectra do obey Monin-Obukhov scaling.

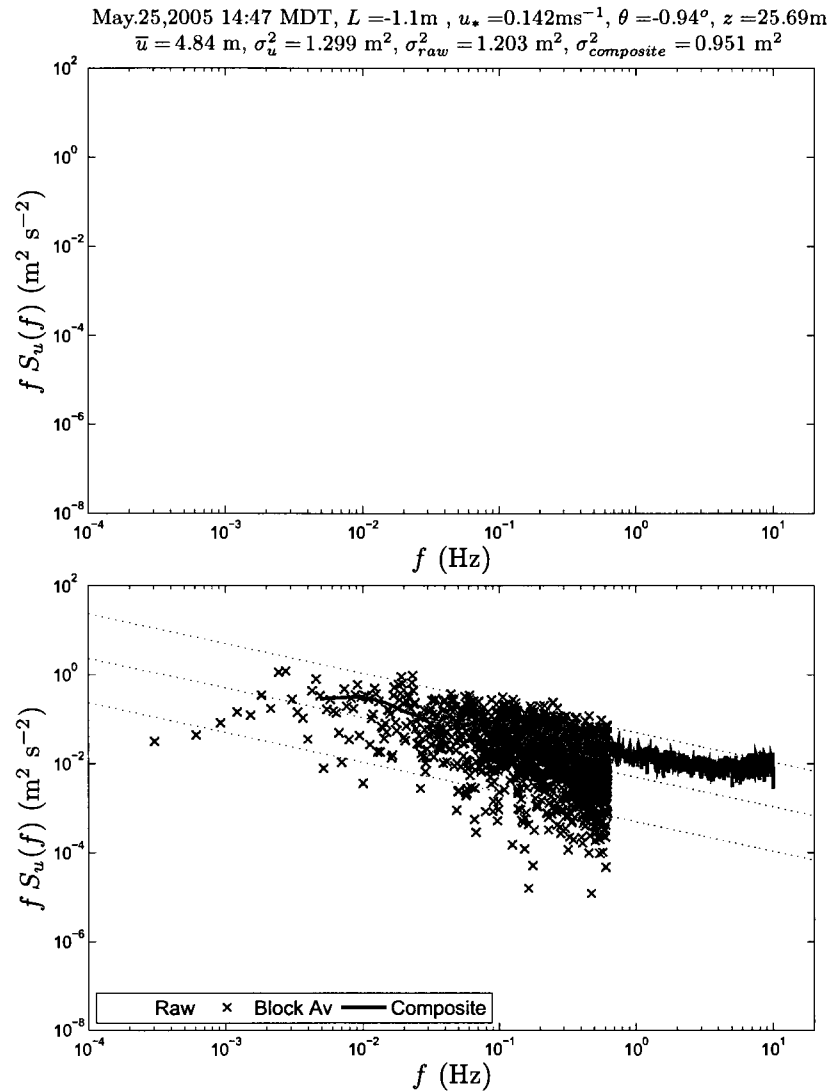


Figure 6.1: (*upper*) Dugway's raw u' spectrum ('raw') of May 25, 2005 14:47 MDT (mid period time) of the sonic anemometer no. 9 ($z = 25.69\text{ m}$). This spectrum is very noisy and spans $0.0003 \leq f \leq 10\text{ Hz}$. (*lower*) Block average ('block av') and composite ('composite') spectra for the same run. The block average spectrum was calculated from the block average time series, which was created by block averaging over 16 points of data (non-overlapping blocks). It is very noisy, spans $0.003 \leq f \leq 0.625\text{ Hz}$ (low-pass filter), and is not affected by aliasing. The composite spectrum spans $0.005 - 10\text{ Hz}$, the original time series being divided into 16 non-overlapping blocks or sub-series, each block containing 4096 points of data. The composite spectrum is the average of sixteen spectra of the sub-series. It is much smoother than the raw spectrum, but provides no information in the low frequency region (high-pass filter). These two spectra overlap over two decades ($0.005-0.625\text{ Hz}$) and agree quite well with each other in this region. The second line of the header indicates the variance of u velocity (measured) and the area under each curve, which represents the total variance. All of them are very close to each other as expected.

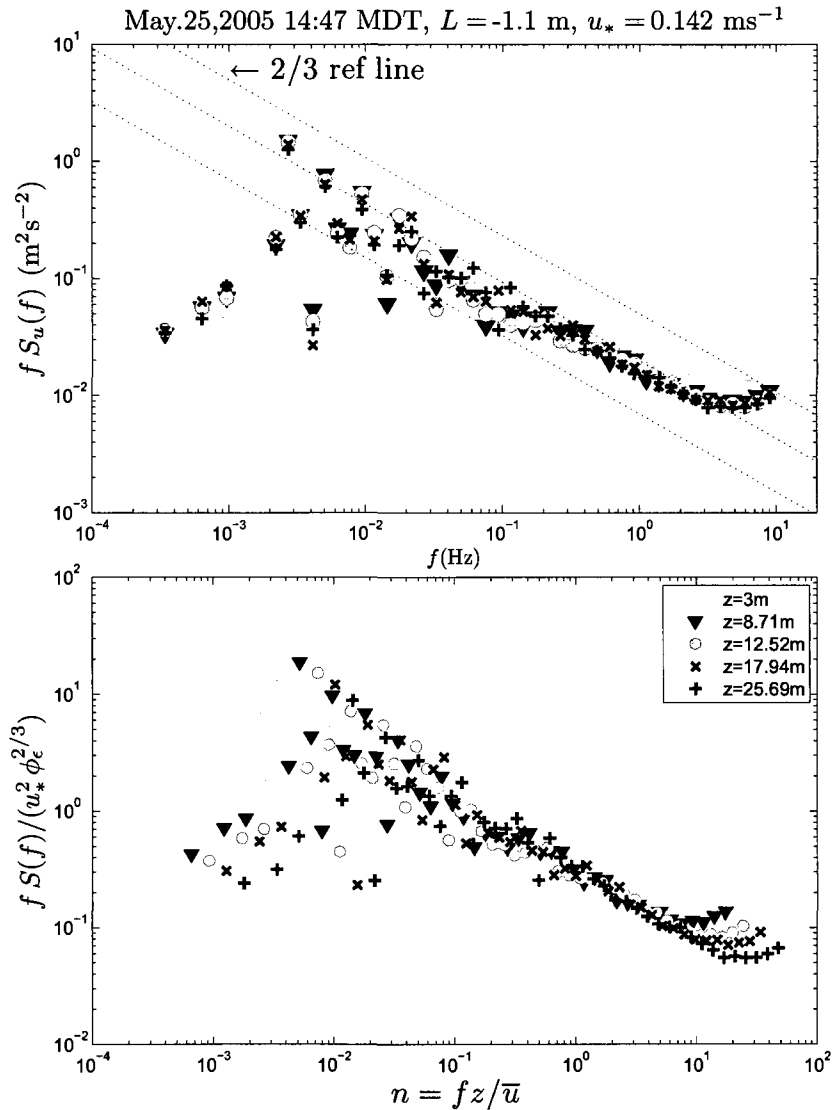


Figure 6.2: (*upper*) Comparison of Dugway u' spectra from different heights during the same run (May 25, 2005 14:47 MDT). In the high frequency region, spectral density decreases with increasing height and the spectral density “rolls off” with $f^{-2/3}$ (dashed lines are $-2/3$ reference lines). When these spectra were normalized with $u_*^2 \phi_\epsilon^{2/3}$ and plotted against normalized frequency (*lower*), the high frequency regions collapse into the same curve.

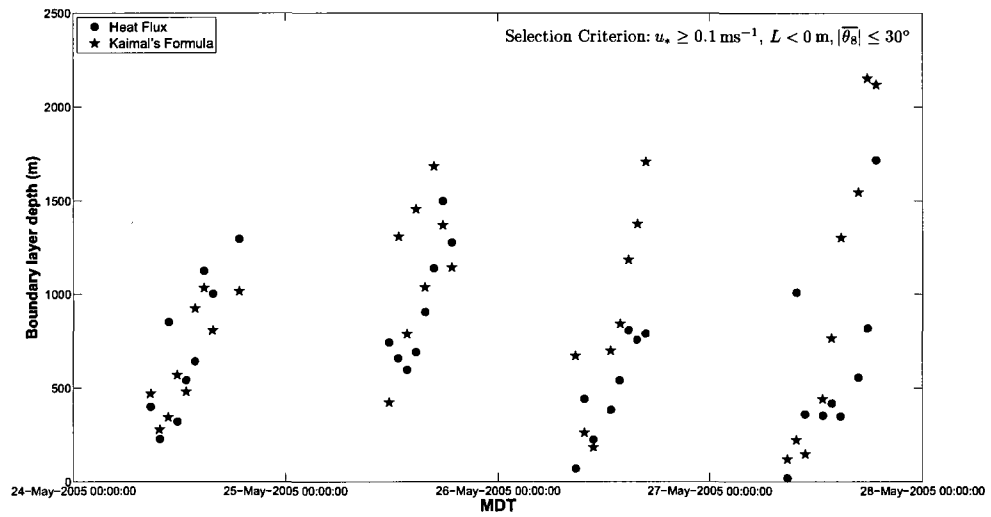


Figure 6.3: Evolution of the boundary layer depth with time, from selected unstable runs from Dugway experiment. The estimate based on the heat budget (δ_{HF} , labeled 'heat flux') and from Kaimal curve fitting (δ_K , labeled 'Kaimal's formula') tend to vary in the diurnal cycle in which ABL depth starts to increase in the morning and reaches its maximum daily value in the late afternoon. Overall, the two estimates agree quite well.

May.26,2005 13:47MDT, $L = -1.6$ m, $u_* = 0.148\text{ms}^{-1}$, $\delta_K = 842.3\text{m}$, $\delta_{HF} = 539.4\text{m}$

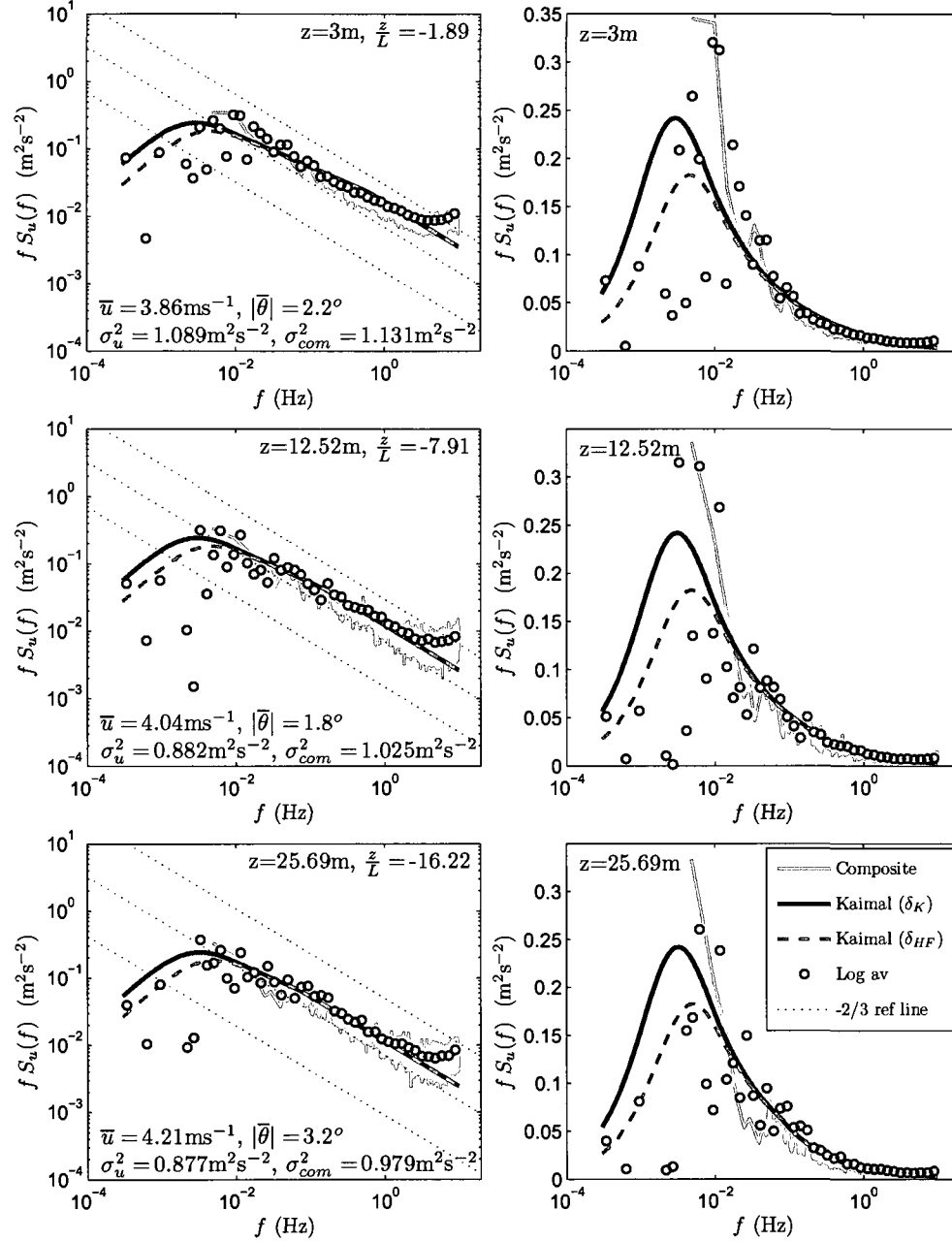


Figure 6.4: Examples of Dugway u' spectra. The left hand side was plotted in log-log axis, while the right hand side was in semilog axis. All of them contain the composite spectra ('composite'), δ_K Kaimal's theoretical curves ('Kaimal δ_K '), δ_{HF} Kaimal's theoretical curves ('Kaimal δ_{HF} ') and log average spectra ('log av'). The log-log axis plots also contains -2/3 reference lines for comparison in the inertial subrange region.

Chapter 7

TKE dissipation rate during unstable stratification

This chapter covers estimates of the TKE dissipation rate ϵ , deduced from the composite and log average spectra. These values will be compared with others' earlier results, and with estimates stemming from simplification of the TKE budget equation.

7.1 Methods for indirect estimation of TKE dissipation rate

The TKE dissipation rate can be indirectly estimated from velocity spectra by invoking Kolmogorov's law (Eq. 2.38) for the spectral density in the inertial subrange. Less familiarly, ϵ can be determined (Albertson et al. 1997, Chamecki and Dias 2004) from Kolmogorov's similarity laws for the statistical properties

$$D_2(r) \equiv \langle [u'(x) - u'(x+r)]^2 \rangle = S_2 \epsilon^{2/3} r^{2/3}, \quad (7.1)$$

$$D_3(r) \equiv \langle [u'(x) - u'(x+r)]^3 \rangle = -\frac{4}{5} \epsilon r, \quad (7.2)$$

where $D_2(r)$, $D_3(r)$ are the second- and third-order "structure functions," r being a small streamwise separation of two measurement points, and S_2 being a dimensionless constant. Albertson et al. (1997) favoured using the third order structure function to deduce ϵ , since Kolmogorov's prediction features no flexible constants.

Chamecki and Dias (2004), however, report that while values of ϵ deduced from Eq. 2.38 are very close to those deduced from Eq. 7.1, they are very different from those deduced from Eq. 7.2. They emphasize that the validity of Eq. 7.2 hinges on assumptions that probably are not valid in the vertically-inhomogeneous and strongly sheared ASL turbulence. Therefore according to Chamecki and Dias, estimation of ϵ from the inertial subrange of u' spectra is the preferable approach. Details of this procedure follow.

7.2 Experimental TKE dissipation rate

As stated in Chapter 2, the TKE dissipation rate can be extracted from measured spectral density in the inertial subrange of u' spectra, at the point where the normalized wave number is equal to unity (Eq. 2.41). Since the Dugway experiment yielded time- rather than spatial-series, I used Taylor's hypothesis to transform the Kolmogorov law (Eq. 2.38) into frequency space, viz.

$$f S_u(f) = \kappa F_u(\kappa) = \alpha_k \epsilon^{2/3} \left(\frac{2\pi f}{\bar{u}} \right)^{-2/3}. \quad (7.3)$$

Taking the logarithm on both sides of this equation, we have the equation of a straight line of slope $-2/3$ in $\log f$ axis, with the y -intercept at $\log B_1$,

$$\log f S_u(f) = -\frac{2}{3} \log f + \log B_1 \quad (7.4)$$

$$B_1 = \alpha_k \epsilon^{2/3} \left(\frac{2\pi}{\bar{u}} \right)^{-2/3}. \quad (7.5)$$

Then the TKE dissipation rate can be extracted from the y -intercept, $\log f = 0$ or $f = 1$ Hz, as

$$\epsilon = \frac{2\pi}{\bar{u}} \left[\frac{S_u(f=1)}{\alpha_k} \right]^{3/2}. \quad (7.6)$$

In order to find the y -intercept of any given Dugway u' spectrum, a line with $-2/3$ slope has been best fitted to the inertial subrange region. It was evident by inspection that most the Dugway u' spectra vary in proportion to $f^{-2/3}$ in the frequency range of 0.2 - 2 Hz. Beyond this range, they were effected by the aliasing effects. From a least square fitting with $-2/3$ slope, the y -intercept, B_2 is

$$B_2 = \bar{y} + \frac{2}{3} \bar{x}, \quad (7.7)$$

where

$$y_i = \log f_i S_u(f_i), \quad \bar{y} = \frac{1}{N} \sum_{i=1}^N \log f_i S_u(f_i) \quad (7.8)$$

$$x_i = \log f_i, \quad \bar{x} = \frac{1}{N} \sum_{i=1}^N \log f_i \quad (7.9)$$

Hence,

$$\log B_1 = B_2 \quad (7.10)$$

$$\alpha_k \epsilon^{2/3} \left(\frac{2\pi}{\bar{u}} \right)^{-2/3} = e^{B_2} \quad (7.11)$$

$$\epsilon = \frac{2\pi}{\bar{u}} \left(\frac{e^{B_2}}{\alpha_k} \right)^{3/2} \quad (7.12)$$

This procedure has been applied to the composite and log average spectra of the Dugway experiment. Results were compared with the following theoretical estimations.

7.3 Theoretical TKE dissipation rate

The TKE dissipation rate can be deduced theoretically from the TKE budget equation (Eq. 2.35). For the horizontally-homogeneous ASL in steady state condition — restrictions we assume do apply to the Dugway observations — this equation

simplifies to Eq. 2.36. Multiplying that equation by $k_v z / u_*^3$, one obtains

$$0 = -\frac{z}{L} - \frac{\overline{u'w'}}{u_*^3} \frac{k_v z}{\partial z} \frac{\partial \bar{u}}{\partial z} - \frac{k_v z}{u_*^3} \frac{\partial \overline{w'e}}{\partial z} - \frac{k_v z}{u_*^3} \frac{1}{\rho_0} \frac{\partial \overline{w'p'}}{\partial z} - \phi_\epsilon \quad (7.13)$$

The first term is buoyant production ($\phi_b = z/L$). The second is shear production, and may be simplified:

$$-\frac{\overline{u'w'}}{u_*^3} \frac{k_v z}{\partial z} \frac{\partial \bar{u}}{\partial z} \approx \frac{k_v z}{u_*} \frac{\partial \bar{u}}{\partial z} = \phi_m \quad (7.14)$$

The third term is turbulent transport

$$\phi_t = \frac{k_v z}{u_*^3} \frac{\partial \overline{w'e}}{\partial z} \quad (7.15)$$

while the fourth is pressure transport and the final term the (normalized) dissipation rate.

According to MOST, ϕ_m and ϕ_ϵ are universal functions of z/L . Turbulent transport (ϕ_t) can be determined directly from the experimental data. Pressure transport is difficult to measure, and often obtained from the imbalance of the remaining terms. Denoting that imbalance I , the normalized TKE budget equation of the ASL becomes

$$\phi_m - \frac{z}{L} - \phi_t - \phi_\epsilon + I = 0 \quad (7.16)$$

A common assumption is that the TKE budget is in “local equilibrium,” meaning that the normalized TKE dissipation rate can be approximated as a sum of the (normalized) shear and buoyant production terms, i.e.

$$\phi_\epsilon \approx \phi_m - \frac{z}{L} \quad (7.17)$$

Obviously (and as the terminology “local equilibrium” suggests) this is based on the assumption that ϕ_t and I are negligible. However measurements contradict that idea.

Wyngaard and Coté (1971) found from the Kansas experiment that

$$\phi_t = \begin{cases} -z/L, & z/L \leq 0 \\ 0, & z/L \geq 0 \end{cases} \quad (7.18)$$

The Dugway observations allow a comparative evaluation of ϕ_t . Eq. 7.15 can be rewritten as

$$\phi_t = \frac{\kappa_v z}{u_*^3} \frac{\partial \overline{w'e}}{\partial z} = \frac{\kappa_v(z/L)}{u_*^3} \frac{\partial \overline{w'e}}{\partial(z/L)} = \frac{\kappa_v}{u_*^3} \frac{\partial \overline{w'e}}{\partial \ln z} = \frac{\kappa_v}{u_*^3} \frac{\partial \overline{w'e}}{\partial \ln(z/L)} \quad (7.19)$$

Plotting $\overline{w'e}/u_*^3$ against z/L (Fig. 7.1), one finds that $\overline{w'e}/u_*^3$ depends linearly on z/L during unstable stratification. The equation of a straight line that best fits with this data is

$$y = -1.77x - 1.42, \quad (7.20)$$

which implies

$$\phi_t = \frac{\kappa_v(z/L)}{u_*^3} \frac{\partial \overline{w'e}}{\partial(z/L)} = -0.71 \frac{z}{L} \quad (7.21)$$

Although it differs from the result of Wyngaard and Coté (1971), this estimate from the Dugway data supports the idea of a linear dependency on z/L . Substituting this formula for ϕ_t back into Eq. 7.16 and further assuming the imbalance term is very small, the implied dependency of TKE dissipation rate on z/L for unstable stratification is

$$\phi_\epsilon \approx \phi_m - 0.29 \frac{z}{L} \quad (7.22)$$

Both Eq. 7.17 and Eq. 7.22 will be compared with the Dugway experimental results, in the next section.

7.4 Discussion

Normalized TKE dissipation rates for unstable stratification, deduced from composite and log average spectra of the Dugway experiment, were shown in Fig. 7.2.

Three theoretical curves have been plotted for comparison. Experimental values agreed best with the sum of shear and buoyant production (Eq. 7.17), rather than with Kaimal's Eq. 2.27. The curve defined by Eq. 7.22 is quite different from the experimental results, perhaps implying that the imbalance is not actually zero. The function ϕ_m for these calculations was evaluated using Eq. 2.24 (Dyer and Bradley 1982).

Other forms for ϕ_m have been suggested, most using a $-1/3$ or $-1/4$ power law for the unstable stratification, e.g.

$$\phi_m = (1 + 15|z/L|)^{-1/4} \quad (\text{Oncley et al. 1996}) \quad (7.23)$$

$$\phi_m = (1 + 19|z/L|)^{-1/4} \quad (\text{Dyer 1974, Högström 1996}) \quad (7.24)$$

$$\phi_m = (1 + 16|z/L|)^{-1/3} \quad (\text{Frenzen and Vogel 2001}) \quad (7.25)$$

These universal functions were compared together in Fig. 7.3. All are very similar and agree quite well with the experimental results.

Although ϕ_ϵ as computed here for the Dugway data does not exactly conform to earlier findings, it does clearly depend on z/L . This is another indication of the validity of Monin-Obukhov scaling.

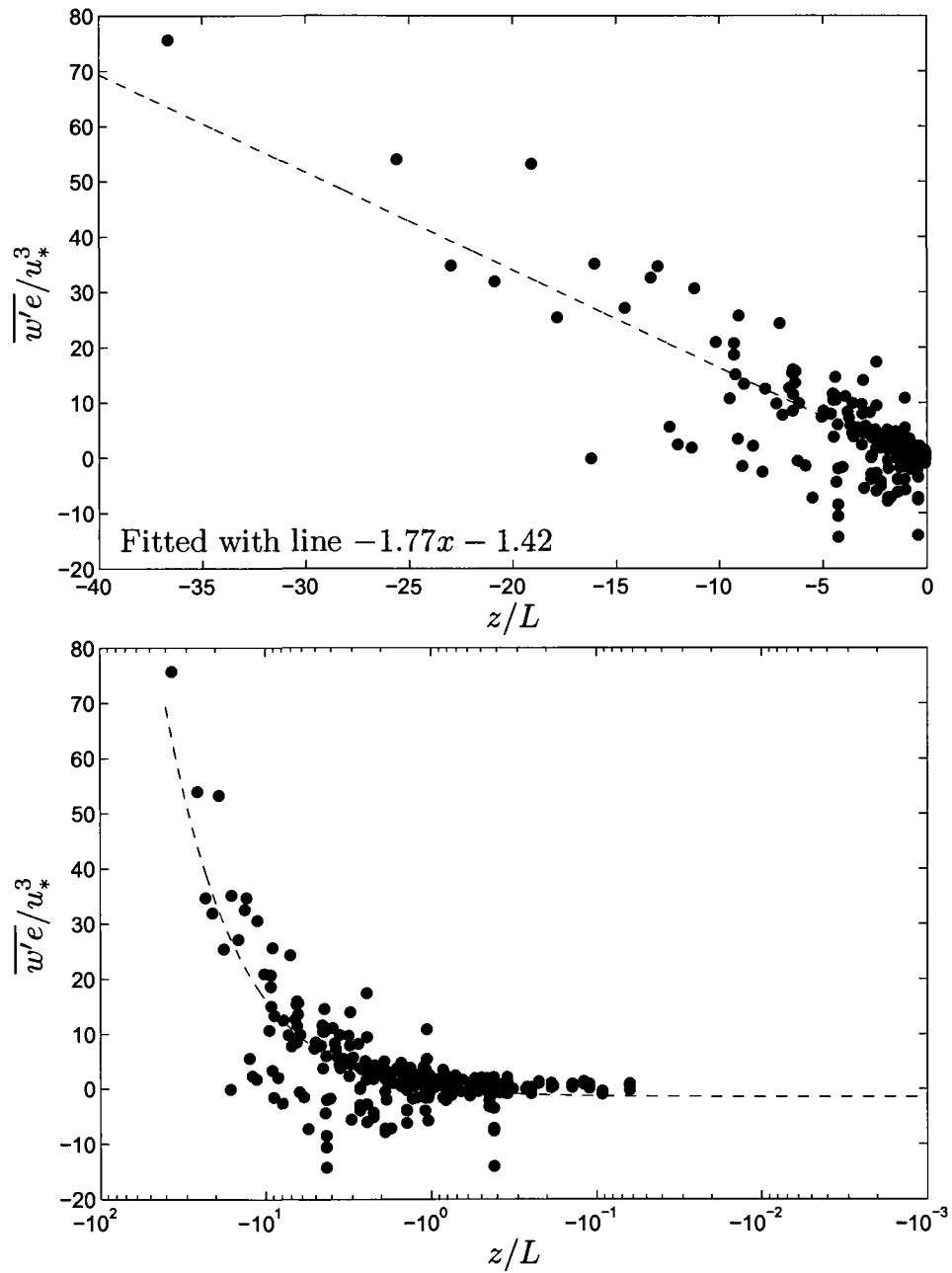


Figure 7.1: Dugway result for ϕ_t , from unstable runs. There is a clear dependency on z/L , which is best fitted by the straight line $y = -1.77x - 1.42$.

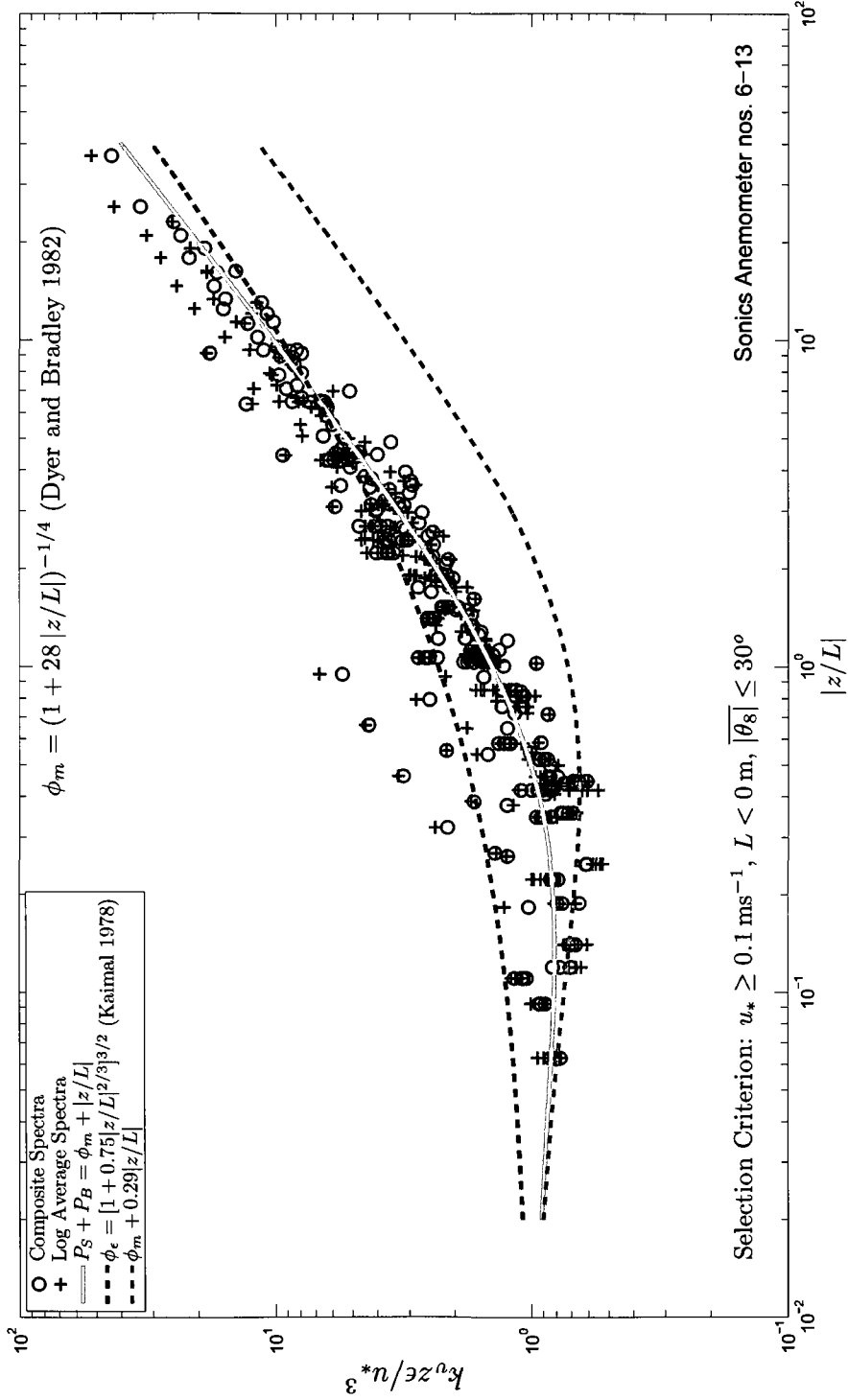


Figure 7.2: Dugway results for normalized TKE dissipation rate $k_v z \epsilon u_*^{-3}$ during unstable stratification. Observed values are best approximated by the sum of shear and buoyant production, rather than by the expression of ϕ_ϵ itself. The approximation in Eq. 7.22 ($\phi_\epsilon \approx \phi_m + 0.29 \frac{z}{L}$) is offset from the experimental results

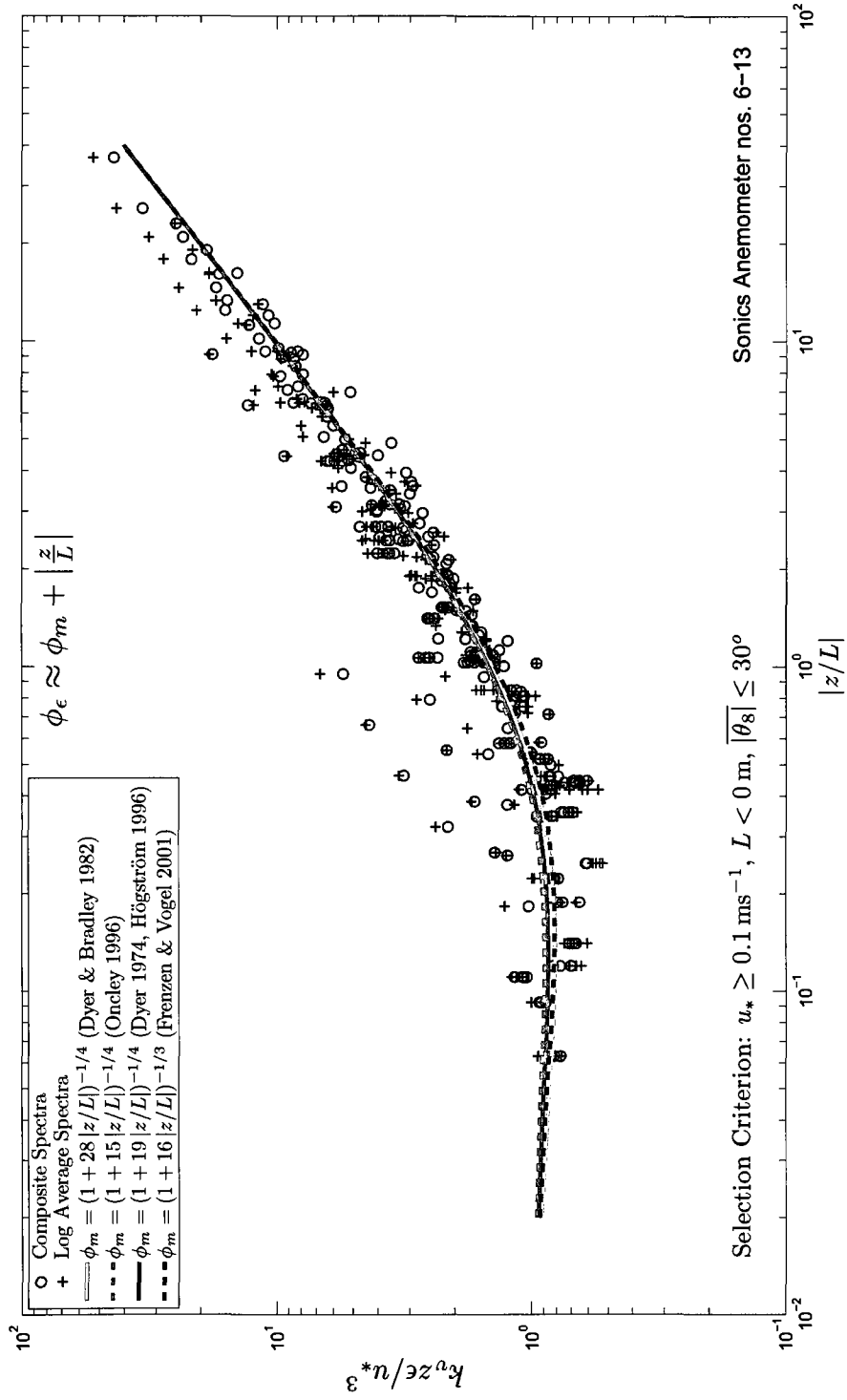


Figure 7.3: Dugway result for ϵ during unstable runs. Observed values are well approximated by the sum of shear and buoyant production ($\phi_\epsilon \approx \phi_m + |z/L|$). Different specifications of ϕ_m yield similar results.

Chapter 8

Dugway under stable stratification

In addition to the runs with unstable stratification, studied in the previous three chapters, the Dugway experiment offers for study some runs with stable stratification. In this chapter, the TKE dissipation rates for selected stable runs have been calculated and compared with the sum of shear and buoyant production, found in the previous chapter to be a good approximation of the TKE dissipation rate in unstable stratification.

8.1 Data selection

By definition Obukhov length is positive during stable stratification. Selection criteria were:

1. Stable stratification: $L > 0$ m
2. Avoid the transitions in stratification (twilight time), which (conservatively) span from 1 hr before and after sunrise and sunset (See Table 5.1).
3. Northerly wind: mean wind direction average over 8 sonic anemometers $|\bar{\theta}_8| \leq 30^\circ$. Since all the sonic anemometers were facing north, the optimized wind

direction that the sonic anemometers can record properly lie with in this range.

4. Wind not too weak: $u_* \geq 0.1 \text{ m s}^{-1}$. This is to make sure that the recorded data were larger than the instrumentation noise.
5. To avoid the flow disturbance caused by the berm and trailers, only the data from the sonic anemometers nos. 6-13, which are the top 4 sonics anemometer on the tower and the 4 sonic anemometers on the west side of the tower were considered
6. No NaN entries.

Fourteen runs with stable stratification satisfied all criteria (Table 8.1).

Table 8.1: MOST parameters for runs selected by the criteria that $L > 0 \text{ m}$, $|\bar{\theta}_8| \leq 30^\circ$ and $u_* \geq 0.1 \text{ m s}^{-1}$. The date and time stated in this table is the mid-period time.

Date/Time (GMT)	Date/Time (MDT)	u_* (m s ⁻¹)	L (m)	T_* (K)
May 24,2005 05:46	May 23,2005 23:46	0.123	41.85	0.027
May 24,2005 06:46	May 24,2005 00:46	0.138	39.25	0.037
May 24,2005 07:46	May 24,2005 01:46	0.215	393.24	0.009
May 24,2005 09:46	May 24,2005 03:46	0.182	209.16	0.012
May 25,2005 05:47	May 24,2005 23:47	0.254	143.84	0.033
May 25,2005 06:47	May 25,2005 00:47	0.247	1687.85	0.003
May 25,2005 07:47	May 25,2005 01:47	0.249	12733.24	0.000
May 25,2005 09:47	May 25,2005 03:47	0.206	183.70	0.017
May 26,2005 06:47	May 26,2005 00:47	0.101	28.55	0.026
May 26,2005 07:47	May 26,2005 01:47	0.120	18.93	0.056
May 26,2005 08:47	May 26,2005 02:47	0.154	51.01	0.034
May 26,2005 09:47	May 26,2005 03:47	0.191	54.16	0.050
May 27,2005 04:47	May 26,2005 22:47	0.158	102.08	0.018
May 27,2005 09:47	May 27,2005 03:47	0.114	23.95	0.040

8.2 MOST statistics and universal functions for stable conditions

Since most of the data clustered over small z/L rather than being uniformly distributed, stable side ϕ_w , ϕ_T and ϕ_t do not show any clear trends (Fig. 8.1). Hence, I shall not attempt to compare these normalized functions with results from earlier experiments.

Regarding u' spectra in stable stratification, the spectral roll-off in the inertial subranges does vary with $f^{-2/3}$ (e.g. Fig. 8.2 and 8.3), hence the TKE dissipation rate can still be extracted. However, when normalized by $u_*^2 \phi_\epsilon^{2/3}$ and plotted in normalized frequency space, spectra from different heights do not always collapse together.

As for the nature of the TKE balance in stable stratification, it remains uncertain (Kaimal and Finnigan 1994). Wyngaard (1975) assumed that the transport terms (pressure, turbulent) are very small, i.e. that the TKE budget is (nearly) in a state of “local equilibrium” such that

$$\phi_\epsilon \approx \phi_m - \frac{z}{L}. \quad (8.1)$$

On Fig. 8.2 the present measurements of ϕ_ϵ are plotted along with three previous formulations, namely Eq. 2.26, and Eq. 8.1 evaluated with each of two different specifications of ϕ_m : the first being Eq. 2.25 (Businger et al. 1971, Högström 1988), and the second (Dyer 1974, Högström 1988)

$$\phi_m = 1 + 4.8 z/L, \quad 0 \leq z/L \leq 1. \quad (8.2)$$

Compared to the corresponding results from unstable periods of measurement, the normalized TKE dissipation rate under stable conditions is quite scattered. It is hard

to judge which reference curve provides best fit with the experimental data. However, it can at least be concluded that ϕ_ϵ does depend on z/L , as expected from MOST.

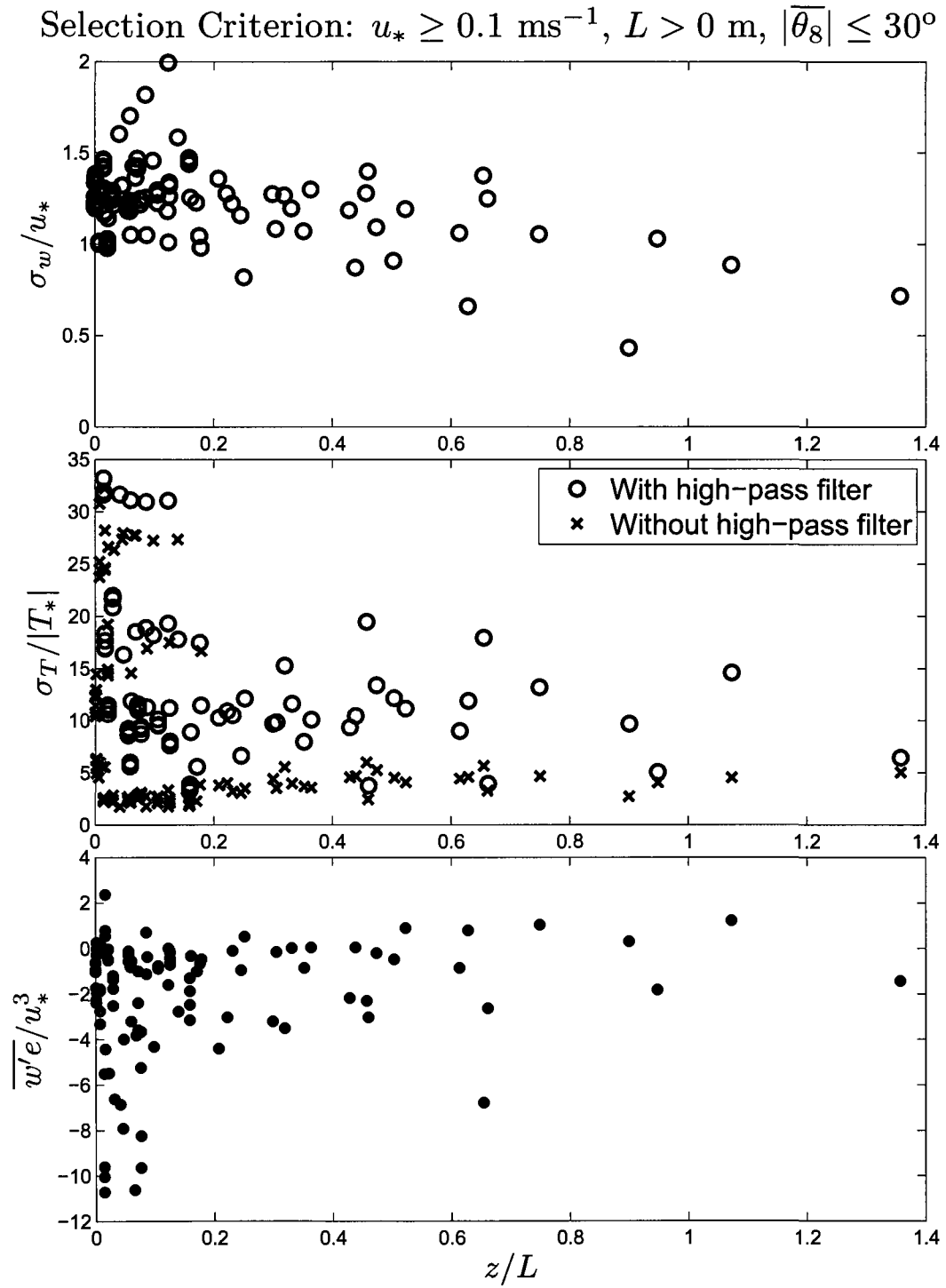


Figure 8.1: Dugway's normalized functions, ϕ_w , ϕ_T and ϕ_t , for stable runs. Most of them cluster around small z/L and do not explicitly show any trend.

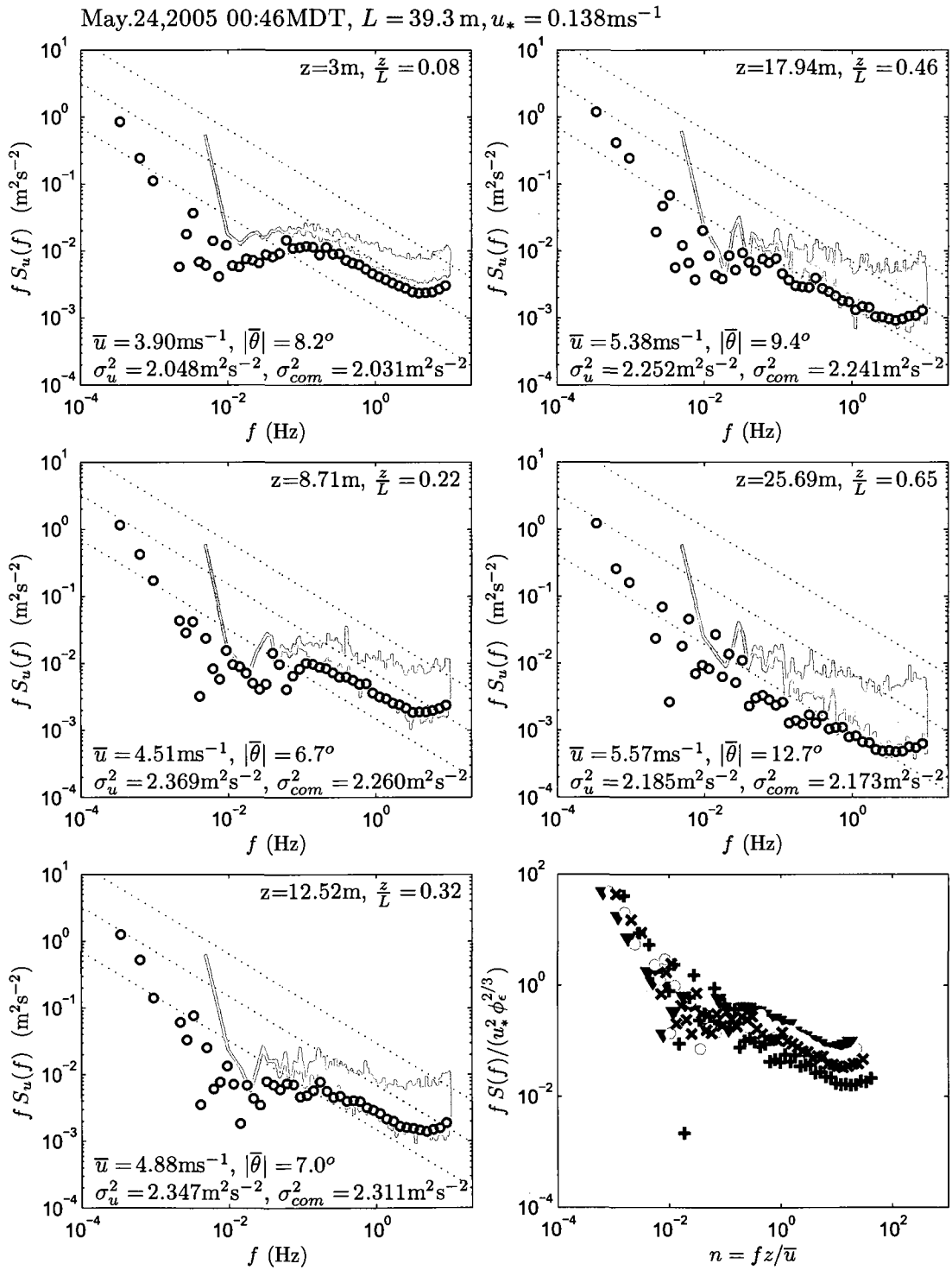


Figure 8.2: Example 1 of u' Spectra Under Stable Condition (See descriptions in Fig. A.1 and A.2).

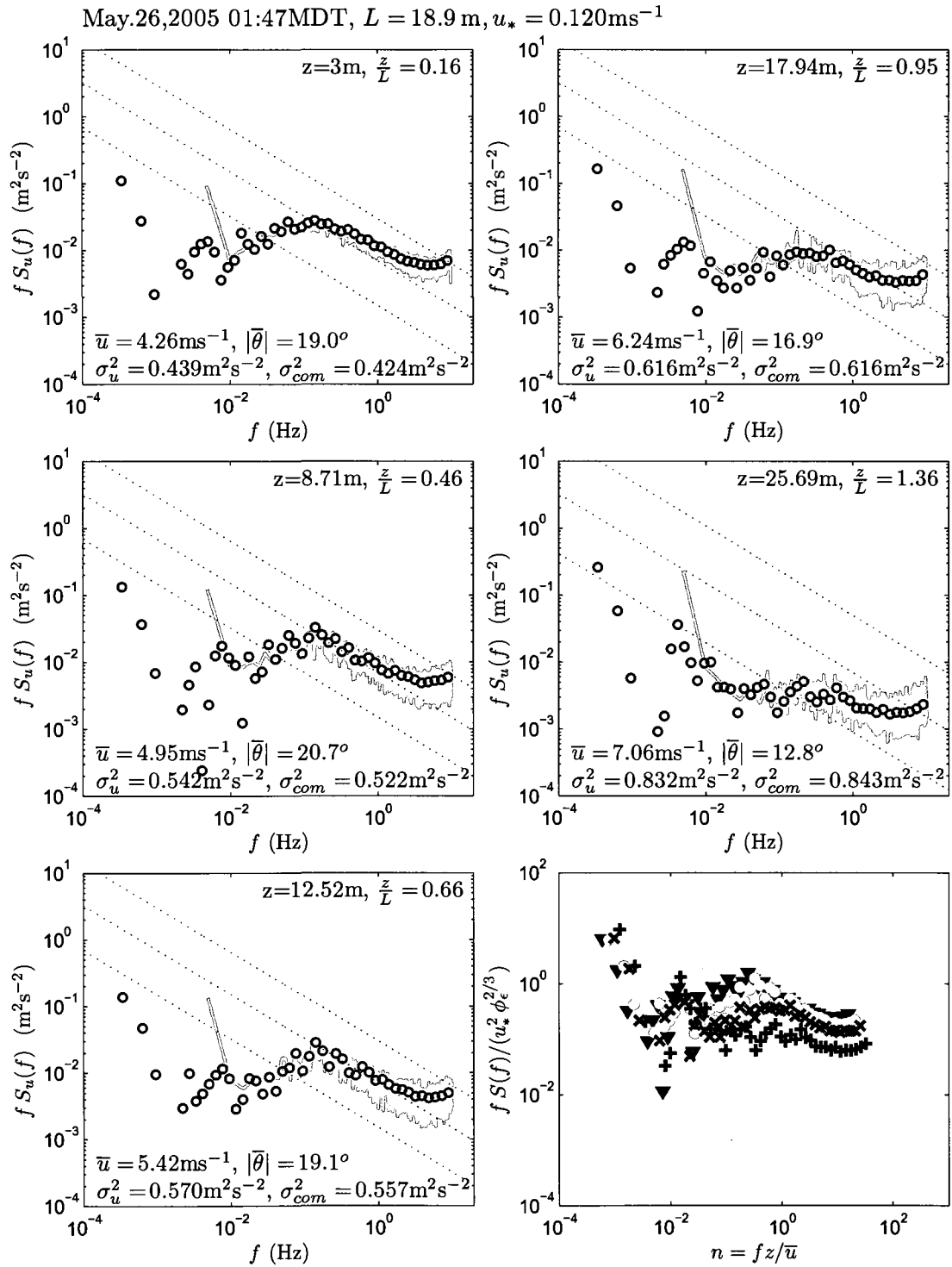


Figure 8.3: Example 2 of u' Spectra Under Stable Condition (See descriptions in Fig. A.1 and A.2).

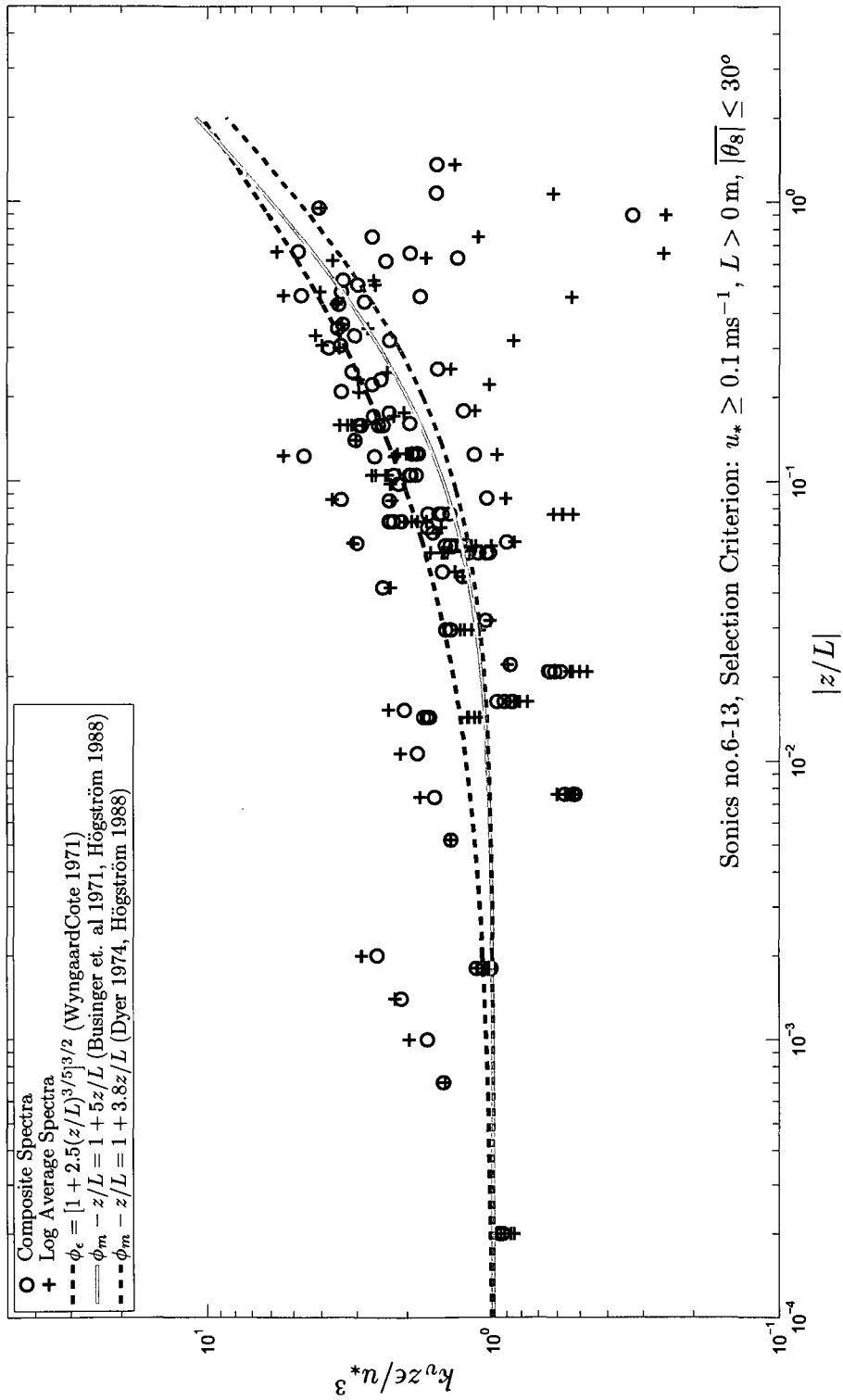


Figure 8.4: Dugway's ϕ_e for stable runs are quite scattered compare to the result under unstable condition.

Chapter 9

McNaughton’s scaling theory for unstable stratification

As stated in Chapter 2, (McNaughton 2006, McNaughton et al. 2007) have suggested a revised scaling theory for the ASL, which is intended to better account for the interaction between the surface layer and the outer layer. McNaughton’s scheme requires as one input the TKE dissipation rate (“ ϵ_0 ”) from the *outer* layer, wherein it is assumed to be height invariant. Under sufficiently unstable stratification, the uppermost sonic anemometer of the Dugway tower lay within the outer layer, so that its TKE dissipation rate (“ ϵ_9 ”) represents ϵ_0 in McNaughton’s scaling theory. The McNaughton length scale (Eq. 2.48) becomes

$$z_s = \frac{u_*^3}{k_v \epsilon_9}. \quad (9.1)$$

Under the McNaughton scaling the normalized standard deviations of w and T

$$\frac{\sigma_w}{u_\epsilon} \quad \text{and} \quad \frac{\sigma_T}{|T_\epsilon|} \quad (9.2)$$

are expected to organize against (vary with) z/z_s , rather than z/L .

9.1 Comparison between MOST and McNaughton's scaling theory

The extremely unstable runs, for which $|L| < 2.5$ m are selected from Table 5.2. There are 7 extremely unstable runs in total (Table 9.2). Each run has undergone the same procedure as described in Chapters 4-6 to get the MOST parameters, and to compute σ_w and σ_T , as well as to extract ϵ from u' spectra. Since u_ϵ is an individual value for each sonic anemometer rather than an average value over the transect, it is suggested that MOST parameters from individual sonic anemometers should be calculated for comparison as well. These individual MOST parameters will be denoted by a subscript i . The equivalent MOST and McNaughton parameters are summarized in Table 9.1.

Table 9.1: Comparison between MOST and McNaughton scaling parameters

MOST	L	u_*	T_*	z/L	$\frac{\sigma_w}{u_*}, \frac{\sigma_w}{u_{*i}}$	$\frac{\sigma_T}{ T_* }, \frac{\sigma_T}{ T_{*i} }$
McNaughton	z_s	u_ϵ	T_ϵ	z/z_s	$\frac{\sigma_w}{u_\epsilon}$	$\frac{\sigma_T}{ T_\epsilon }$

A comparison of MOST and McNaughton scaling is given in Fig. 9.1. The upper panel shows normalized σ_w vs z/L and z/z_s . Both σ_w/u_* and σ_w/u_{*i} vary tidily with z/L , as does σ_w/u_ϵ with z/z_s except at small values of the latter. The lower panel

Table 9.2: Selected runs with extremely unstable conditions from Table 5.2 by limiting $|L| < 2.5$ m.

Date/Time (MDT)	u_* (m s ⁻¹)	L (m)	z_s (m)
May 25,2005 14:47	0.142	-1.12	1.029
May 25,2005 16:47	0.147	-1.35	1.358
May 25,2005 17:47	0.167	-2.14	2.373
May 26,2005 12:47	0.156	-1.98	2.259
May 26,2005 13:47	0.148	-1.58	1.792
May 26,2005 15:47	0.112	-0.70	0.590
May 27,2005 16:47	0.115	-1.23	1.096

shows normalized σ_T vs z/L and z/z_s . Dependence of $\sigma_T/|T_*|$ and $\sigma_T/|T_{*i}|$ on z/L is tidier than the dependence of $\sigma_T/|T_\epsilon|$ on z/z_s . Thus although McNaughton scaling does a good job of normalizing σ_w , it is less successful in scaling σ_T . Apparently MOST offers better scaling for the ASL.

Selection criterion: $-2.5 \text{ m} < L < 0 \text{ m}$, $u_* \geq 0.1 \text{ ms}^{-1}$, $|\overline{\theta}_8| \leq 30^\circ$

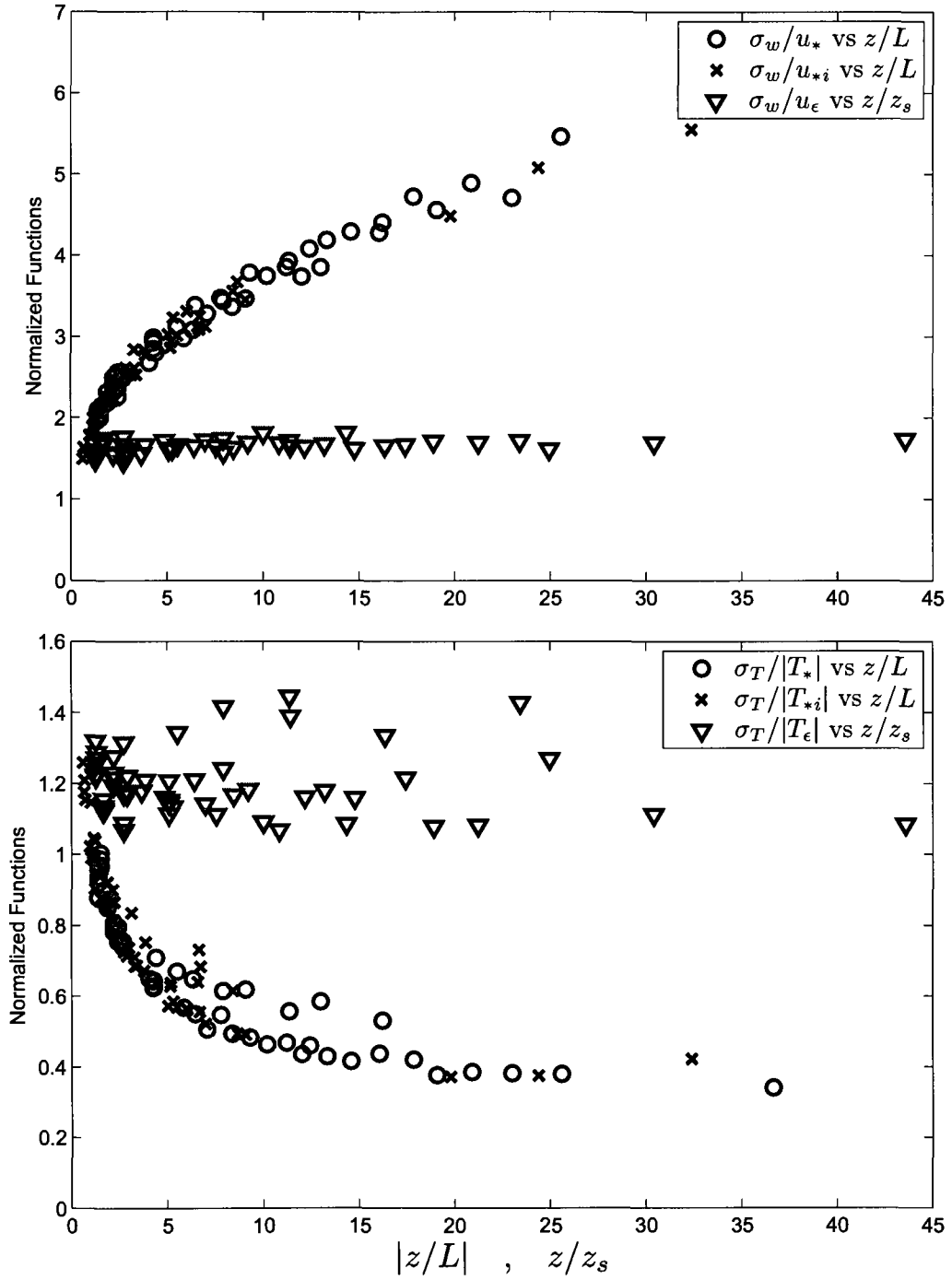


Figure 9.1: (upper) σ_w/u_* and σ_w/u_{*i} vary tidily with z/L , as does σ_w/u_ϵ with z/z_s . (lower) $\sigma_T/|T_*|$ and $\sigma_T/|T_{*i}|$ vary tidily with z/L , however even if $\sigma_T/|T_\epsilon|$ depends on z/z_s its trend is not clearly defined.

Chapter 10

Conclusions

The ASL experiment I have analysed here, an experiment which was performed over a desert flat in Dugway, Utah in May 2005, has provided very useful data. Under suitable selection criteria there were thirty-four unstable runs ($L < 0$ m) of which seven were extremely unstable ($-2.5 \text{ m} < L < 0 \text{ m}$), and fourteen stable runs ($L > 0$ m), where each run lasts for around 1 hr. The present study of velocity and temperature statistics under unstable conditions reveals that:

- σ_w/u_* is a well-organized function of z/L . The function $\phi_w(z/L) = \sigma_w/u_*$ found here has a shape similar to that reported from earlier experiments, and is best fitted by

$$\frac{\sigma_w}{u_*} = 0.96 (1 + 5.8 |z/L|)^{1/3}. \quad (10.1)$$

The neutral limit of about 0.96 differs from the standard 1.3 (Panofsky et al. 1977), but is very close to several later reports (Wilson 2008, Högström 1990, Moraes 2000) whose neutral limits were closer to unity.

- $\sigma_T/|T_*|$ is a function z/L . Scatter is reduced by high-pass filtering the temperature time series with a 72 second moving average. After the high-pass filter

has been applied, this temperature statistic $\phi_T = \sigma_T/|T_*|$ is best fitted by

$$\phi_T = 2.9 (1 + 22 |z/L|)^{-1/3} \quad (10.2)$$

The neutral limit of 2.9 is very close to the 2.6 obtained by Tillman (1972).

- The spectral calculation was based on the Fast Fourier Transforms method. It turns out that u' spectra always resemble the empirical curves of Kaimal's formula. The spectral slope or roll-off in the inertial subrange does vary with $f^{-2/3}$, as predicted by Komolgorov's law. Other than with increasing frequency, the u' spectral densities also vary with height. As height increases, the u' spectral density in the inertial subrange decreases. The u' spectra can be scaled by $u_*^2 \phi_\epsilon^{2/3}$ and plotted against normalized frequency, which causes the inertial subrange from different heights to collapse onto the same curve. Furthermore, even outside the range of Minnesota experiment ($z \leq 4$ m), Dugway u' spectra at 3 m above ground still agree very well with Kaimal spectral curves.
- The boundary layer depth can also be obtained by fitting the Kaimal spectral curve to the Dugway u' spectrum in the low frequency region. The results from this method are broadly compatible with estimates deduced from the heat budget, clearly revealing the diurnal variation, and lying in a reasonable range.
- The TKE dissipation rate (ϵ) can be extracted from u' spectra by fitting a straight line with $-2/3$ slope in the inertial subrange region. The normalized TKE dissipation rate (ϕ_ϵ) is a function of z/L and best approximated by the sum of shear and buoyant production, rather than by an earlier-provided expression for ϕ_ϵ itself.

From the above results, evidently MOST is a useful scaling theory for the unstable ASL observed at Dugway.

For the runs under stable stratification, the data only clustered over a small range in z/L and did not suggest any clear trend. Inertial subranges of the u' spectra still obeyed Kolmogorov's law. Therefore, the extraction of the TKE dissipation rate is still possible in this region. Although ϕ_ϵ in stable stratification is quite scattered, it does show dependence on z/L . It can be fitted either by the sum of shear and buoyant production or by an expression for ϕ_ϵ provided earlier.

The very unstable runs provided an indication of the performance of the new scaling theory (McNaughton 2006, McNaughton et al. 2007). This needs the TKE dissipation rate from the outer layer (ϵ_0) as an input for the length scale (z_s) and velocity scale (u_ϵ). Under extremely unstable conditions, the top sonic anemometer would be in the outer layer. Thus, its TKE dissipation rate can represent the outer layer's. Once normalized with these scaling parameters, the standard deviation in w shows the dependence of σ_w/u_ϵ on z/z_s . However for the temperature statistics, MOST does a lot better than McNaughton's scaling: $\sigma_T/|T_\epsilon|$ seems to depend on z/z_s , but does not show any trend clearly.

In conclusion, Monin-Obukhov similarity theory organizes observations from the unstable atmospheric surface layer very well. For stable stratification, the results are not as good as the unstable ones, due at least in part to the small range of z/L . For an extremely unstable condition, MOST does a better job than McNaughton's scaling theory. For now, MOST remains the preferred scaling theory for the ASL.

Bibliography

- Albertson, J. D., Parlange, M. B., Kiely, G. and Eichinger, W. E.: 1997, The average dissipation rate of turbulent kinetic energy in the neutral and unstable atmospheric surface layer, *Journal of Geophysical Research* **102**, 13423–13432.
- Arya, S. P.: 1988, *Introduction to micrometeorology*, Academic Press.
- Broersen, P. M. T.: 2006, *Automatic autocorrelation and spectral analysis*, Springer-Verlag.
- Buckingham, E.: 1914, On physically similar systems: illustrations of the use of dimensional analysis, *Physical Review* **4**, 345–376.
- Businger, J. A. and Yaglom, A. M.: 1971, Introduction to Obukhov's paper on turbulence in an atmosphere with a non-uniform temperature, *Boundary-Layer Meteorology* **2**, 3–6.
- Businger, J., Wyngaard, J., Izumi, Y. and Bradley, E.: 1971, Flux-profile relationships in the atmospheric surface layer, *Journal of the Atmospheric Sciences* **28**, 181–189.
- Chamecki, M. and Dias, N. L.: 2004, The local isotropy hypothesis and the turbulent

- kinetic energy dissipation rate in the atmospheric surface layer, *Quarterly Journal of the Royal Meteorological Society* **130**, 2733–2752.
- Dyer, A. J.: 1974, A review of flux-profile relationships, *Boundary-Layer Meteorology* **7**, 363–372.
- Dyer, A. J. and Bradley, E. F.: 1982, An alternative analysis of flux-gradient relationships at the 1976 ITCE, *Boundary-Layer Meteorology* **22**, 3–19.
- Finch, S.: 2004, Ornstein-Uhlenbeck Process, Online.
URL: <http://algo.inria.fr/csolve/ou.pdf>
- Foken, T.: 2006, 50 years of the Monin-Obukhov similarity theory, *Boundary-Layer Meteorology* **119**, 431–447.
- Frenzen, P. and Vogel, C. A.: 2001, Further studies of atmospheric turbulence in layers near the surface: scaling the TKE budget above the roughness sublayer, *Boundary-Layer Meteorology* **99**, 173–206.
- Högström, U.: 1988, Non-dimensional wind and temperature profiles in the atmospheric surface layer: A re-evaluation, *Boundary-Layer Meteorology* **42**, 55–78.
- Högström, U.: 1990, Analysis of turbulence structure in the surface layer with a modified similarity formulation for near neutral conditions, *Journal of the Atmospheric Sciences* **47**, 1949–1972.
- Högström, U.: 1996, Review of some basic characteristics of the atmospheric surface layer, *Boundary-Layer Meteorology* **78**, 215–246.
- Højstrup, J.: 1982, Velocity spectra in the unstable planetary boundary layer, *Journal of the Atmospheric Sciences* **39**, 2239–2248.

- Kaimal, J. C.: 1978, Horizontal velocity spectra in an unstable surface layer, *Journal of the Atmospheric Sciences* **35**, 18–24.
- Kaimal, J. C. and Finnigan, J. J.: 1994, *Atmospheric boundary layer flows: their structure and measurement*, Oxford University Press.
- Kaimal, J. C. and Wyngaard, J. C.: 1990, The Kansas and Minnesota experiments, *Boundary-Layer Meteorology* **50**, 31–47.
- Kaimal, J. C., Wyngaard, J. C., Haugen, D. A., Cote, O. R. and Izumi, Y.: 1976, Turbulence structure in the convective boundary layer, *Journal of the Atmospheric Sciences* **33**, 2152–2169.
- Kaimal, J. C., Wyngaard, J. C., Izumi, Y. and Cote, O. R.: 1972, Spectral characteristics of surface-layer turbulence, *Quarterly Journal of the Royal Meteorological Society* **98**(417), 563–589.
- Liu, X. and Ohtaki, E.: 1997, An independent method to determine the height of the mixed layer, *Boundary-Layer Meteorology* **85**, 497–504.
- McNaughton, K. G.: 2006, On the kinetic energy budget of the unstable atmospheric surface layer, *Boundary-Layer Meteorology* **118**, 83–107.
- McNaughton, K. G., Clement, R. J. and Moncrieff, J. B.: 2007, Scaling properties of velocity and temperature spectra above the surface friction layer in a convective atmospheric boundary layer, *Nonlinear Processes in Geophysics* **14**(3), 257–271.
- Monji, N.: 1973, Budgets of turbulent energy and temperature variance in the transition zone from forced to free convection, *Journal of the Meteorological Society of Japan* **51**(2), 133–144.

- Moraes, O. L. L.: 2000, Turbulence characteristics in the surface boundary layer over the south american pampa, *Boundary-Layer Meteorology* **96**, 317–335.
- Nakamura, R. and Mahrt, L.: 2006, Vertically integrated sensible-heat budgets for stable nocturnal boundary layers, *Quarterly Journal of the Royal Meteorological Society* **132**, 383–403.
- Obukhov, A. M.: 1971, Turbulence in an atmosphere with a non-uniform temperature, *Boundary-Layer Meteorology* **2**, 7–29.
- Oncley, S. P., Friehe, C. A., Larue, J. C., Businger, J. A. and Itsweire, Eric C. and Chang, S. S.: 1996, Surface-layer fluxes, profiles, and turbulence measurements over uniform terrain under near-neutral conditions, *Journal of the Atmospheric Sciences* **53**, 1029–1044.
- Pahlow, M., Parlange, M. B. and Porté-Agel, F.: 2001, On MoninObukhov similarity In the stable atmospheric boundary layer, *Boundary-Layer Meteorology* **99**, 225–248.
- Panofsky, H. A., Tennekes, H., Lenschow, D. H. and Wyngaard, J. C.: 1977, The characteristics of turbulent velocity components in the surface layer under convective conditions, *Boundary-Layer Meteorology* **11**, 355–361.
- Priestley, M. B.: 1981, *Spectral analysis and time series*, Academic Press.
- Sreenivasan, K. R.: 1995, On the universality of the Kolmogorov constant, *Physics of Fluids* **7**, 2778–2784.
- Stoica, P. and Moses, R. L.: 1997, *Introduction to spectral analysis*, Prentice-Hall.

- Stull, R. B.: 1988, *An Introduction to boundary layer meteorology*, Kluwer Academic Publishers.
- Tillman, J. E.: 1972, The Indirect determination of stability, heat and momentum fluxes in the atmospheric boundary layer from simple scalar variables during dry unstable conditions JF *Journal of Applied Meteorology*, *Journal of Applied Meteorology* **11**, 783–792.
- Welch, P. D.: 1967, The use of Fast Fourier Transform for the estimation of power spectra: A method based on time averaging over short, modified Periodogram, *IEEE Transactions on Audio and Electroacoustics* **AU-15**, 70–73.
- Wilczak, J. M., Oncley, S. P. and Stage, S. A.: 2001, Sonic anemometer tilt correction algorithms, *Boundary-Layer Meteorology* **99**, 127–150.
- Wilson, J. D.: 2008, Monin-Obukhov functions for standard deviations of velocity, *Boundary-Layer Meteorology* **129**, 353–369.
- Wyngaard, J.: 1975, Modeling the planetary boundary layer Extension to the stable case, *Boundary-Layer Meteorology* **9**, 441–460.
- Wyngaard, J. and Coté, O. R.: 1971, The budgets of turbulent kinetic energy and temperature variance in the atmospheric surface layer, *Journal of the Atmospheric Sciences* **28**, 190–201.

Appendix A

Streamwise velocity spectra for all selected unstable runs

All the spectral curves of the runs selected in Chapter 5 are shown in this chapter. The figure on each page represents each specific run. The header of each figure provides the following information for each run:

1. The mid-period time of each run, in MDT.
2. The Obukhov length (L [m]).
3. Friction velocity (u_* [m s^{-1}])
4. The boundary layer depth deduced by fitting Kaimal's empirical spectral curve (δ_K [m]).
5. The boundary layer depth deduced from the heat budget (δ_{HF} [m])

Each figure contains 6 sub-figures. The first 5 sub-figures provide the following information from each sonic anemometer for each run. (Note that the spectral curves from sonic anemometers nos. 10-13 were average together to represent the spectrum at $z = 3$ m above ground.)

1. Composite spectrum (labeled “composite”)
2. Theoretical Kaimal spectrum using δ_K as boundary layer depth (labeled “Kaimal, δ_K ”).
3. Theoretical Kaimal spectrum using δ_{HF} as boundary layer depth (labeled “Kaimal, δ_{HF} ”).
4. Log average spectrum (labeled “log av”).
5. -2/3 reference lines (labeled “-2/3 ref line”) for comparison in the inertial sub-range.
6. See Fig. A.1 for all other quantities.

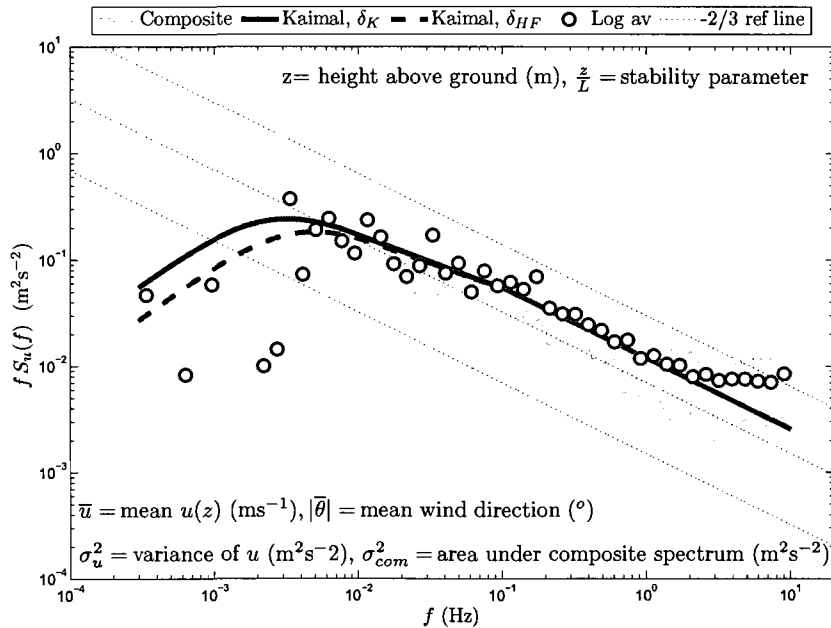


Figure A.1: Description of the first 5 sub-figures.

The last sub-figure provides the normalized log average spectra from different heights in normalized frequency space (see Fig.A.2 for more details). (Note that the

spectral curves from sonic anemometers nos. 10-13 were average together to represent the spectrum at $z = 3$ m above ground.)

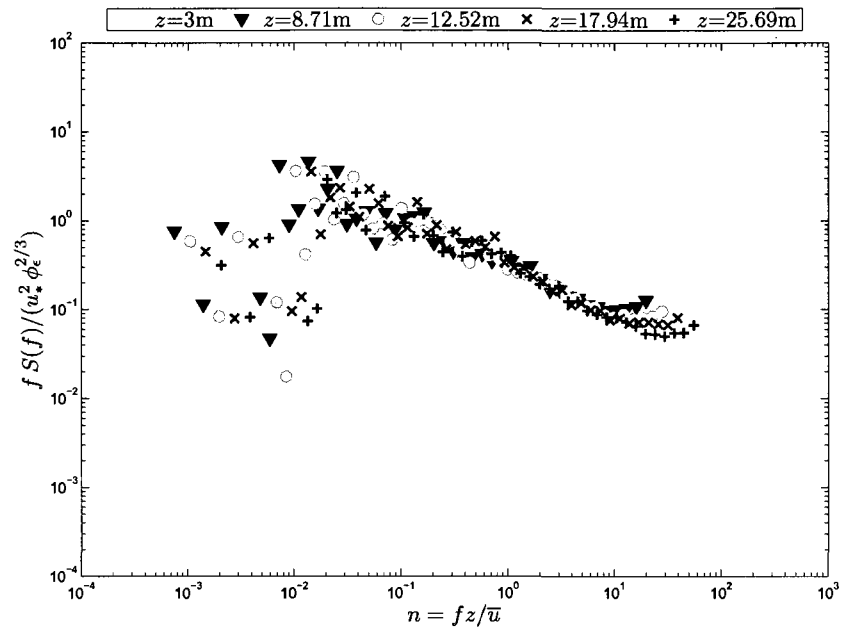
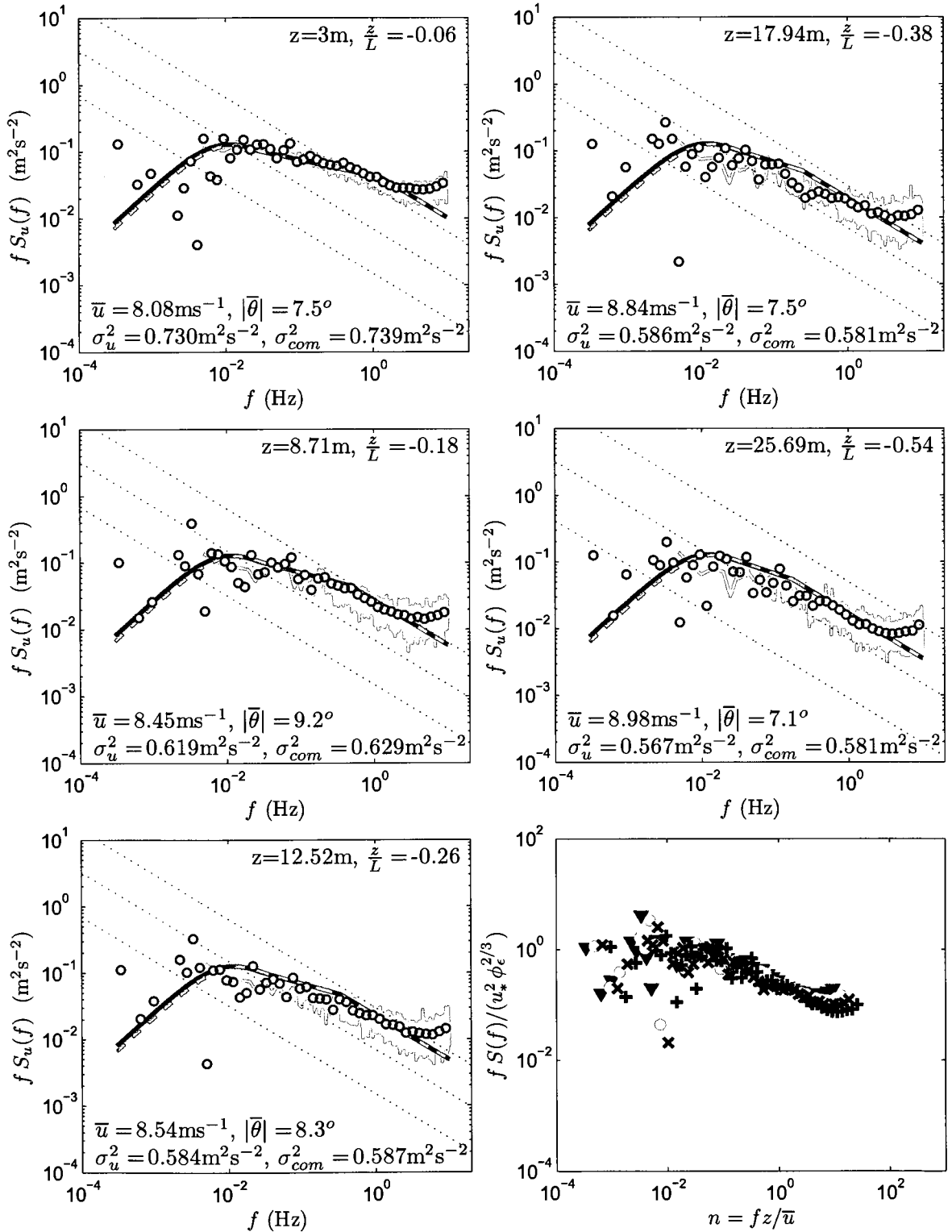
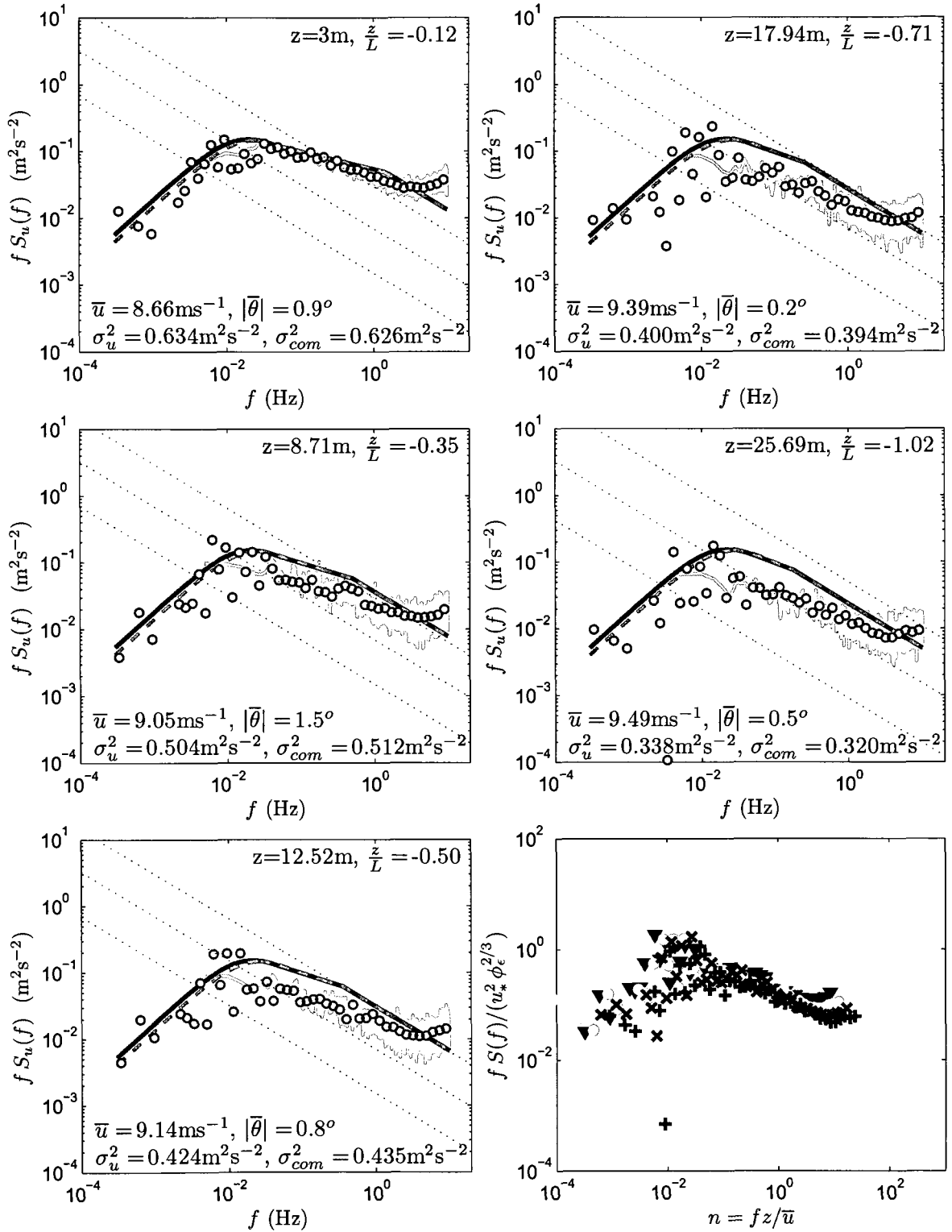


Figure A.2: Description of the last sub-figure

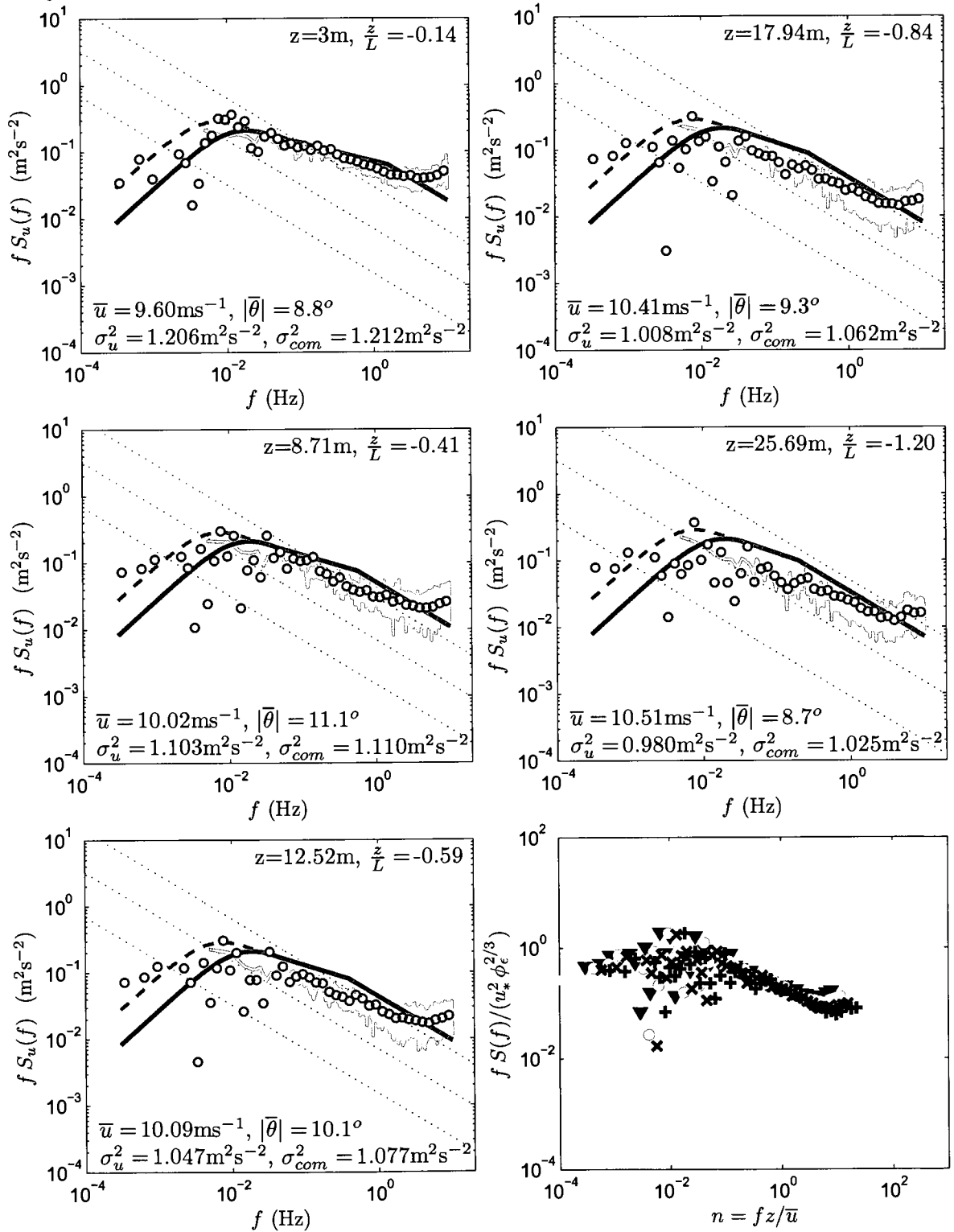
May.24,2005 08:46MDT, $L = -47.7$ m, $u_* = 0.274\text{ms}^{-1}$, $\delta_K = 469.3\text{m}$, $\delta_{HF} = 398.9\text{m}$



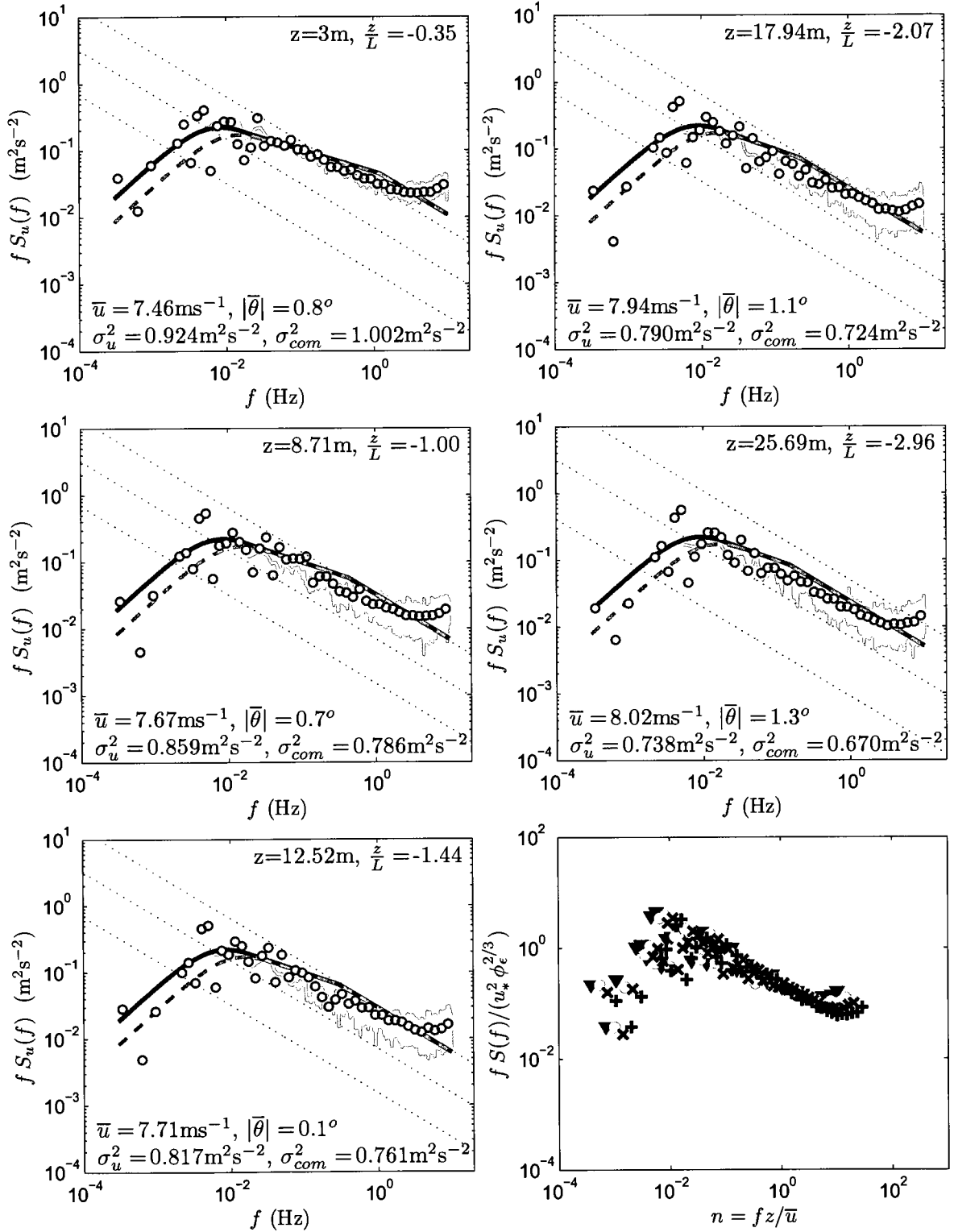
May.24,2005 09:46MDT, $L = -25.1 \text{ m}$, $u_* = 0.295 \text{ ms}^{-1}$, $\delta_K = 279.3 \text{ m}$, $\delta_{HF} = 227.4 \text{ m}$



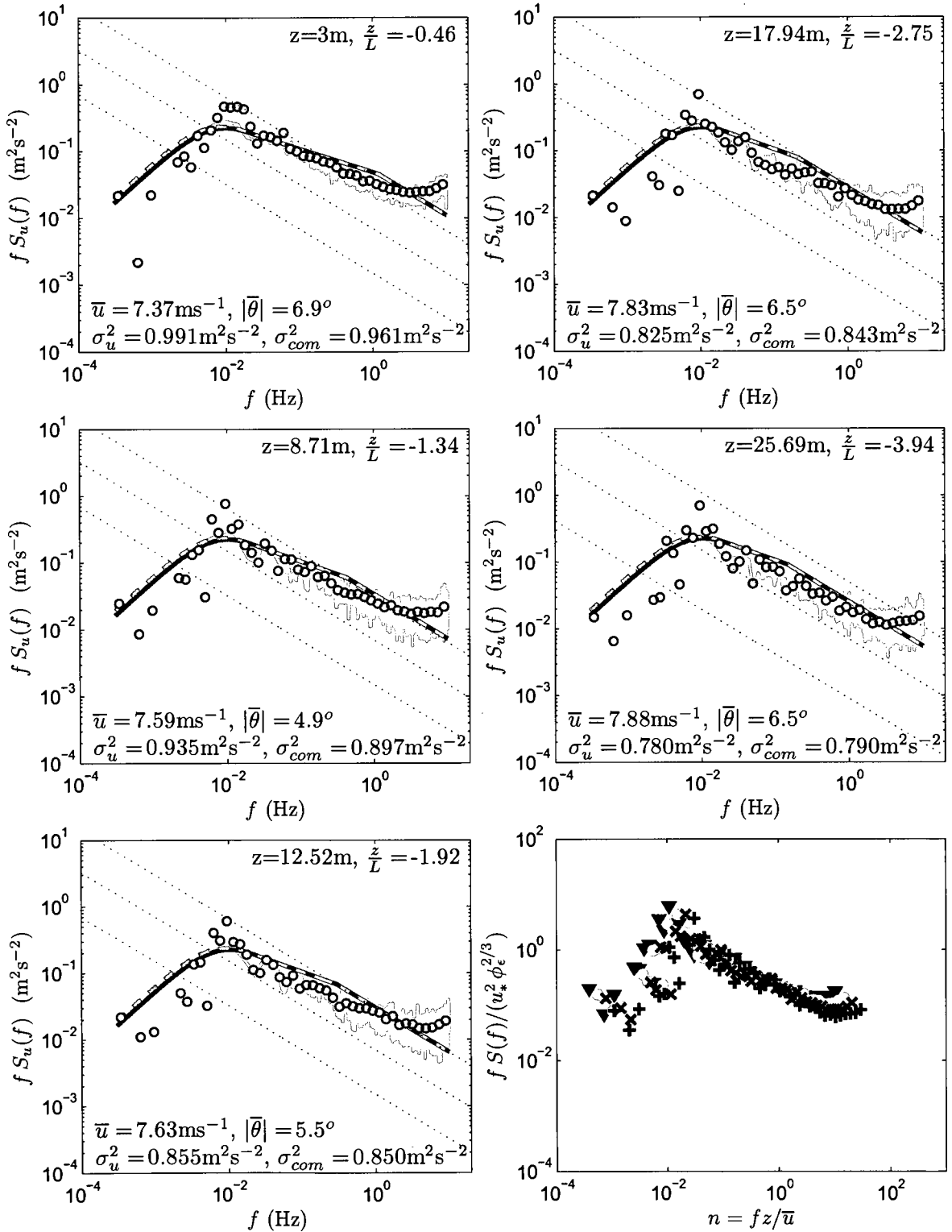
May.24,2005 10:46MDT, $L = -21.4 \text{ m}$, $u_* = 0.332 \text{ ms}^{-1}$, $\delta_K = 343.9 \text{ m}$, $\delta_{HF} = 852.4 \text{ m}$



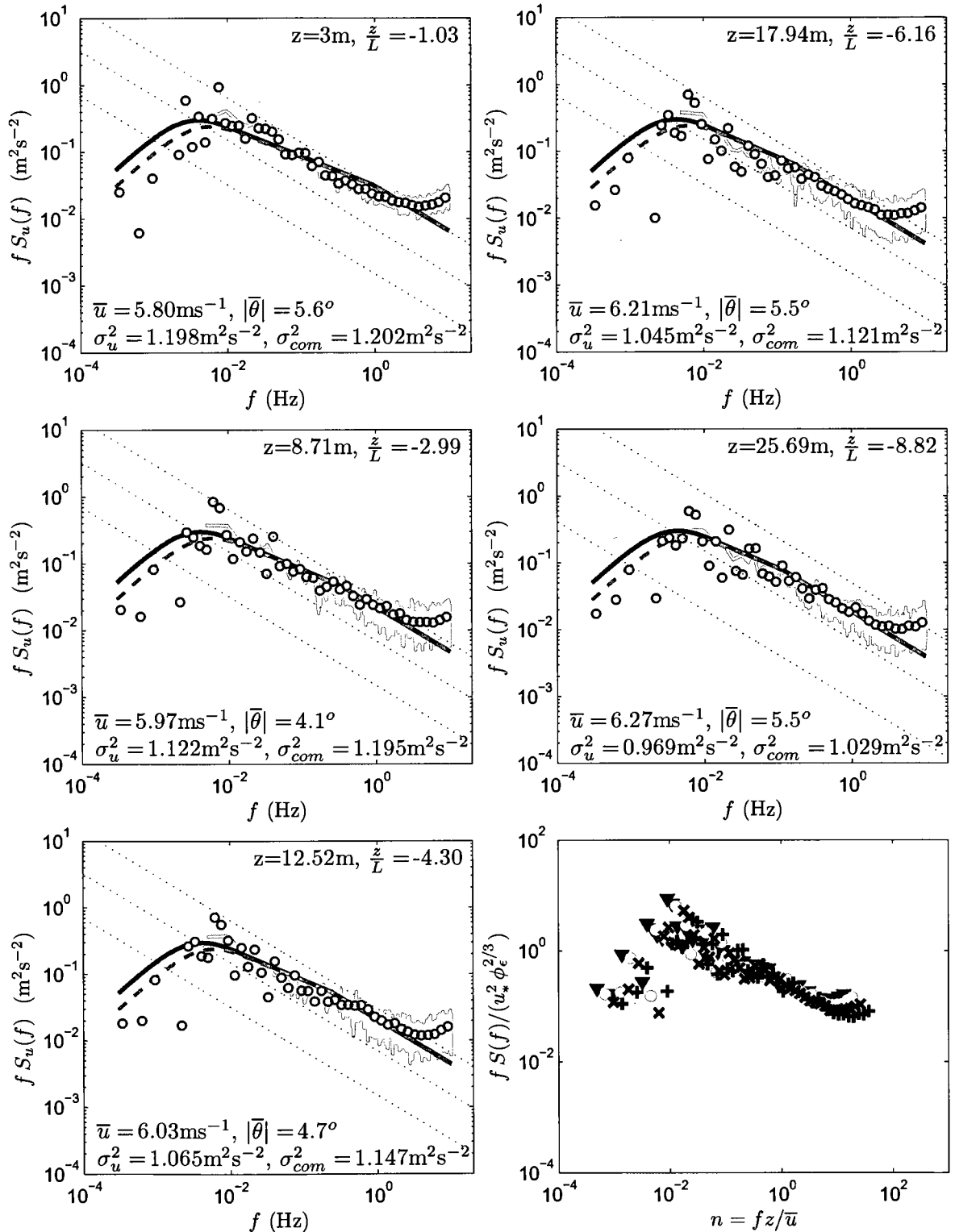
May.24,2005 11:46MDT, $L = -8.7 \text{ m}$, $u_* = 0.260 \text{ ms}^{-1}$, $\delta_K = 567.5 \text{ m}$, $\delta_{HF} = 320.6 \text{ m}$



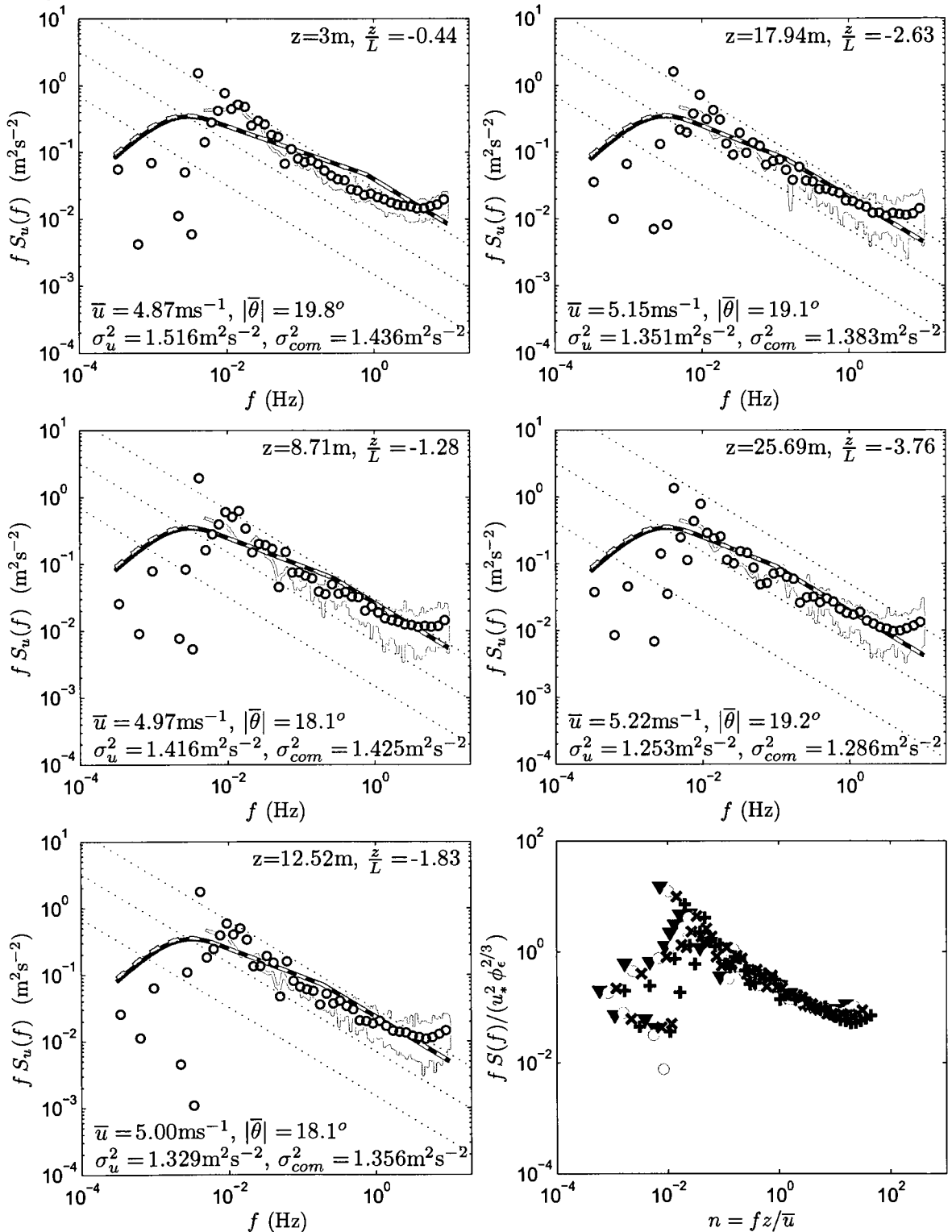
May.24,2005 12:46MDT, $L = -6.5 \text{ m}$, $u_* = 0.255 \text{ ms}^{-1}$, $\delta_K = 479.0 \text{ m}$, $\delta_{HF} = 542.2 \text{ m}$



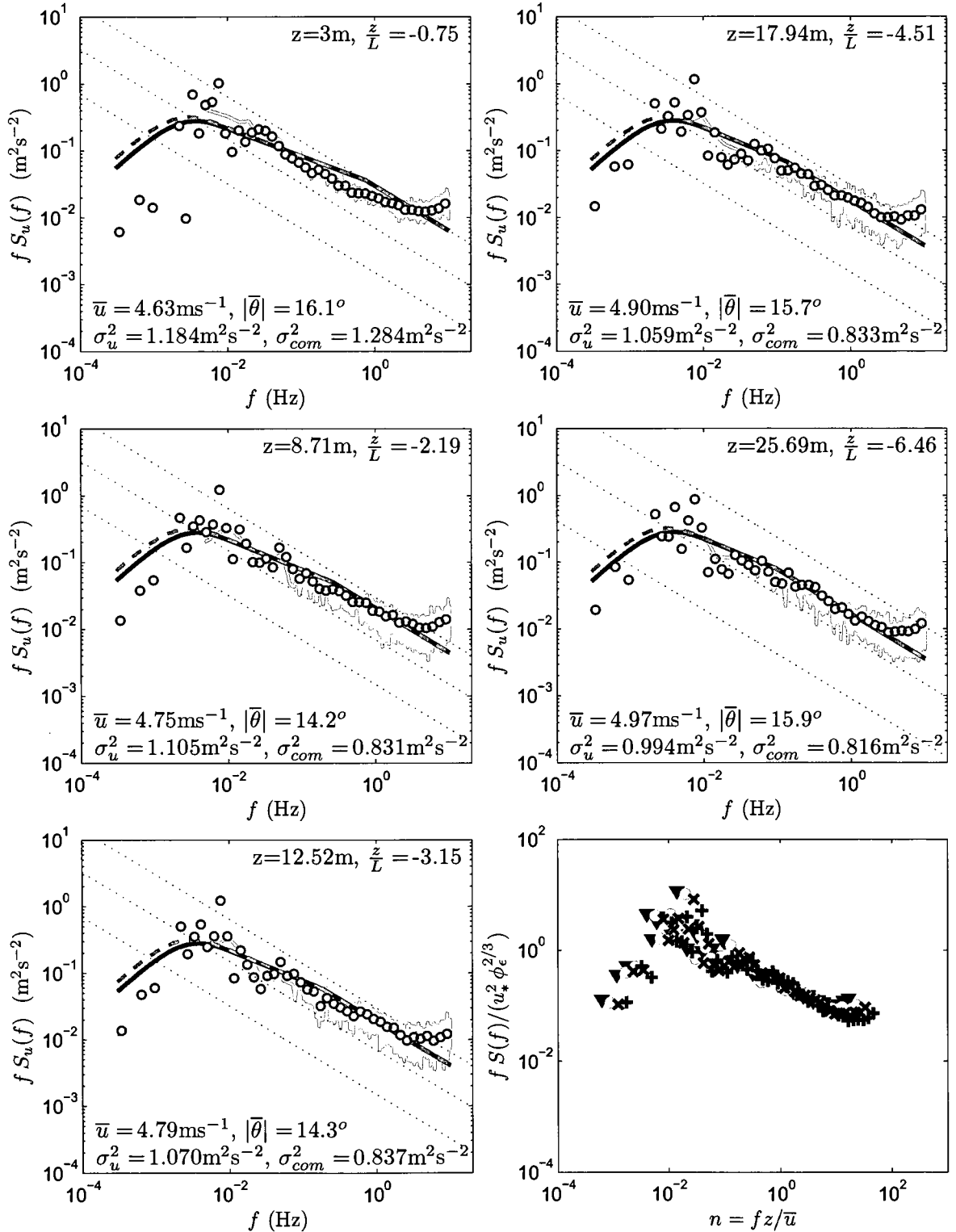
May.24,2005 13:46MDT, $L = -2.9$ m, $u_* = 0.194\text{ms}^{-1}$, $\delta_K = 924.3\text{m}$, $\delta_{HF} = 642.2\text{m}$



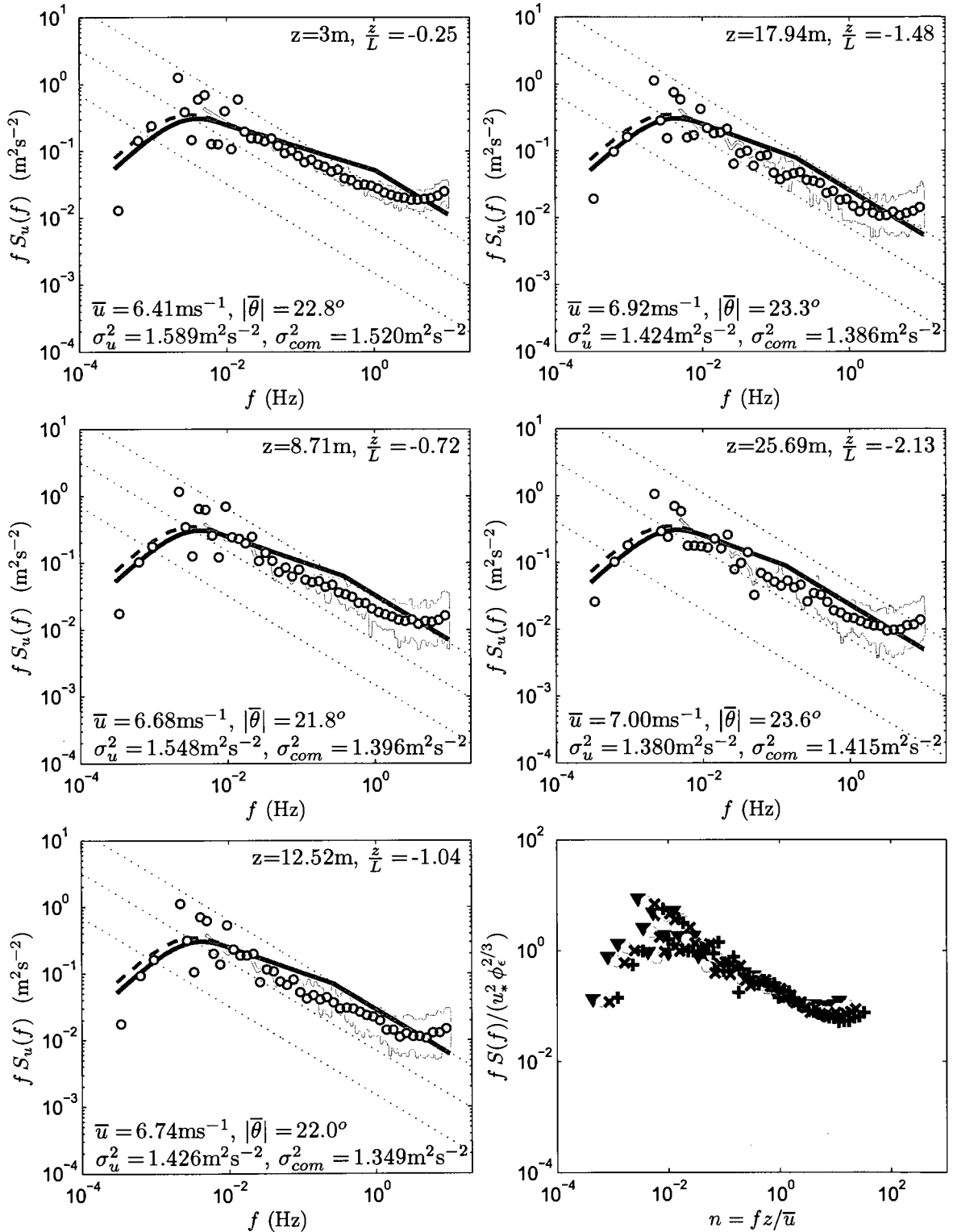
May.24,2005 14:46MDT, $L = -6.8 \text{ m}$, $u_* = 0.260 \text{ ms}^{-1}$, $\delta_K = 1033.8 \text{ m}$, $\delta_{HF} = 1124.2 \text{ m}$



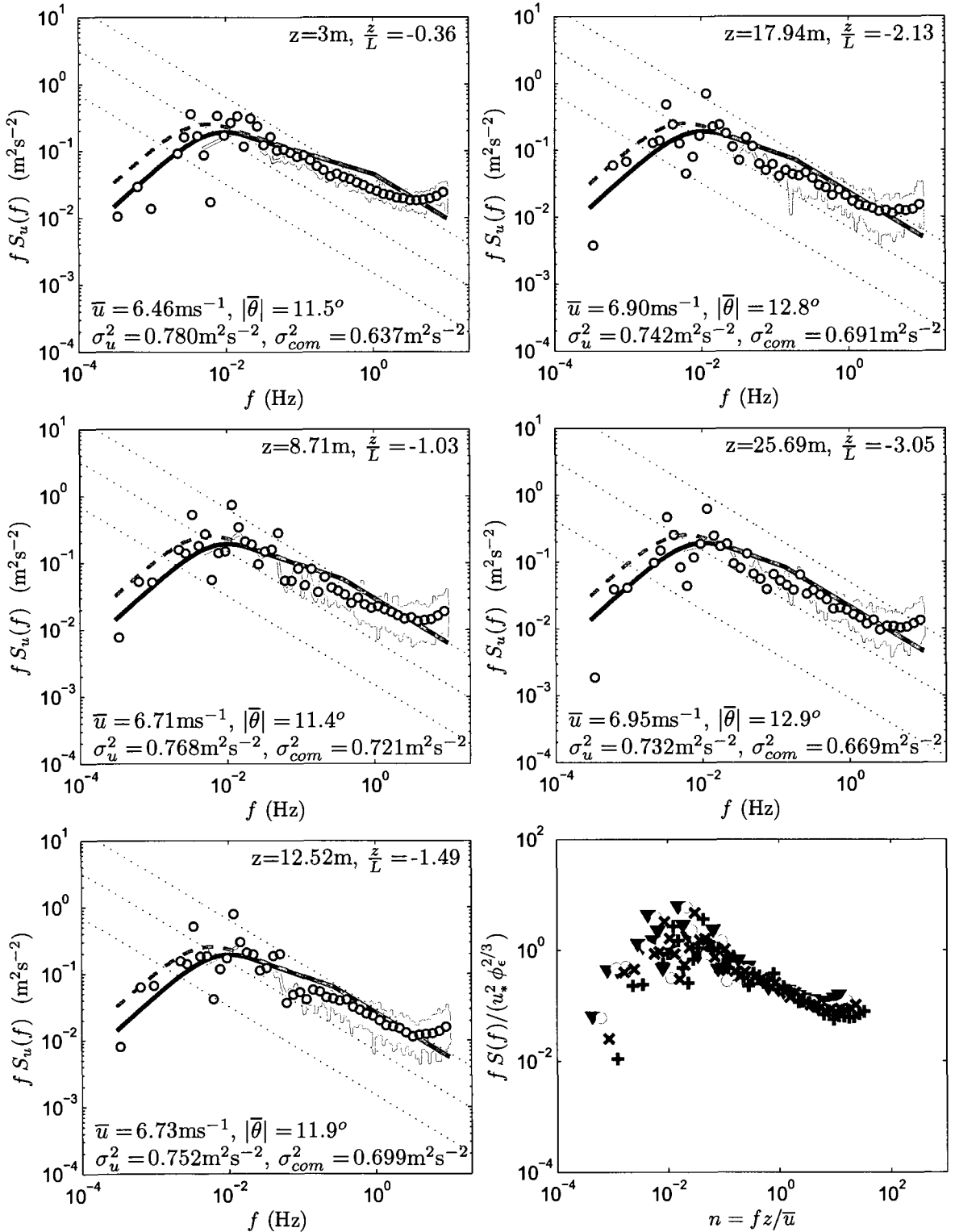
May.24,2005 15:46MDT, $L = -4.0$ m, $u_* = 0.215\text{ms}^{-1}$, $\delta_K = 807.3\text{m}$, $\delta_{HF} = 1002.7\text{m}$



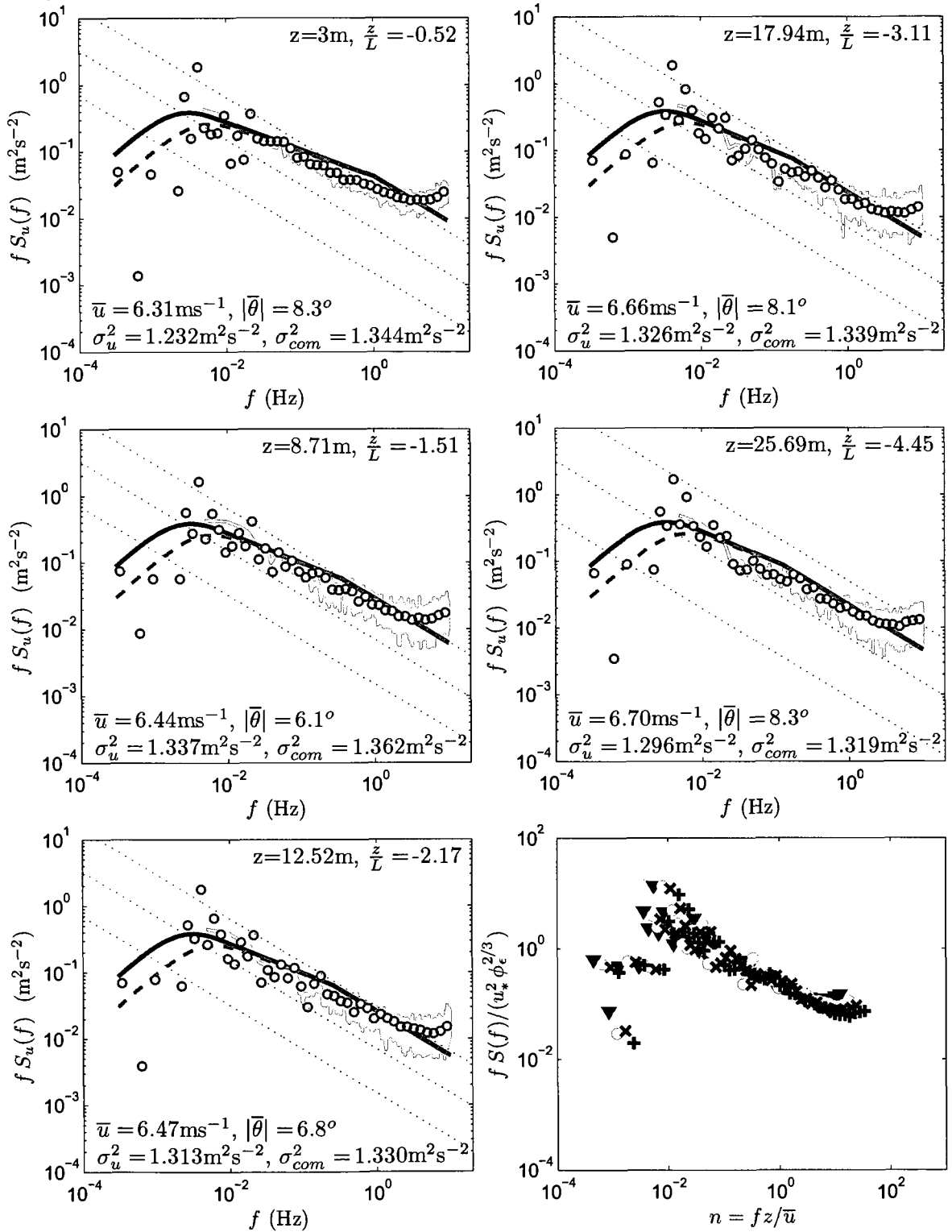
May.24,2005 18:47MDT, $L = -12.1$ m, $u_* = 0.287$ ms⁻¹, $\delta_K = 1015.0$ m, $\delta_{HF} = 1294.9$ m



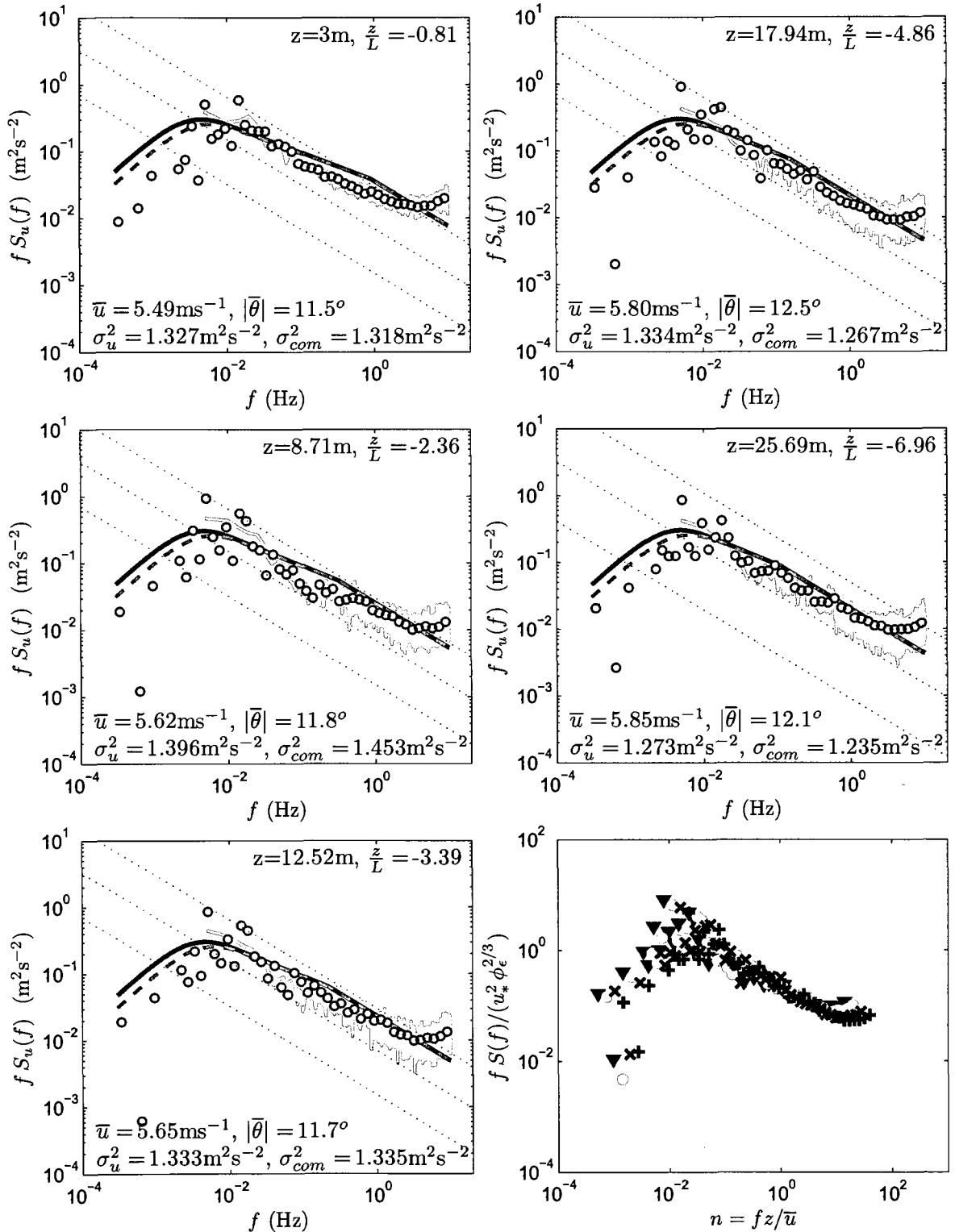
May.25,2005 11:47MDT, $L = -8.4 \text{ m}$, $u_* = 0.259 \text{ ms}^{-1}$, $\delta_K = 424.5 \text{ m}$, $\delta_{HF} = 743.6 \text{ m}$



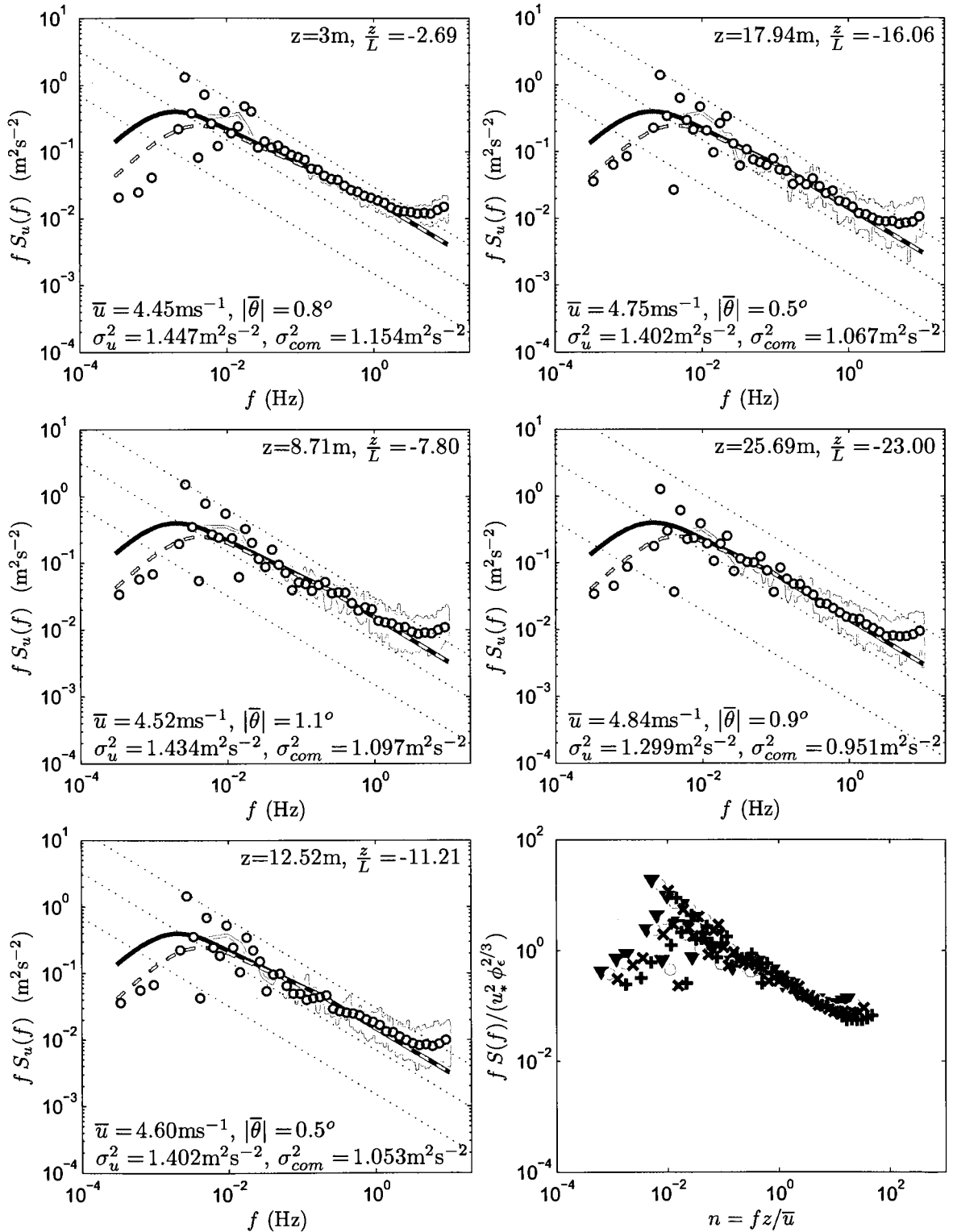
May.25,2005 12:47MDT, $L = -5.8 \text{ m}$, $u_* = 0.243 \text{ ms}^{-1}$, $\delta_K = 1308.9 \text{ m}$, $\delta_{HF} = 659.6 \text{ m}$



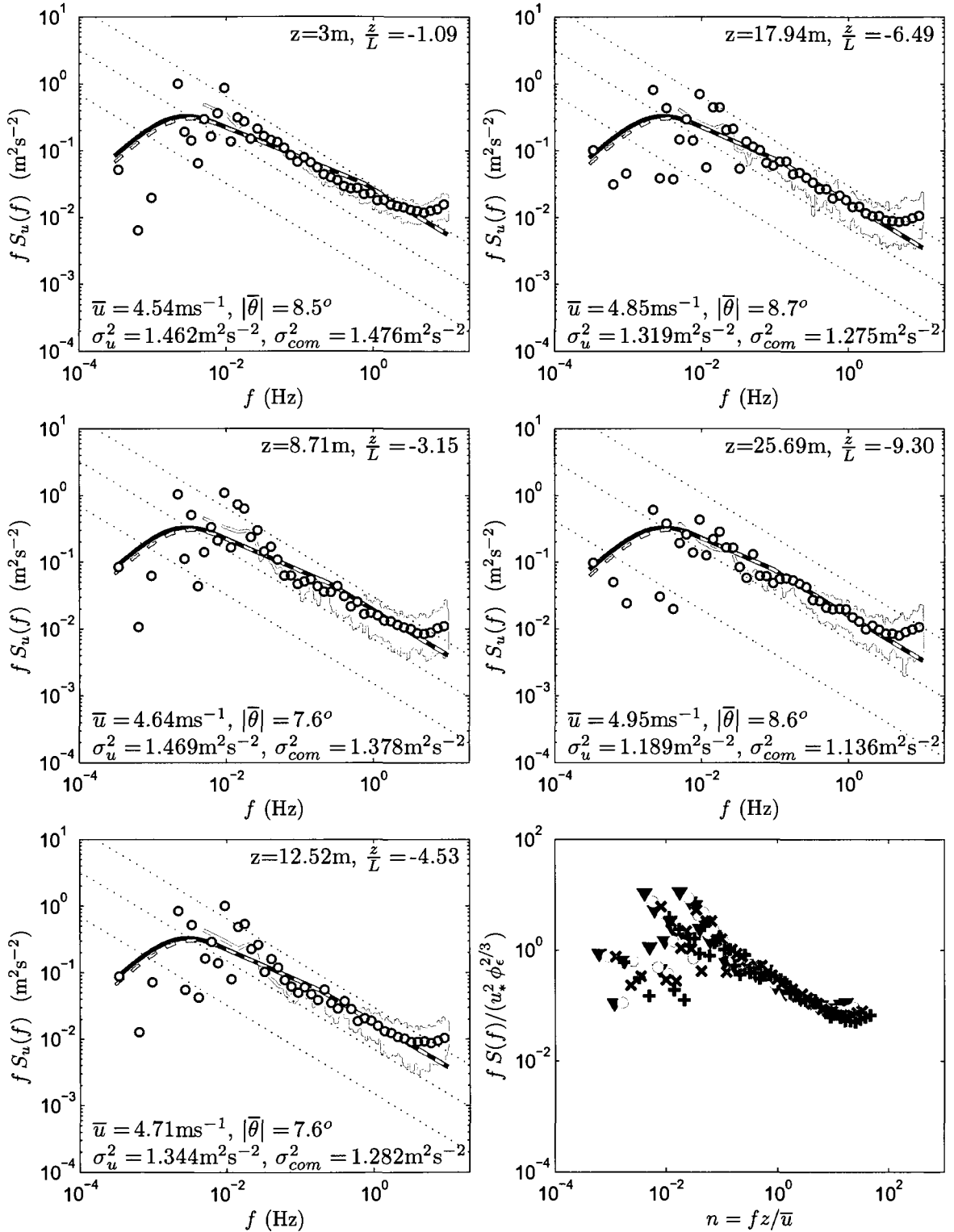
May.25,2005 13:47MDT, $L = -3.7$ m, $u_* = 0.220\text{ms}^{-1}$, $\delta_K = 788.1\text{m}$, $\delta_{HF} = 597.7\text{m}$



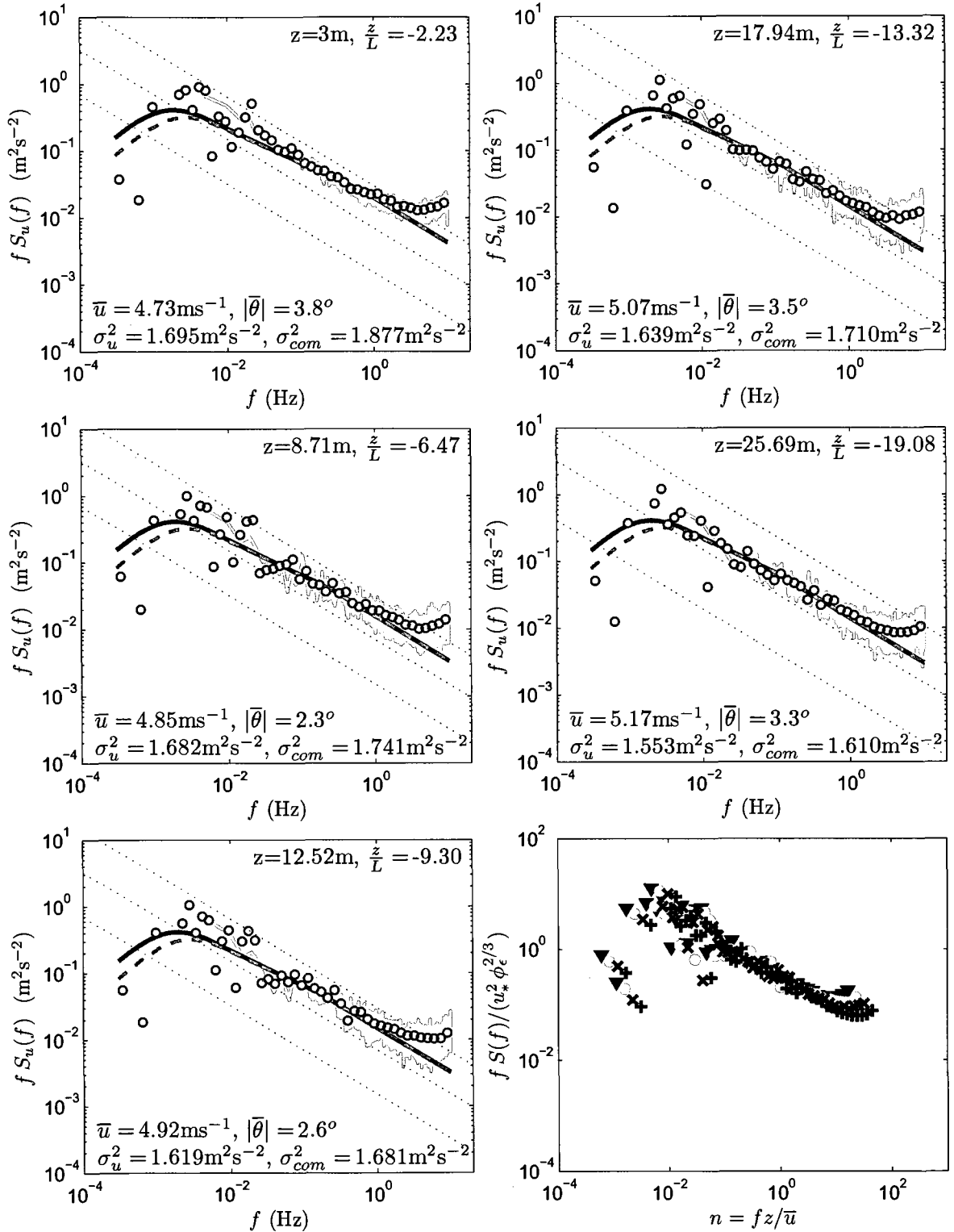
May.25,2005 14:47MDT, $L = -1.1$ m, $u_* = 0.142\text{ms}^{-1}$, $\delta_K = 1454.4\text{m}$, $\delta_{HF} = 691.1\text{m}$



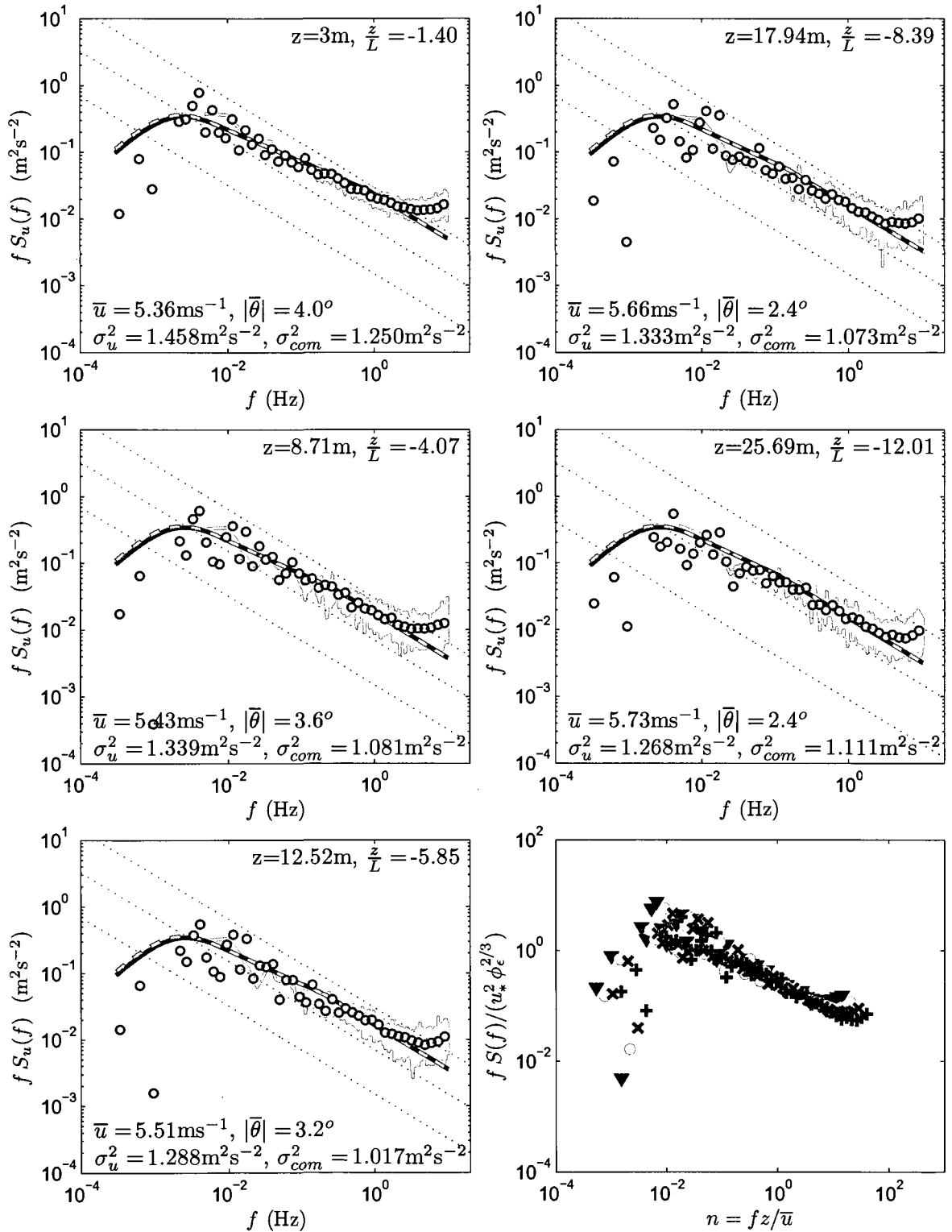
May.25,2005 15:47MDT, $L = -2.8 \text{ m}$, $u_* = 0.192 \text{ ms}^{-1}$, $\delta_K = 1038.1 \text{ m}$, $\delta_{HF} = 906.8 \text{ m}$



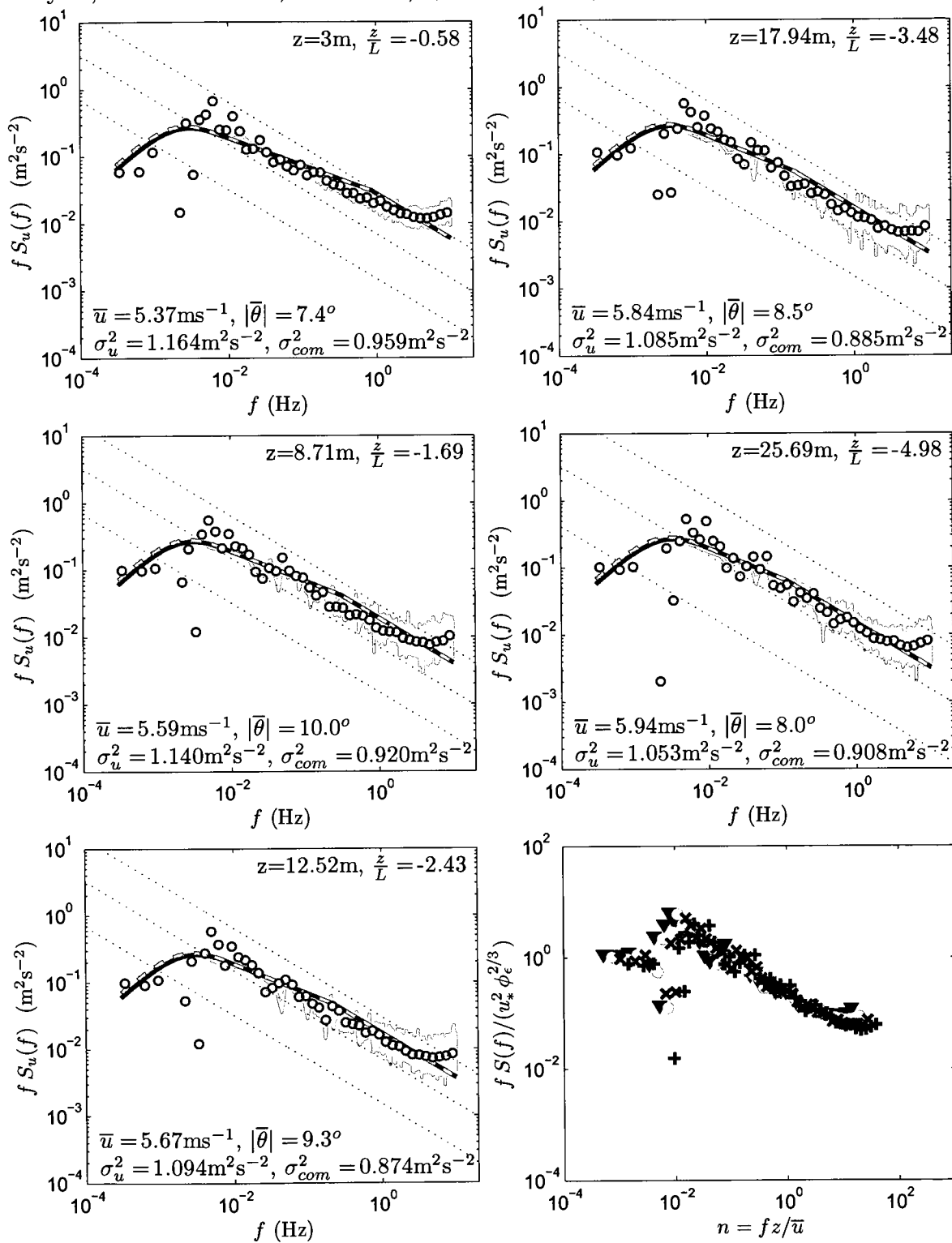
May.25,2005 16:47MDT, $L = -1.3 \text{ m}$, $u_* = 0.147 \text{ ms}^{-1}$, $\delta_K = 1682.3 \text{ m}$, $\delta_{HF} = 1138.8 \text{ m}$



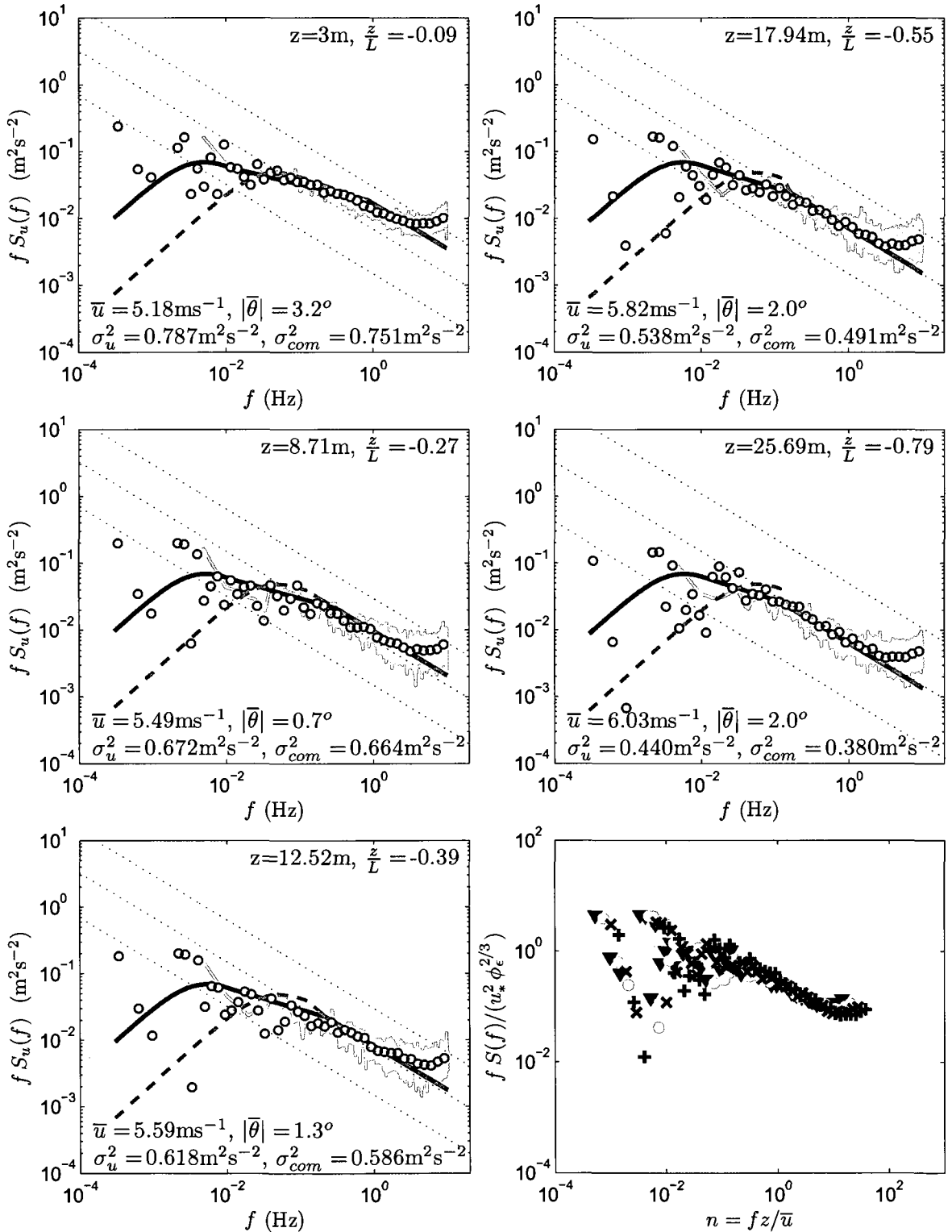
May.25,2005 17:47MDT, $L = -2.1$ m, $u_* = 0.167\text{ms}^{-1}$, $\delta_K = 1368.0\text{m}$, $\delta_{HF} = 1498.2\text{m}$



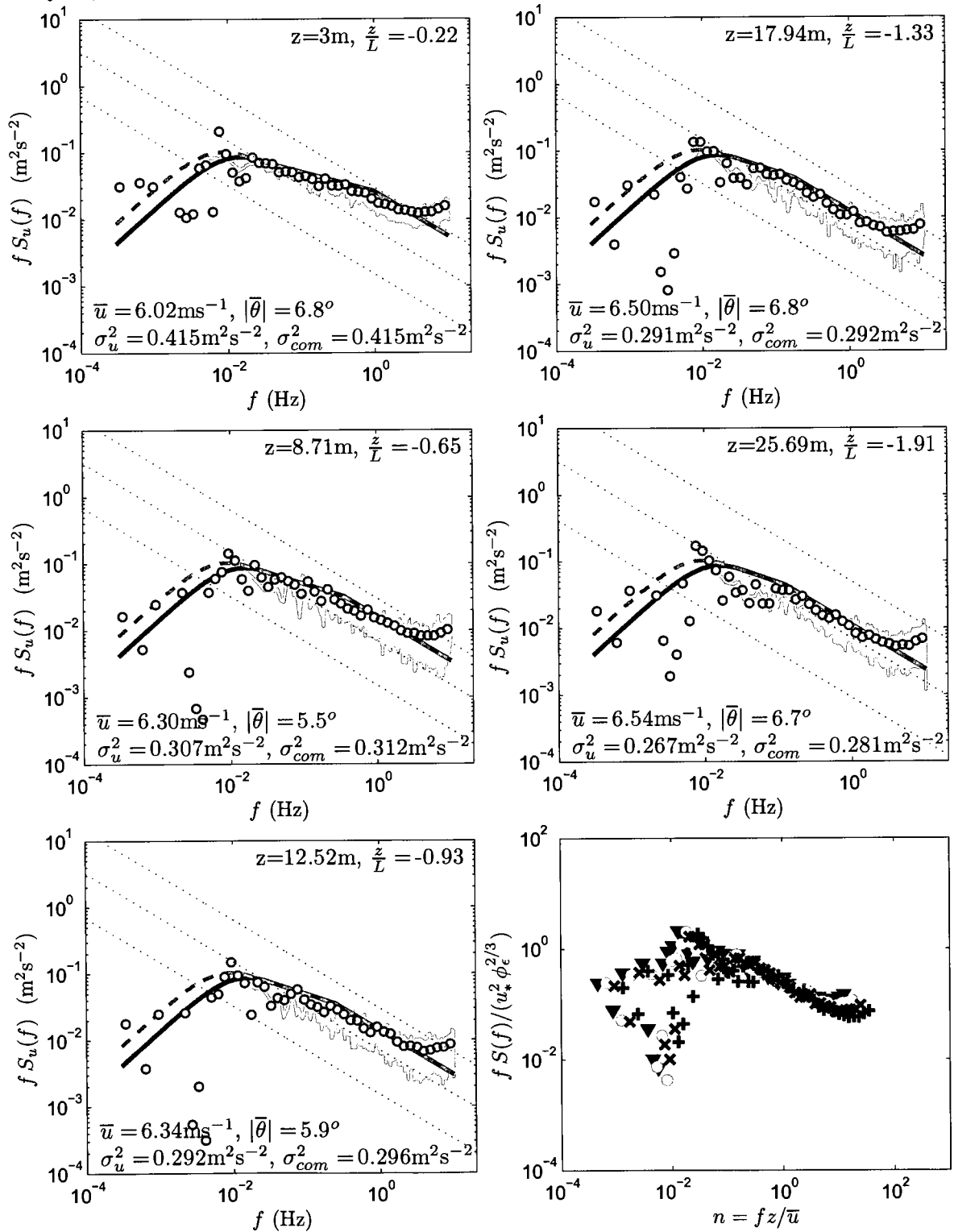
May.25,2005 18:47MDT, $L = -5.2 \text{ m}$, $u_* = 0.203 \text{ ms}^{-1}$, $\delta_K = 1142.5 \text{ m}$, $\delta_{HF} = 1278.0 \text{ m}$



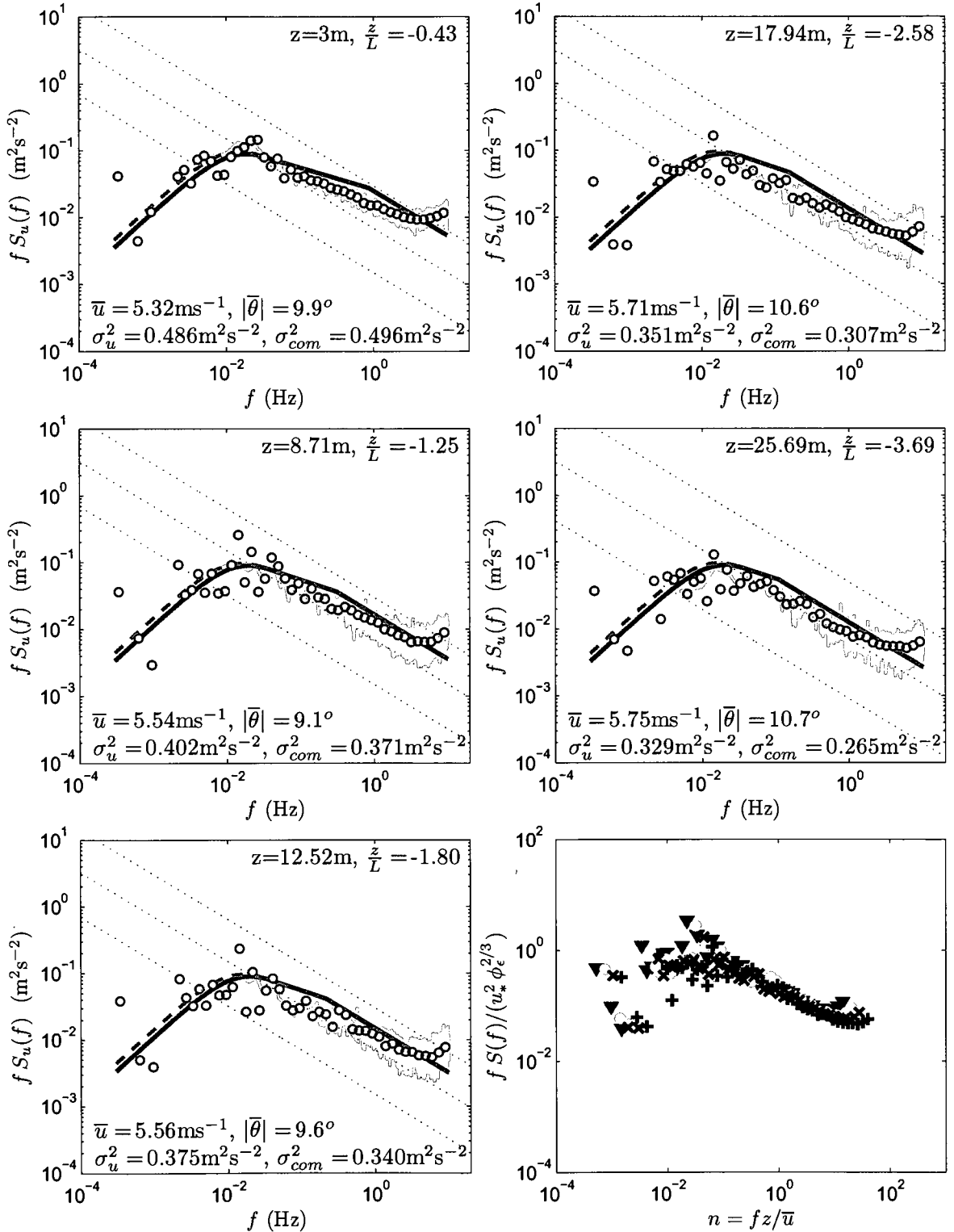
May.26,2005 08:47MDT, $L = -32.5$ m, $u_* = 0.184\text{ms}^{-1}$, $\delta_K = 668.8\text{m}$, $\delta_{HF} = 67.8\text{m}$



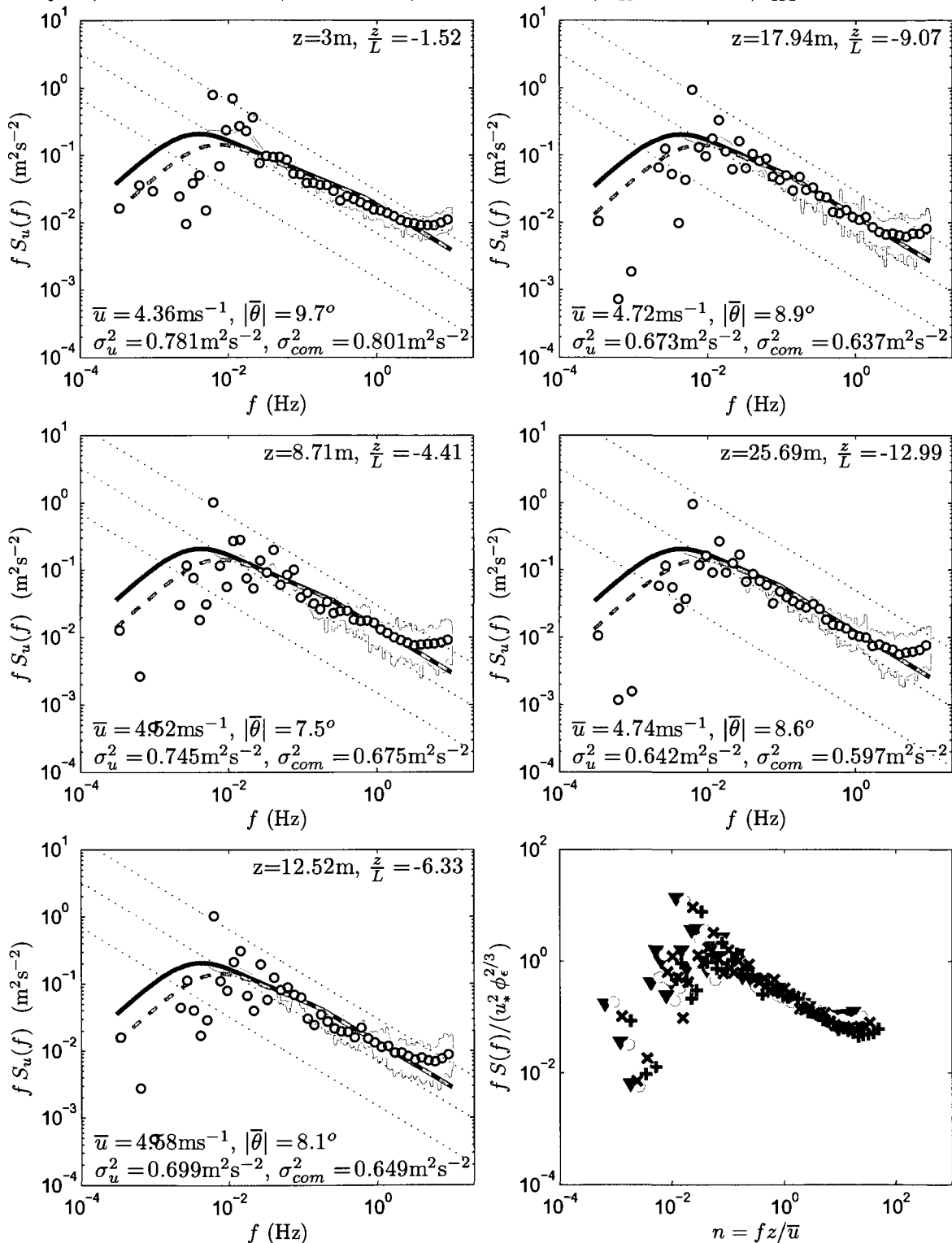
May.26,2005 09:47MDT, $L = -13.5$ m, $u_* = 0.207\text{ms}^{-1}$, $\delta_K = 261.5\text{m}$, $\delta_{HF} = 441.1\text{m}$



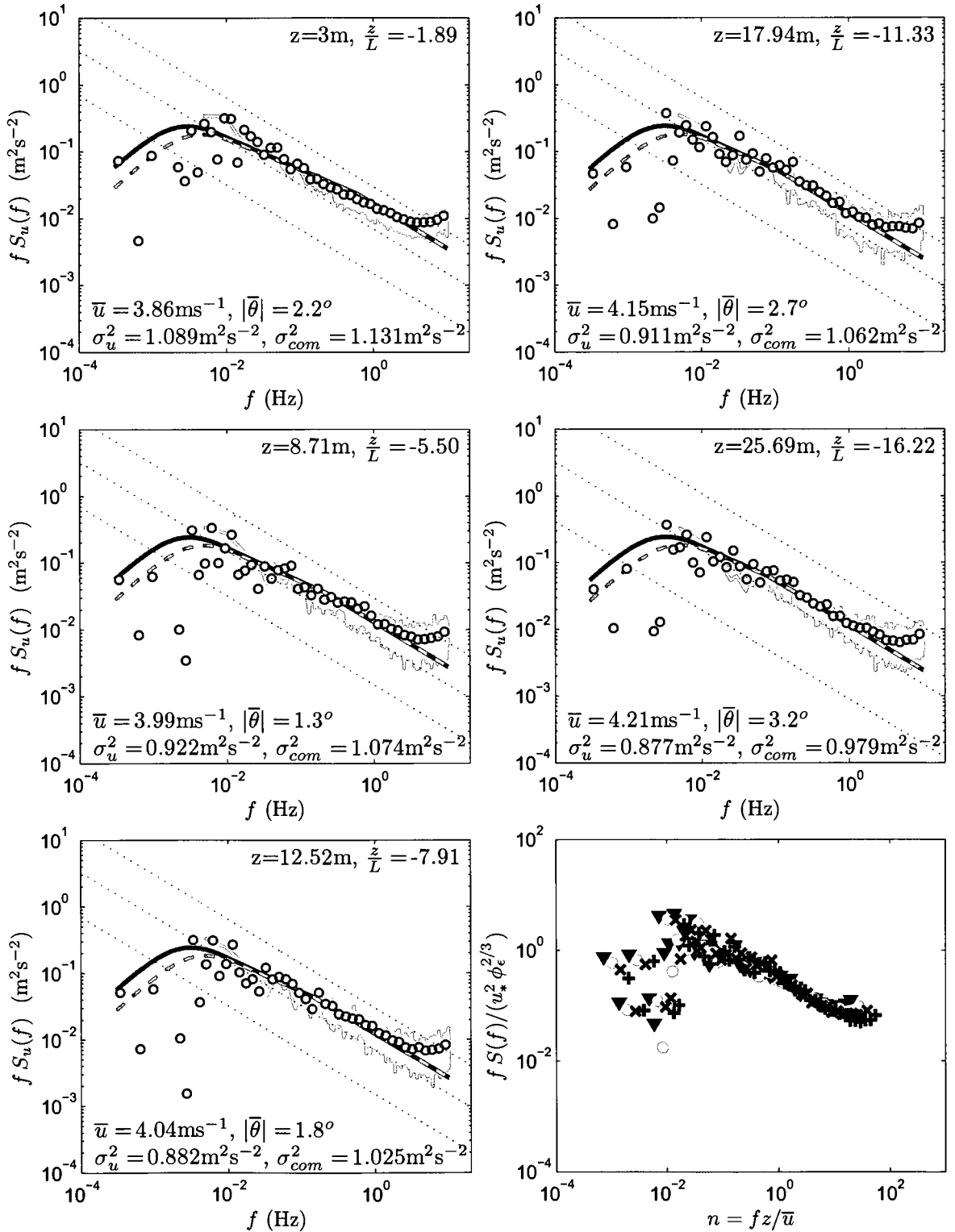
May.26,2005 10:47MDT, $L = -7.0$ m, $u_* = 0.201\text{ms}^{-1}$, $\delta_K = 182.8\text{m}$, $\delta_{HF} = 223.6\text{m}$



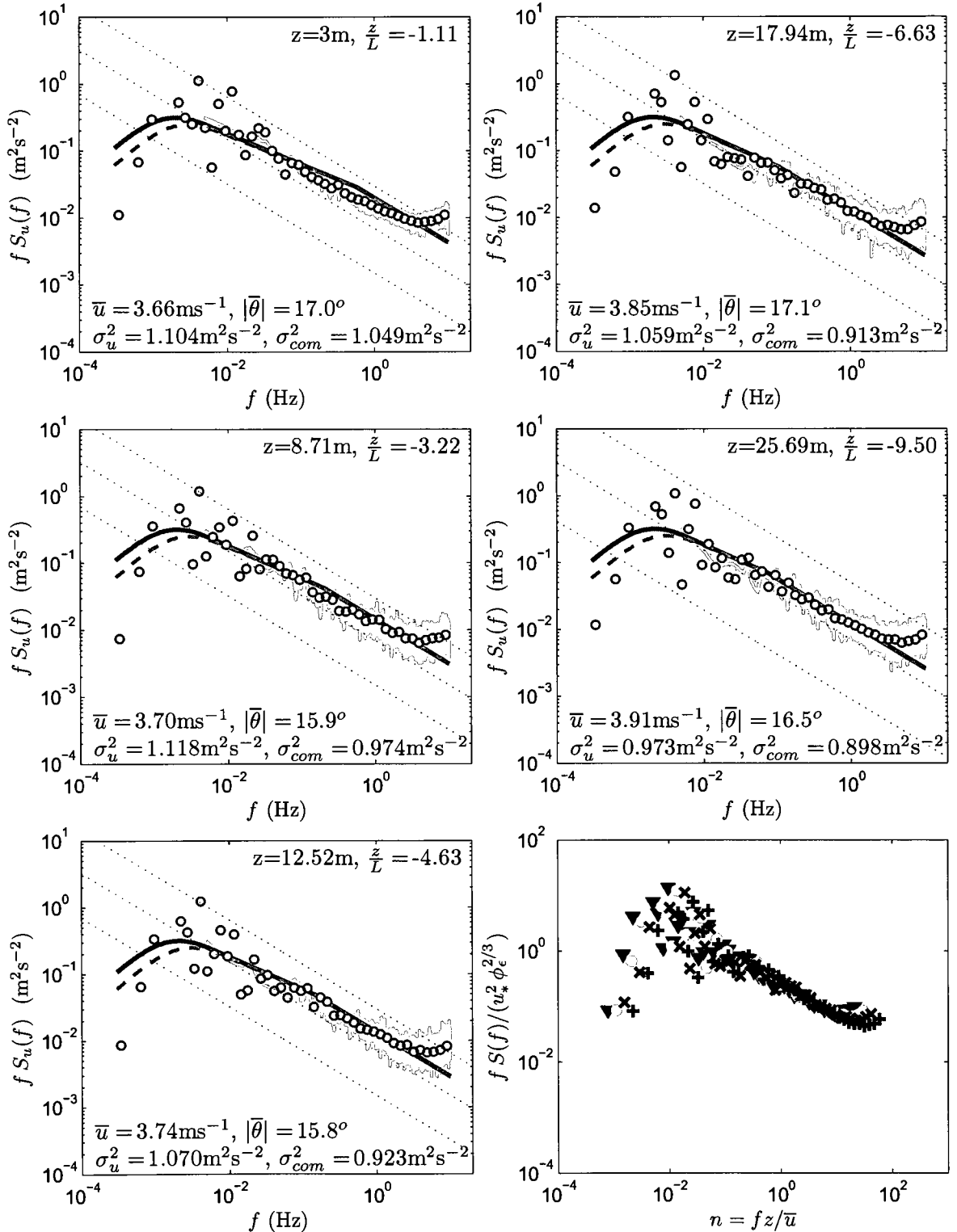
May.26,2005 12:47MDT, $L = -2.0$ m, $u_* = 0.156\text{ms}^{-1}$, $\delta_K = 698.3\text{m}$, $\delta_{HF} = 382.1\text{m}$



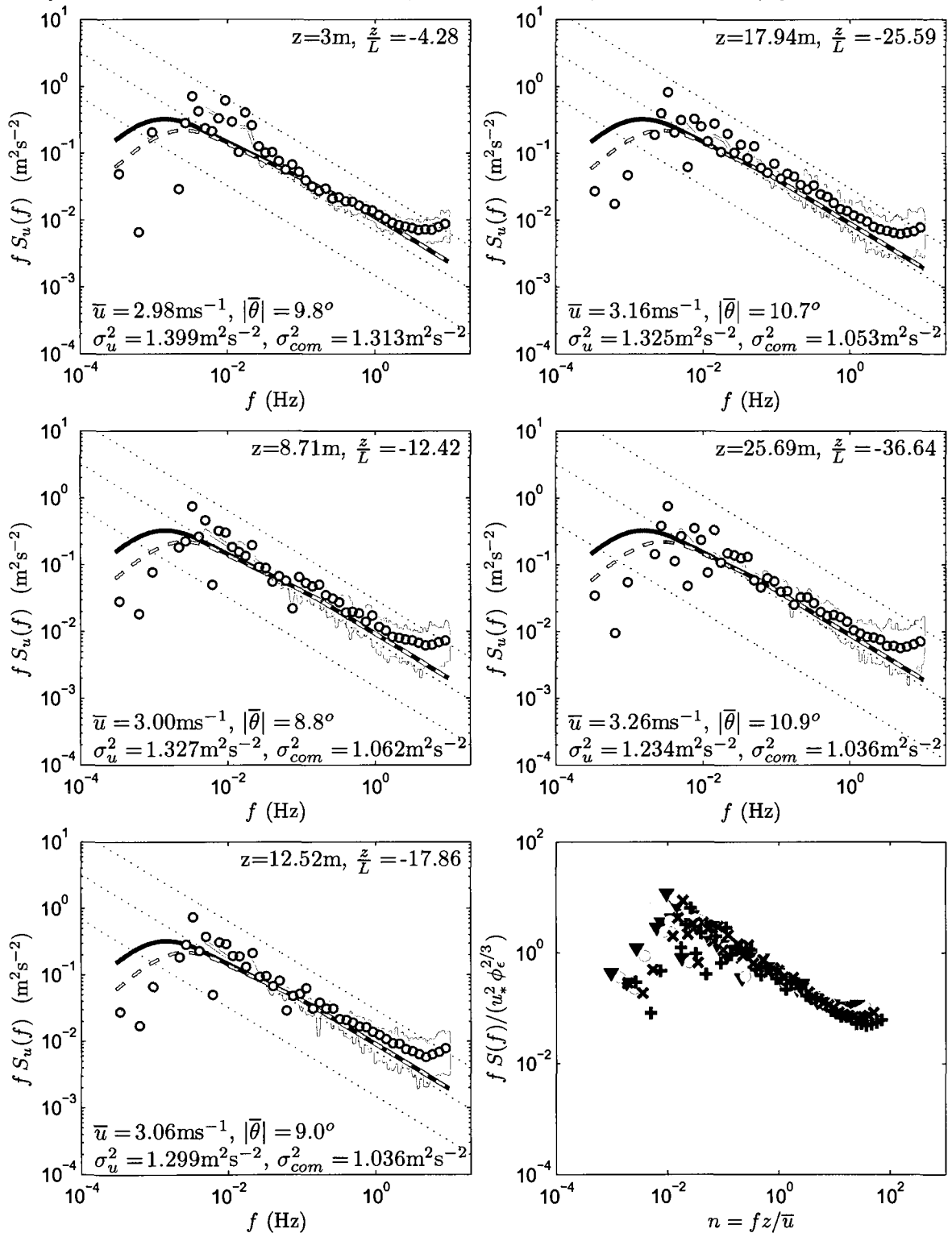
May.26,2005 13:47MDT, $L = -1.6 \text{ m}$, $u_* = 0.148 \text{ ms}^{-1}$, $\delta_K = 842.3 \text{ m}$, $\delta_{HF} = 539.4 \text{ m}$



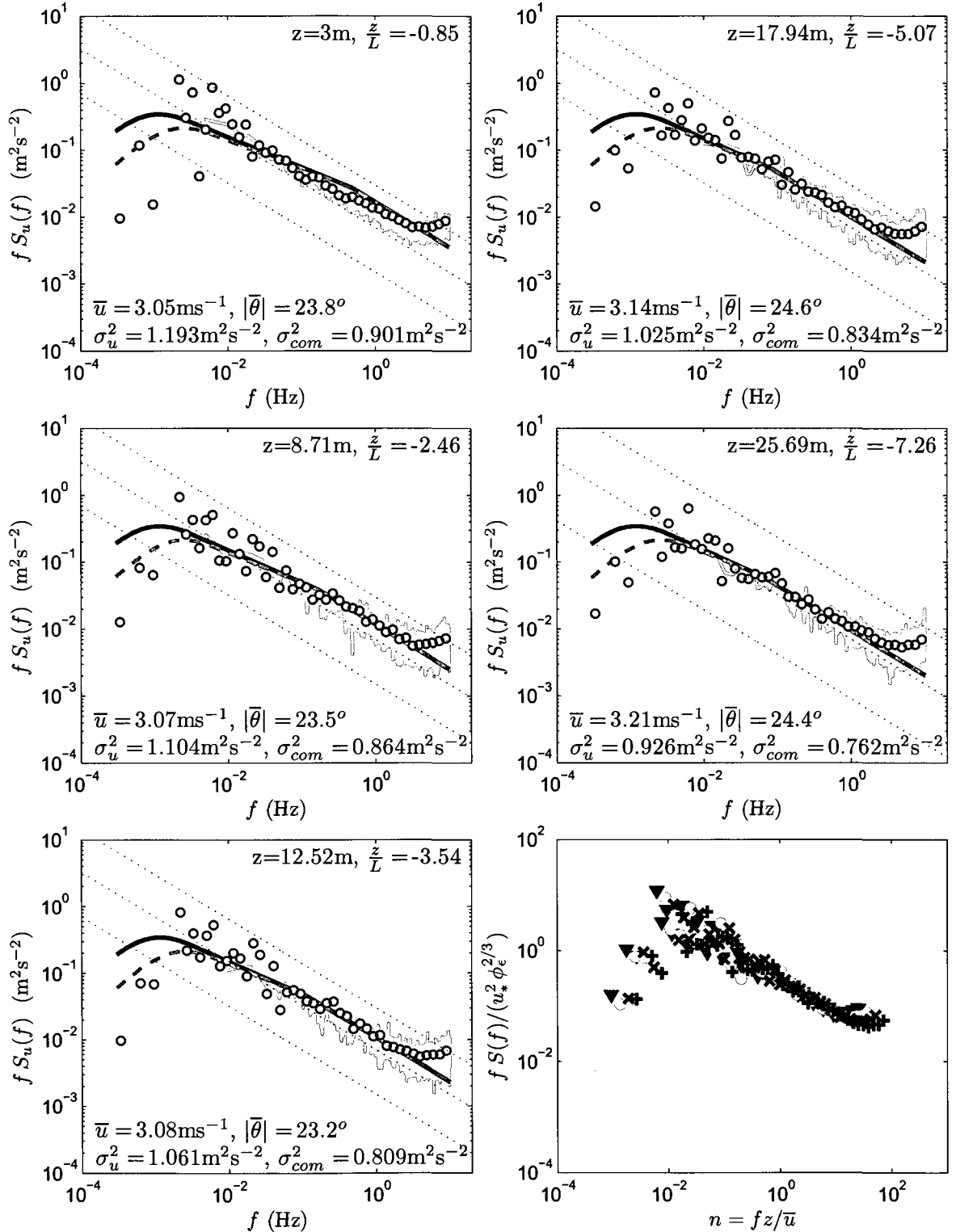
May.26,2005 14:47MDT, $L = -2.7 \text{ m}$, $u_* = 0.180 \text{ ms}^{-1}$, $\delta_K = 1181.4 \text{ m}$, $\delta_{HF} = 807.5 \text{ m}$



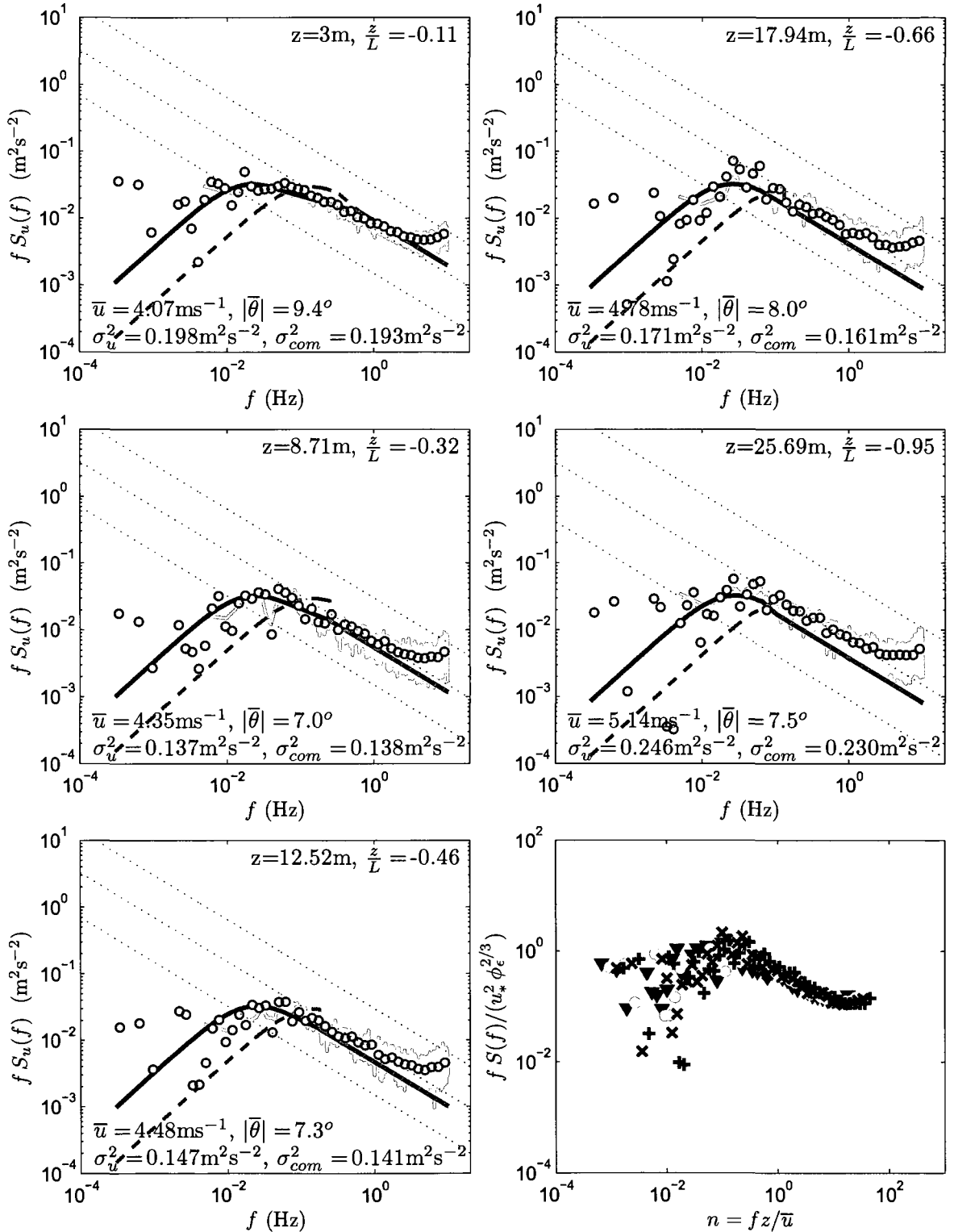
May.26,2005 15:47MDT, $L = -0.7$ m, $u_* = 0.112\text{ms}^{-1}$, $\delta_K = 1374.4\text{m}$, $\delta_{HF} = 756.8\text{m}$



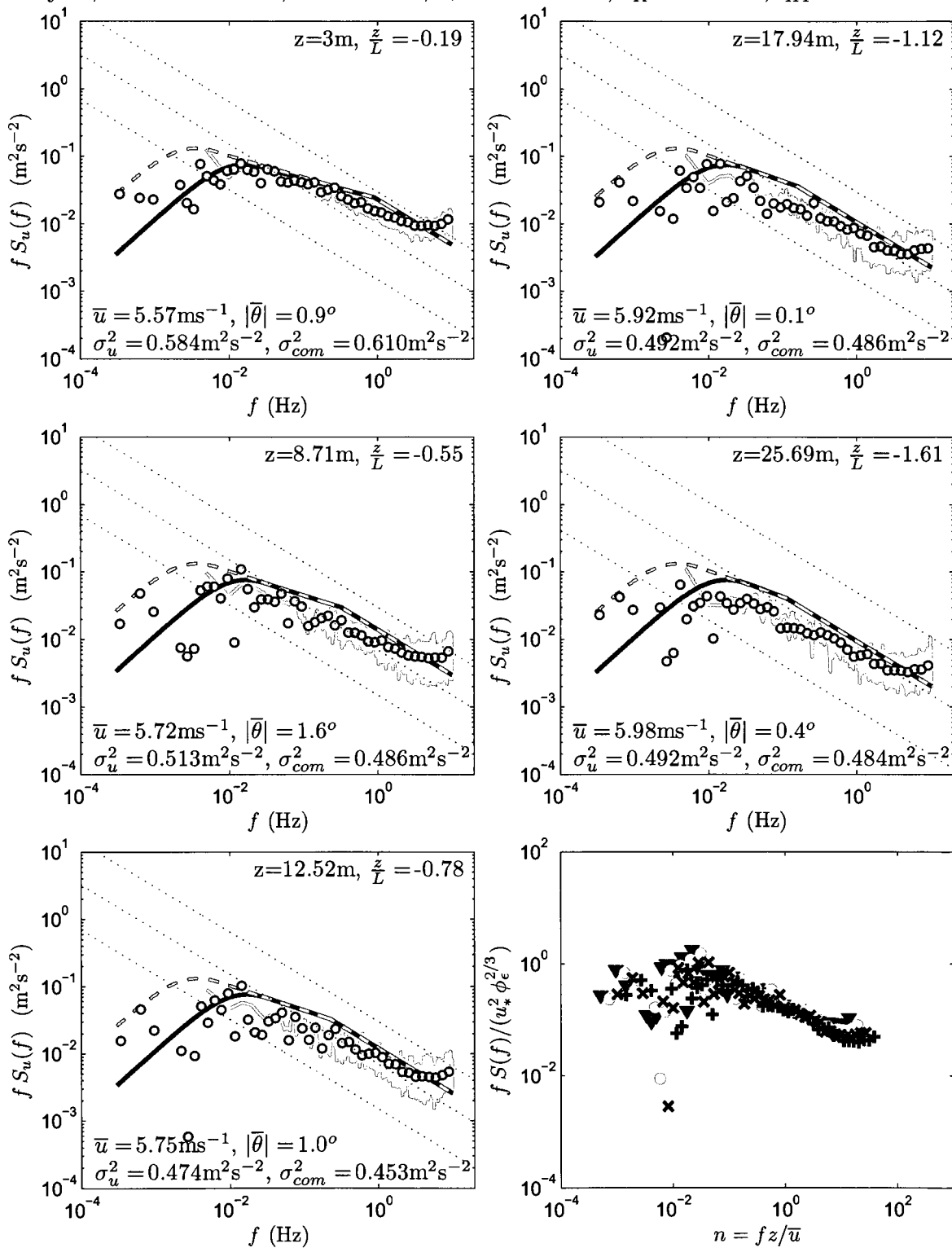
May.26,2005 16:47MDT, $L = -3.5 \text{ m}$, $u_* = 0.182 \text{ ms}^{-1}$, $\delta_K = 1704.4 \text{ m}$, $\delta_{HF} = 789.2 \text{ m}$



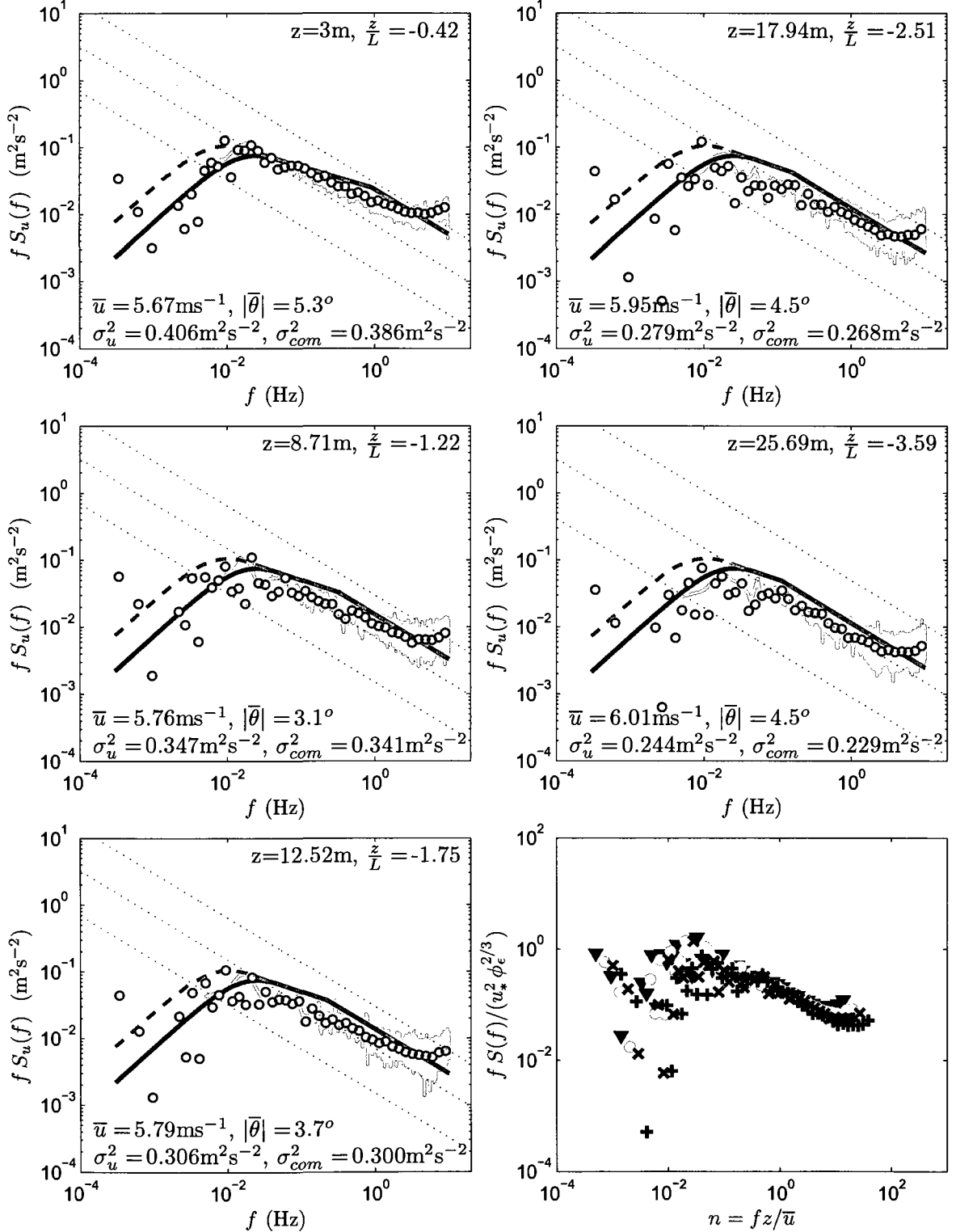
May.27,2005 08:47MDT, $L = -27.1 \text{ m}$, $u_* = 0.146 \text{ ms}^{-1}$, $\delta_K = 117.0 \text{ m}$, $\delta_{HF} = 19.2 \text{ m}$



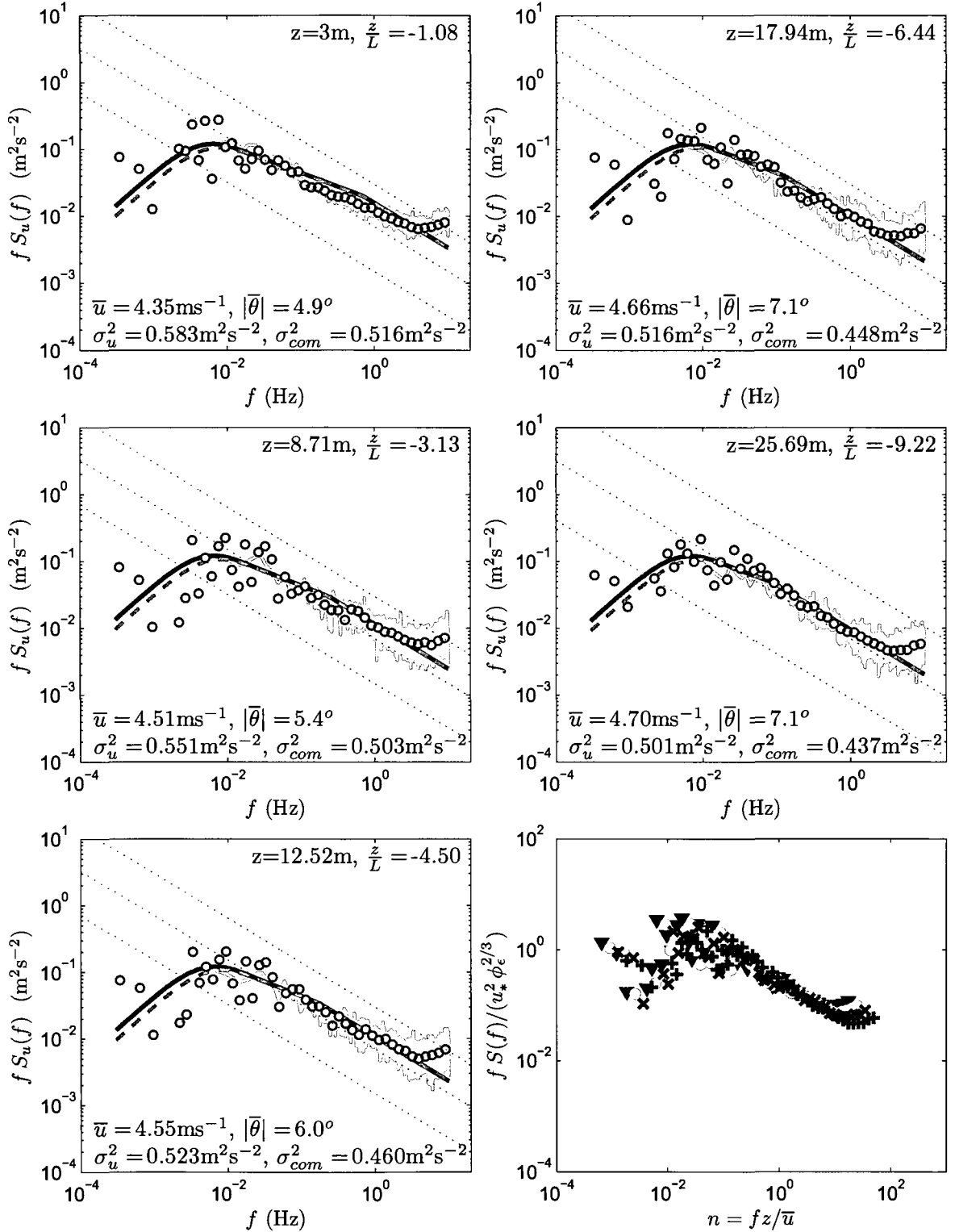
May.27,2005 09:47MDT, $L = -16.0$ m, $u_* = 0.203\text{ms}^{-1}$, $\delta_K = 222.4\text{m}$, $\delta_{HF} = 1008.9\text{m}$



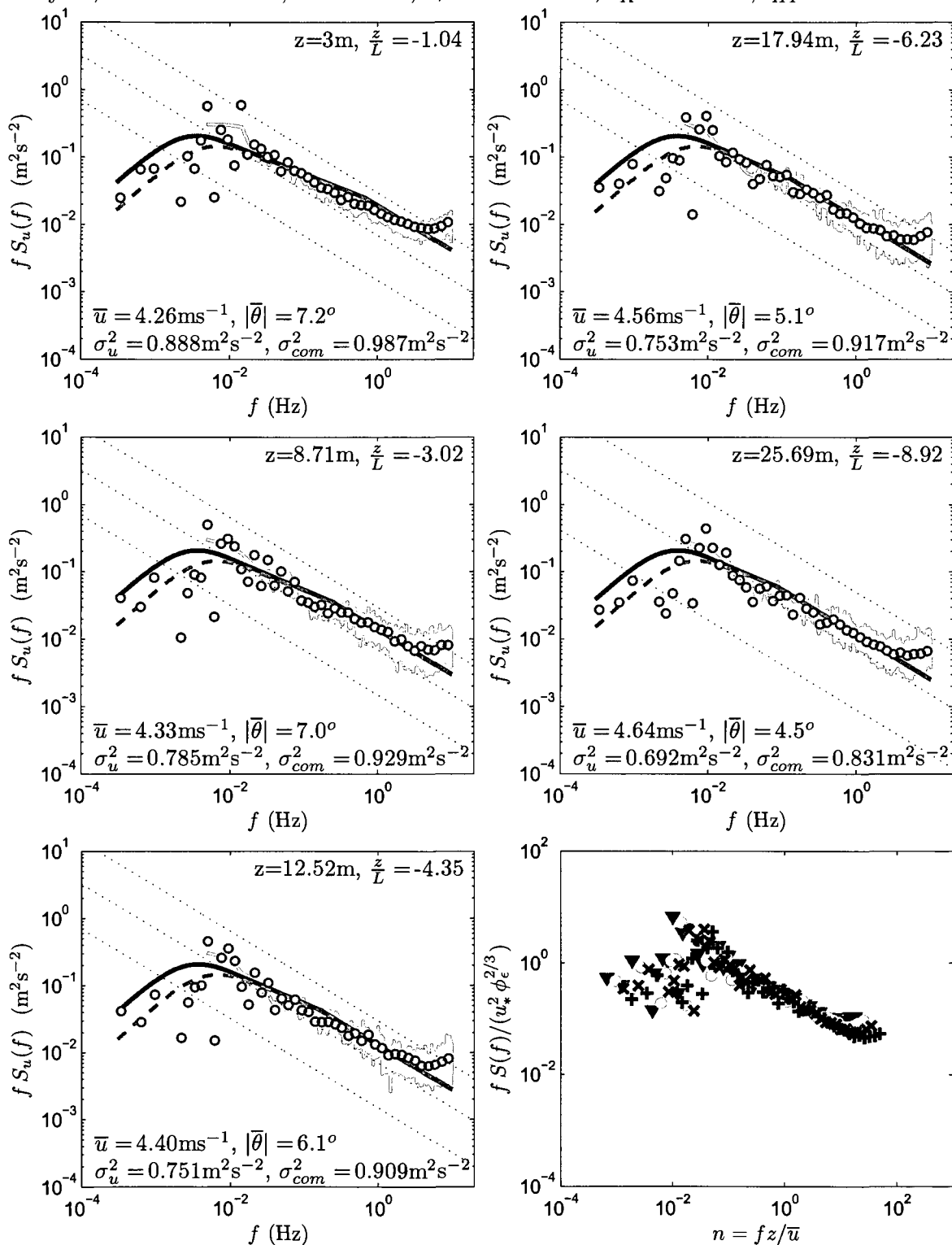
May.27,2005 10:47MDT, $L = -7.2 \text{ m}$, $u_* = 0.191 \text{ ms}^{-1}$, $\delta_K = 147.4 \text{ m}$, $\delta_{HF} = 359.5 \text{ m}$



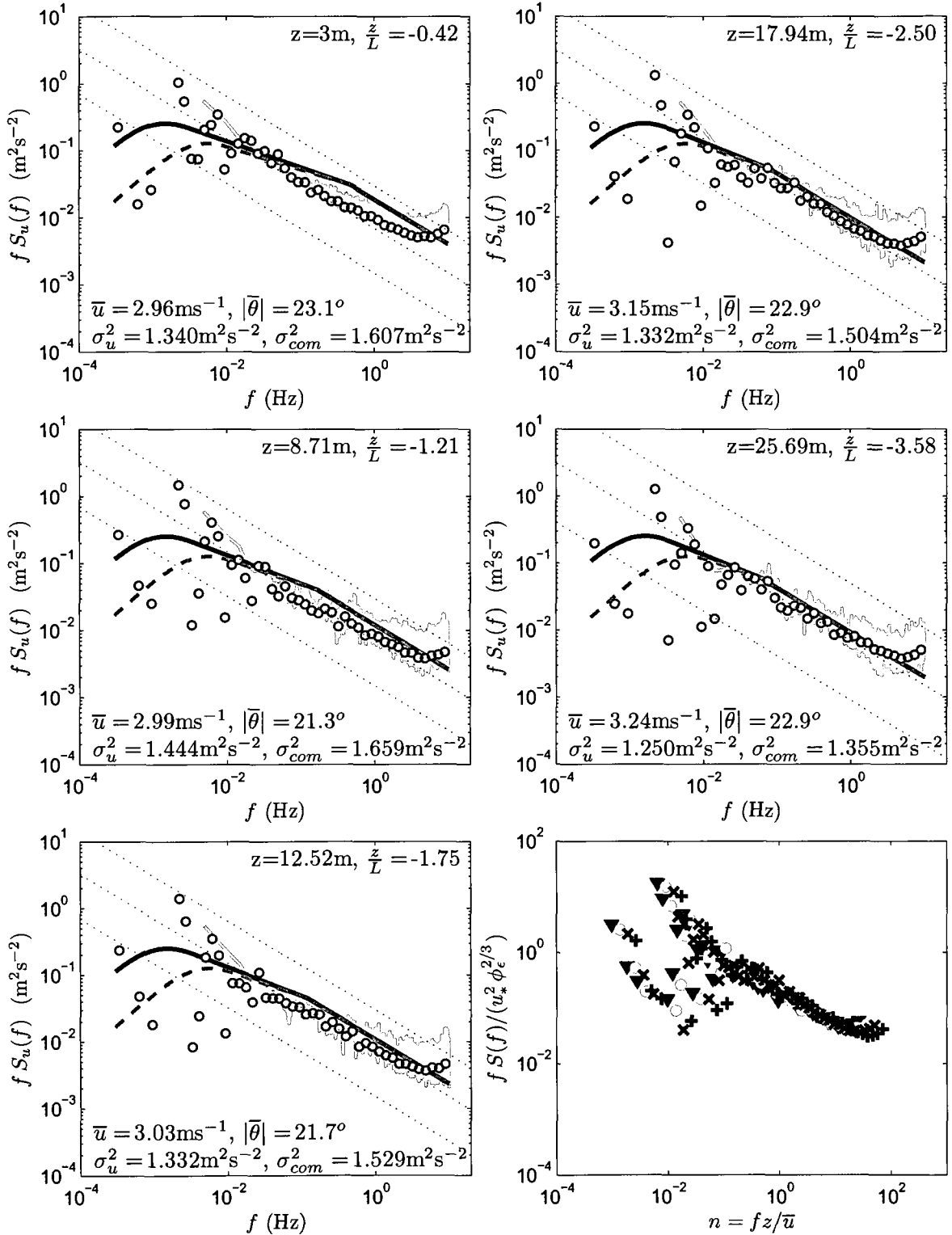
May.27,2005 12:47MDT, $L = -2.8 \text{ m}$, $u_* = 0.152 \text{ ms}^{-1}$, $\delta_K = 439.4 \text{ m}$, $\delta_{HF} = 353.4 \text{ m}$



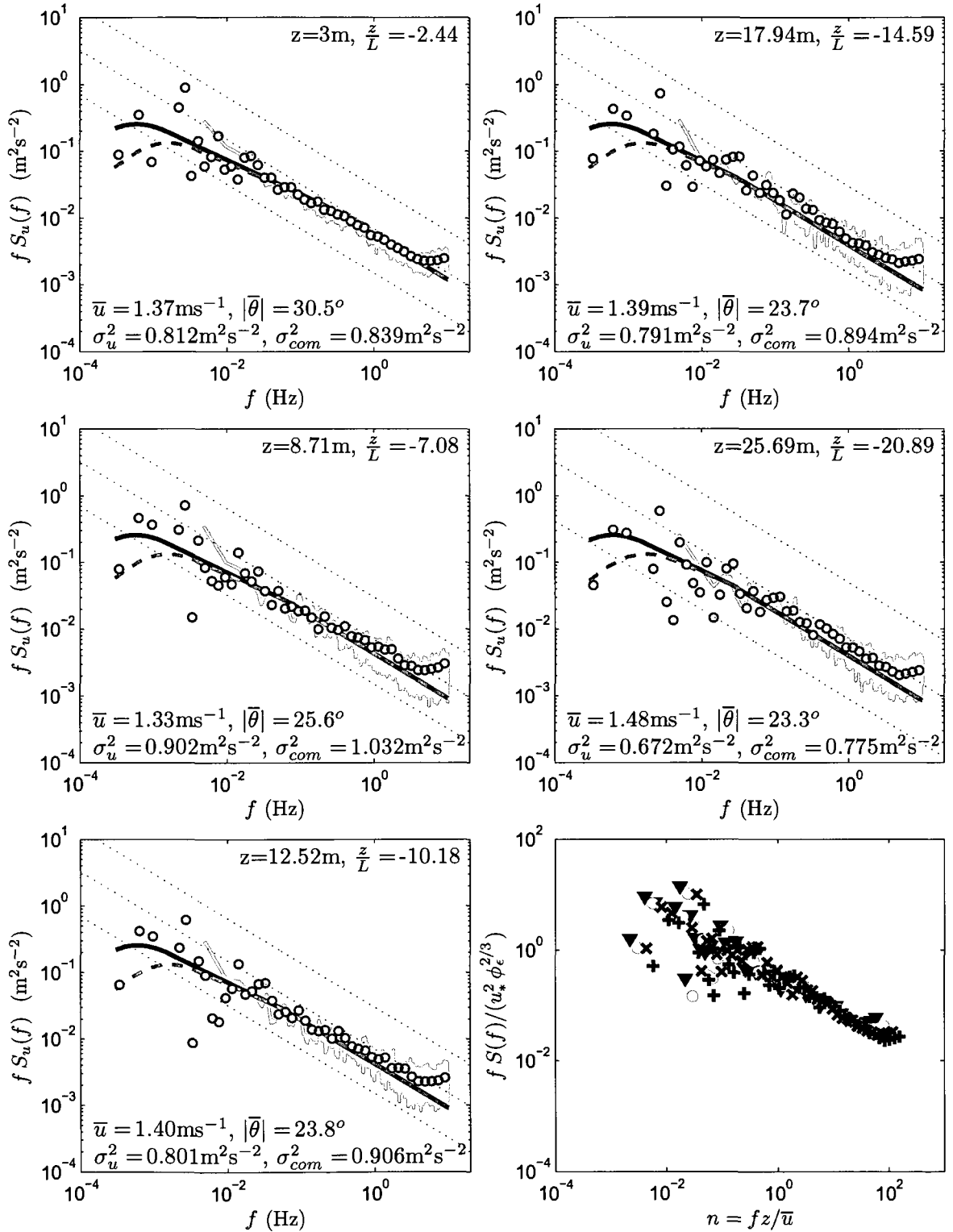
May.27,2005 13:47MDT, $L = -2.9$ m, $u_* = 0.171$ ms $^{-1}$, $\delta_K = 763.8$ m, $\delta_{HF} = 418.2$ m



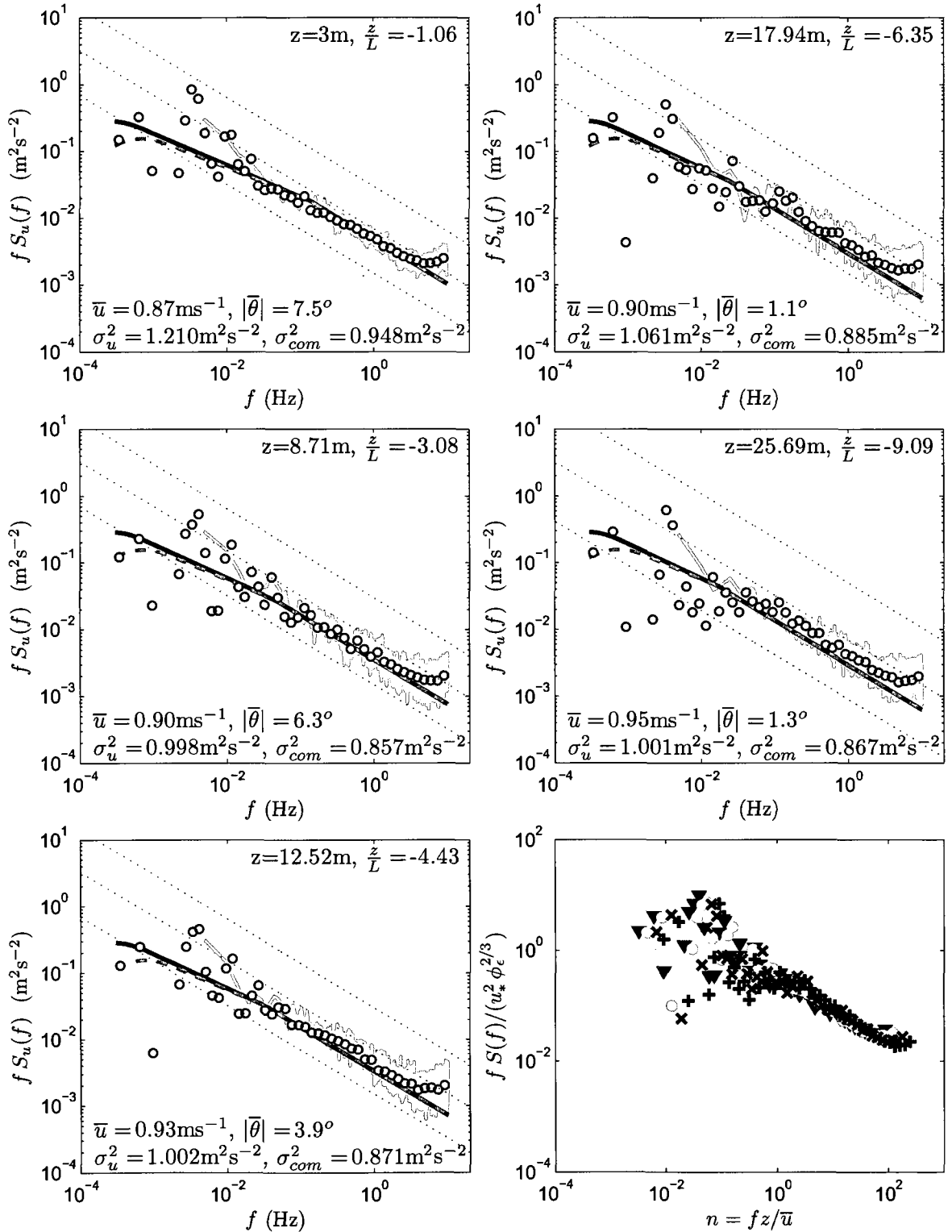
May.27,2005 14:47MDT, $L = -7.2 \text{ m}$, $u_* = 0.211 \text{ ms}^{-1}$, $\delta_K = 1301.9 \text{ m}$, $\delta_{HF} = 349.8 \text{ m}$



May.27,2005 16:47MDT, $L = -1.2 \text{ m}$, $u_* = 0.115 \text{ ms}^{-1}$, $\delta_K = 1545.0 \text{ m}$, $\delta_{HF} = 556.0 \text{ m}$



May.27,2005 17:47MDT, $L = -2.8 \text{ m}$, $u_* = 0.144 \text{ ms}^{-1}$, $\delta_K = 2151.3 \text{ m}$, $\delta_{HF} = 818.3 \text{ m}$



May.27,2005 18:47MDT, $L = -6.7$ m, $u_* = 0.166\text{ms}^{-1}$, $\delta_K = 2117.0\text{m}$, $\delta_{HF} = 1716.2\text{m}$

